

Integrated Experimental Methods and Machine Learning for Tire Wear Prediction

Chuang Su

Dissertation submitted to the faculty of the Virginia Polytechnic Institute and State University in partial fulfillment of the requirements for the degree of

Doctor of Philosophy
In
Mechanical Engineering

Taheri, Saied. Chair
Ahmadian, Mehdi
Sandu, Corina
Tarazaga, Pablo A.
Wang, Linbing

February 19, 2019
Blacksburg, VA

Keywords: tire wear, rubber abrasion, machine design, wear testing, machine learning

Copyright 2019, Chuang Su

Chuang Su

Abstract

A major challenge in tire research, is tire wear modeling. There are too many factors affecting tire wear, and part of those factors are difficult to be accurately expressed in physics and math.

The objectives of this research is to develop a machine learning based rubber sample wear model, and find the correlation between sample wear and tire wear. To develop this model, accurate and diverse wear data is necessary. The Dynamic Friction Tester (DFT) was designed and built for this purpose. This test machine has made it possible to collect accurate rubber sample wear data which has been validated under different conditions. Wear tests under diverse test conditions were conducted, and the test data were used to train machine learned based wear models with different algorithms, such as Neural Networks and Support Vector Machines. With test-proved wear behavior classification as additional input, and feature selection, performance of the trained rubber sample wear model has been further improved.

To correlate rubber sample wear and tire wear, a set of correlation functions were developed and proposed. By validating the correlation functions using tire wear data collected from the modified Rolling Resistance machine and road tests, this research contributes a fast and economical approach to predict tire wear.

Chuang Su

General Audience Abstract

Tire wear is closely related to the life time of tire, and excessive wear of tire can result in serious accidents. Since 1950s, research have been done to predict tire wear using experiments and empirical relations. These approaches are expensive, time consuming, and highly restricted to certain conditions.

The objectives of this research is to develop a statistic based rubber sample wear model, and find the correlation between rubber sample wear and tire wear. To develop the statistic based rubber sample wear model, a test machine, named Dynamic Friction Tester (DFT) was designed and built to collect rubber sample wear data. The final rubber sample wear model is trained by wear data under 600 different test conditions. A set of mathematical equations were proposed to correlate rubber sample wear and tire wear. These equations were validated by actual tire wear data collected from lab and public roads.

In combination of the statistic based rubber sample wear model and mathematical relation between rubber sample wear and tire wear, this research contributes a flexible, economical, and fast method to predict tire wear.

Acknowledgements

Foremost, I owe my deepest gratitude to my advisor, Dr. Saied Taheri for his encouragement, patience, support and guidance throughout my PhD study. I would like to thank my committee members: Dr. Mehdi Ahmadian, Dr. Corina Sandu, Dr. Pablo Tarazaga, and Dr. Linbing Wang, for their encouragement and comments.

I thank Michael Craft, Mehran Motamedi, Karan Khanse, Hongxiao Yu, and Eric Pierce for their assistance in building the DFT. I must acknowledge Anahita Emami and Sunish Vadakkeveetil for their cooperation in Multiscale Modeling of Tire Wear project. I thank Dr. Mehdi Ashraf-Khorasani for his assistance in toluene tests for rubber particles. As a team project, I thank Surabhi, Waleed, Arash, Chidambaram, Ashkan, and other students for their contribution and devotion in modifying the rolling resistance machine. I would like to thank Karthik, Mehran Shams Kondori, and Anish for their assistance in tire wear tests on the RR machine.

I thank Center for Tire Research (CenTiRe) Industry Advisory Board Members for their technical and financial support. Special thanks goes to Dr. Toshio Tada and Shinya Nakano from Sumitomo Rubber, who provided us with lots of useful suggestions and most importantly, rubber samples and tires.

I thank my parents for their irreplaceable support throughout my life.

Lastly, I would like to thank friends that I met during these years at Virginia Tech.

Table of Contents

| | |
|--|------|
| Abstract..... | ii |
| General Audience Abstract..... | iii |
| Acknowledgements..... | iv |
| List of Figures..... | viii |
| List of Tables..... | xii |
| 1. Introduction..... | 1 |
| 1.1 Motivation..... | 1 |
| 1.2 Main Contributions..... | 2 |
| 1.3 Document Outline..... | 3 |
| 2. Literature Review..... | 4 |
| 2.1 Physics behind Rubber/Tire Wear..... | 4 |
| 2.1.1 Crack Initiation and Propagation..... | 5 |
| 2.1.2 Major Factors Affecting Rubber Abrasion..... | 12 |
| 2.1.3 Major Factors Affecting Tire Wear..... | 16 |
| 2.1.4 Empirical Wear Models..... | 19 |
| 2.2 Materials of Rubber/Tire and oxidation..... | 22 |
| 2.2.1 Materials..... | 22 |
| 2.2.2 Rubber Oxidation..... | 24 |
| 2.3 Rubber/Tire Friction/Wear Test Machines and Methods..... | 30 |
| 2.3.1 Principles of Experimental Design..... | 30 |
| 2.3.2 Indoor Rubber Tests..... | 31 |
| 2.3.3 Indoor Tire Tests..... | 35 |
| 2.3.4 Outdoor Tire Tests..... | 38 |
| 2.3.5 Summary of Wear Test Machines and Methods..... | 42 |
| 3. Design/build Test Rigs..... | 44 |
| 3.1 Design and build the Dynamic Friction Tester (DFT)..... | 44 |
| 3.1.1 Structure of the DFT..... | 44 |
| 3.1.2 Choice of Sample Shape and Motion Type..... | 47 |
| 3.1.3 Sliding Velocity Control..... | 49 |

| | | |
|-------|---|----|
| 3.1.4 | Loading Mechanism..... | 50 |
| 3.1.5 | Wear Measurement | 51 |
| 3.1.6 | Sensors on the DFT..... | 53 |
| 3.1.7 | Procedures of Rubber Sample Wear Test | 54 |
| 3.2 | Design of the Trailer-Axle Tire Friction Tester | 55 |
| 3.2.1 | Structure..... | 56 |
| 3.2.2 | Key Components..... | 58 |
| 3.2.3 | Sensors on the Trailer-Axle Tire Friction Tester | 59 |
| 3.2.4 | Issues of the Design | 60 |
| 3.3 | Modification of the Rolling Resistance Machine for Wear Testing | 61 |
| 3.3.1 | Structure..... | 62 |
| 3.3.2 | Sensors | 65 |
| 3.3.3 | Comparison with Trailer-Axle Tire Friction Tester..... | 66 |
| 4. | Supervised Machine Learning | 68 |
| 4.1 | Additive Models and Trees | 68 |
| 4.1.1 | Generalized Additive Models | 69 |
| 4.1.2 | Tree-based Methods..... | 69 |
| 4.2 | Boosting Methods | 71 |
| 4.2.1 | AdaBoost..... | 71 |
| 4.2.2 | Boosting Trees | 72 |
| 4.3 | Tree Bagging and Random Forest..... | 74 |
| 4.4 | Neural Networks | 74 |
| 4.4.1 | Components of a Neural Network | 75 |
| 4.4.2 | Fit a Neural Network | 76 |
| 4.4.3 | Network Topology | 77 |
| 4.5 | Support Vector Machines..... | 78 |
| 4.5.1 | Basic of SVM..... | 79 |
| 4.5.2 | Constructing the Optimal Hyperplane | 80 |
| 4.5.3 | Kernel Trick | 81 |
| 4.5.4 | Least Squares Support Vector Machine..... | 83 |
| 4.5.5 | Applications of SVM in Wear Prediction..... | 84 |
| 4.6 | Comparison of Machine Learning Methods..... | 86 |

| | | |
|-------|---|-----|
| 4.6.1 | Coefficient of Determination | 86 |
| 4.6.2 | Prediction Error..... | 87 |
| 4.6.3 | Cross-validation | 88 |
| 4.6.4 | General Comparison of Supervised Machine Learning Models..... | 89 |
| 4.7 | Dimension Reduction..... | 90 |
| 4.8 | Choices of Inputs and Response for Rubber Sample Wear Model | 92 |
| 4.9 | Validation of the Wear Modeling Method | 94 |
| 4.10 | Choosing Machine Learning Algorithms for Wear Modeling | 98 |
| 5. | Results..... | 100 |
| 5.1 | DFT Performance Evaluation..... | 100 |
| 5.1.1 | Evaluation of Sensor Data | 101 |
| 5.1.2 | Evaluation of Sliding Velocity Control | 103 |
| 5.1.3 | Fluctuation of Normal Load..... | 103 |
| 5.1.4 | Repeatability of Wear Test | 104 |
| 5.2 | Initial Machine Learning Based Rubber Wear Modeling | 105 |
| 5.2.1 | Contact Patch Area of Rubber Samples..... | 106 |
| 5.2.2 | Effective Radius of Rubber Sample..... | 108 |
| 5.2.3 | Performance of Different Machine Learning Based Wear Models | 109 |
| 5.3 | Improvement of Rubber Wear Model | 111 |
| 5.3.1 | Introducing the Influence of Oxidation..... | 111 |
| 5.3.2 | Feature Selection..... | 117 |
| 5.4 | Complete Rubber Wear Model | 118 |
| 5.5 | Correlation of Rubber Wear and Tire Wear..... | 124 |
| 5.5.1 | Converting Parameters of Tire Wear into Rubber Wear | 124 |
| 5.5.2 | Tire Wear Tests..... | 130 |
| 5.5.3 | Validation of the Conversion Functions | 133 |
| 6. | Conclusions..... | 139 |
| 7. | Future Work | 142 |
| | References..... | 143 |

List of Figures

| | |
|---|----|
| Figure 1. Apparatus for testing friction and wear of rubber (Fukahori & Yamazaki, 1994) | 6 |
| Figure 2. Friction vs. sliding time and acceleration vs. sliding time (Fukahori & Yamazaki, 1994)..... | 7 |
| Figure 3. Initial cracks after 100 revolutions with 20 N normal load (Fukahori, Liang, & Busfield, 2008)..... | 7 |
| Figure 4. Abrasion pattern at the steady state at 20 N (Fukahori, Liang, & Busfield, 2008) | 8 |
| Figure 5. Model of a single ridge subject to friction (Fukahori & Yamazaki, 1995)..... | 9 |
| Figure 6. Model of hard slider on rubber surface (Fukahori & Yamazaki, 1995)..... | 10 |
| Figure 7. Cut growth rate vs. tearing energy (Lake & Lindley, 1965)..... | 13 |
| Figure 8. Sliding abrasion vs. temperature at 0.01m/s sliding velocity. (A) SBR, (B) ABR, (C) NR. --- tread compound, - gum compound (Gent & Walter, 2006)..... | 14 |
| Figure 9. Log abrasion rate vs. load at different slip angles at a speed of 19.2km/h (Gent & Walter, 2006)..... | 15 |
| Figure 10. (a) Abrasion rate vs. slip angle at 76 N load and 19.2km/h speed (b) logarithmic scales (Gent & Walter, 2006)..... | 15 |
| Figure 11. Log abrasion vs. log energy dissipation for two compounds and two surfaces (Gent & Walter, 2006)..... | 16 |
| Figure 12. Log tire wear rate vs. long slip angle (Grosch & Schallamach, 1961)..... | 17 |
| Figure 13. Abrasion of NR and SBR compounds vs. tire surface temperature (Grosch & Schallamach, 1961)..... | 17 |
| Figure 14. Wear rate of bias ply tire compared with radial ply tire (Gent & Walter, 2006) | 18 |
| Figure 15. In a controlled road wear test (a) Distribution of cornering acceleration (b) Distribution of fore and aft accelerations (Gent & Walter, 2006)..... | 19 |
| Figure 16. Distribution of speed in a controlled road wear test (Gent & Walter, 2006) .. | 19 |
| Figure 17. Testing scheme for evaluating coefficients of abrasion equation | 21 |

| | |
|--|----|
| Figure 18. chemical structure of vulcanized natural rubber (Jü, 2011) | 24 |
| Figure 19. Relative temperature dependence of permeability and oxidation rate of NR (Baldwin & Bauer, 2008)..... | 26 |
| Figure 20. Ahagon plot of retrieved on-road and spare tires | 27 |
| Figure 21. Ahagon plot of oven aged tires (Baldwin & Bauer, 2008)..... | 28 |
| Figure 22. Peel strength vs. shifted time. Shift factors (SF) are in the legend (Baldwin, Bauer, & Ellwood, 2005) | 29 |
| Figure 23. Dependence of rubber oxidation on oven temperature (Baldwin & Bauer, 2008) | 29 |
| Figure 24. (a) Sketch of the Dynamic Frictional Property Test Machine; (b) Principle of friction measurement (Frictional property tester of JLU, 2012)..... | 32 |
| Figure 25. (a) Contact geometries; (b) TE 75 rubber friction test machine (George, 2017) | 33 |
| Figure 26. High Speed Linear Friction Tester (Berres & Barz, 2017) | 34 |
| Figure 27. LAT100 Compound Tester (Description – Laboratory Abrasion & Skid Tester, 2014) | 35 |
| Figure 28. Rotating disk machine (Berritta, Cossalter, Doria, & Ruffo, 2002)..... | 36 |
| Figure 29. MTS Tire Rolling Resistance System (Tire Rolling Resistance Measurement System, 2014) | 36 |
| Figure 30. Flat-Trac® Tire Test System (Flat-Trac Tire Test Systems, 2014) | 37 |
| Figure 31. Tire Tread Wear Simulation System (Tire Tread Wear Simulation System, 2014) | 38 |
| Figure 32. RoaDyn® S630 sp System 2000 (Kistler, 2010)..... | 39 |
| Figure 33. ASFT Mk IV Rear -axle (Fernando, 2009) | 40 |
| Figure 34. Test course (Beebe, 2004) | 41 |
| Figure 35. The “Forward X” rotation plan (Beebe, 2004)..... | 41 |
| Figure 36. Front view (a) and left view (b) of the DFT | 46 |
| Figure 37. Rubber samples | 48 |
| Figure 38. Base of road surface | 49 |
| Figure 39. Kollmorgen AKM 4x servomotor | 49 |
| Figure 40. Loading mechanism..... | 51 |

| | |
|---|----|
| Figure 41. Rubber sample hub (transparent part is rubber sample) | 52 |
| Figure 42. HRB-303 high resolution balance (Lim, 2016)..... | 52 |
| Figure 43. Load cells measuring normal load and longitudinal friction force (highlighted in green squares) | 53 |
| Figure 44. Dynamic Friction Tester..... | 55 |
| Figure 45. Trailer in our lab..... | 56 |
| Figure 46. Trailer-Axle Tire Friction Tester..... | 57 |
| Figure 47. Normal load control..... | 59 |
| Figure 48. VBOX speed sensor | 60 |
| Figure 49. LW12.8 Wheel Load Transducer and its application (LW12.8, 2017) | 60 |
| Figure 50. Vibration isolation of the machine | 62 |
| Figure 51. Tire positioning mechanism (Ramdasi, 2016)..... | 63 |
| Figure 52. Modified rolling resistance machine (drive motor not included)..... | 65 |
| Figure 53. Partitions and CART (Hastie, Tibshirani, & Friedman, 2001)..... | 70 |
| Figure 54. Data processing in a neuron | 75 |
| Figure 55. Feed forward neuron network (Feedforward neural network, 2017) | 78 |
| Figure 56. Optimal separating hyperplane with maximum margin (Hofmann, 2006) | 79 |
| Figure 57. Mapping from 2-D space to 3-D space (Weston, 2006)..... | 82 |
| Figure 58. Definition of flank wear of broaching tool: (a) fresh tool, (b) worn tool (Shi & Gindy, 2007) | 84 |
| Figure 59. Comparison between predicted wear and wear measured by microscope (Shi & Gindy, 2007) | 85 |
| Figure 60. Experimental milling process (Slavkovic, Jugovic, Dragicevic, Jovicic, & Slavkovic, 2013) | 85 |
| Figure 61. SVR implementation (Slavkovic, Jugovic, Dragicevic, Jovicic, & Slavkovic, 2013) | 86 |
| Figure 62. RMS values of different kernel functions (Slavkovic, Jugovic, Dragicevic, Jovicic, & Slavkovic, 2013)..... | 86 |
| Figure 63. Dataset division | 87 |
| Figure 64. Training process of rubber sample wear model | 94 |
| Figure 65. Process of training friction model trained by early wear data..... | 95 |

| | |
|--|-----|
| Figure 66. Response plot of linear regression based friction modeling. Blue dots: true response, orange dots: predicted response | 96 |
| Figure 67. Structure of the 2-layer feedforward neural network | 97 |
| Figure 68. Error histogram of ANN based friction model trained by early data | 97 |
| Figure 69. Plot of calculated loads and measurements | 102 |
| Figure 70. Motor shaft position curve. (a): case 1; (b): case 2 | 103 |
| Figure 71. Normal load data during wear tests | 104 |
| Figure 72. Red patches on prescale film representing the sample contact patch..... | 106 |
| Figure 73. Contact patch area vs. load (rubber compound A) | 107 |
| Figure 74. Contact patch pressure vs. load (compound A)..... | 108 |
| Figure 75. R_c vs. F_N (compound A)..... | 109 |
| Figure 76. Wear rates of compound C on P120 sandpaper..... | 113 |
| Figure 77. Contact patch temperature of compound C on P120 sandpaper..... | 114 |
| Figure 78. Relationship of road smoothness, severity of dynamics, and abrasion behavior. (a) NR. (b) Synthetic rubber | 116 |
| Figure 79. Structure of final rubber wear model..... | 120 |
| Figure 80. wear rate vs. normal load – sliding velocity. Compound E on P120 sandpaper | 121 |
| Figure 81. Test and predictions of wear rate vs. normal load..... | 122 |
| Figure 82. Test and predictions of wear rate vs. sliding velocity | 123 |
| Figure 83. Test and predictions of wear rate vs. tensile strength..... | 124 |
| Figure 84. Standard tread measurement..... | 131 |

List of Tables

| | |
|---|-----|
| Table 1. Comparison of sample shapes and types of motion..... | 47 |
| Table 2. Comparisons of different loading mechanism | 50 |
| Table 3. Comparison of original and modified rolling resistance machine | 62 |
| Table 4. Comparison of supervised machine learning models | 89 |
| Table 5. Data categorization of wear tests on DFT | 92 |
| Table 6. Inputs of rubber sample wear model (early stage)..... | 93 |
| Table 7. Conditions of early wear test data..... | 95 |
| Table 8. Calculated load and sensor measurements..... | 101 |
| Table 9. Temperature measurements | 102 |
| Table 10. Standard deviation of repeated wear tests..... | 104 |
| Table 11. Contact patch test results (compound A)..... | 106 |
| Table 12. Rubber sample deformation test results (compound A) | 108 |
| Table 13. Test configurations for model comparison | 110 |
| Table 14. Performance comparison of machine learning algorithms | 111 |
| Table 15. Correlation of test conditions and oxidation..... | 114 |
| Table 16. Classification of rubber abrasion behaviors..... | 115 |
| Table 17. Toluene test conditions | 116 |
| Table 18. Comparison of reference and select-feature wear models | 118 |
| Table 19. Final wear test configurations..... | 119 |
| Table 20. Comparison of last-four wear models..... | 120 |
| Table 21. Rubber wear model and tire wear influential factors..... | 125 |
| Table 22. Parameters of wear tests on RR machine..... | 130 |
| Table 23. Tread depth measurements of RR machine tests (in mm)..... | 131 |
| Table 24. Parameters of tire wear tests on road | 132 |
| Table 25. Route map information | 132 |
| Table 26. Tread depth of tire A2..... | 133 |
| Table 27. Constants and coefficients of tire wear test on RR machine | 134 |
| Table 28. Constants and coefficients of tire wear test on road | 136 |

Table 29. Predicted weight loss in each road segment 137

1. Introduction

1.1 Motivation

An important problem in tire research, is tire wear prediction. Although this problem exists from the day when pneumatic tires were invented, there are not any widely-recognized models for tire wear. This is because there are too many physical and chemical factors affecting tire wear, and part of those factors are difficult to be accurately expressed in mathematical forms.

Nowadays, machine learning is becoming more and more widely used: self-driving, online recommendations, fraud detections, and so on. A lot of these applications have one thing in common: it is hard or impossible to develop an explicit model based on the theory. Machine learning gives computers the ability to learn without being explicitly programmed. After being trained with accurate, diverse and large enough data sets, a good machine learning model can accurately predict the system response, whose inputs are in the range of the data used for training the model. Machine learning models, especially neural networks and support vector machines (SVMs), have been applied in tool wear, and have proven to be successful. The main obstacle preventing researchers from using machine learning models in tire wear prediction, is that it is difficult to collect accurate tire wear data with enough diversity of test conditions.

Instead of collecting the data from tire tests, an alternative solution is to test small rubber samples, whose compound is the same as the tire tread, in the laboratory. The main advantage of testing rubber samples over actual tires, is the ease of developing test samples. However, a test machine that can provide enough diverse testing conditions for most wear-affecting factors and collect accurate data, did not exist and needed to be designed, fabricated and validated.

Even if a good rubber sample wear model could be developed and trained, there is still a need for developing a model for the tire. This is due to several factors such as tread patterns, pressure distribution in the contact patch, stiffness differences, etc. For this

purpose, some tire wear tests have to be performed under similar conditions as those of the rubber sample wear tests.

In this research, the following steps have been carried out:

1. Design and build a test machine, which can perform rubber sample wear tests under diverse conditions for most wear-affecting factors.
2. Use wear data collected from the test machine to develop and validate machine learning based rubber sample wear models.
3. Collect tire wear data from the modified Rolling Resistance machine and road tests.
4. Correlate rubber sample wear and tire wear.

1.2 Main Contributions

This research focuses on developing machine learning based rubber sample wear models capable of predicting tire wear. The main contributions are:

1. Designed and built the dynamic friction tester (DFT).

The DFT is a machine that can control or record most non-rubber-property factors that affect rubber wear, including: load, friction, sliding velocity, flash temperature, road surface roughness, and so on.

2. Developed machine learning based rubber sample wear model.

Although machine learning is becoming more and more popular, it has not been utilized to develop rubber/tire wear models. Based on collected wear data, comparisons of different machine learning methods were performed, and several new algorithms were developed. And finally, a machine learning based rubber sample wear model, which can provide accurate prediction under known conditions, was developed.

3. Developed a method to predict tire wear.

Tire wear tests are quite expensive and time consuming. Since the rubber compound of the rubber sample is the same as the tire tread compound, there could exist a relationship between rubber sample wear and tire wear. Finding that relationship means tire wear can be predicted

without running standard wear tests, therefore reduce the cost of wear tests.

1.3 Document Outline

The document is organized as follows.

- Chapter 1: motivation and main contributions.
- Chapter 2: literatures related to crack initiation and propagation, major factors affecting wear, empirical wear models, rubber materials, rubber oxidation and different rubber/tire test machines and methods are summarized.
- Chapter 3: The design and development of DFT is explained, as well as detailed test procedures. Also, the design of Trailer-Axle Tire Friction Tester is presented. Lastly, details of the modified Rolling Resistance machine are presented.
- Chapter 4: Multiple supervised machine learning models are introduced. After that, it is comparison of different supervised machine learning models. Lastly, is applying machine learning methods on rubber sample wear modeling.
- Chapter 5: The performance of DFT is validated from various aspects, which proves the tester as a reliable machine for wear data collecting. After that, are the procedures taken for improving the performance of rubber sample wear model. Rubber sample wear tests under 600 test conditions are conducted to train the final rubber sample wear model. Lastly, tire wear test data are collected to validate the proposed correlation functions between rubber sample wear and tire wear.
- Chapter 6: The results and achievements are summarized.
- Chapter 7: Detail plan of future work is discussed.

2. Literature Review

The nature of rubber abrasion, or tire wear, is the repeating process of crack initiation and propagation. The rate of rubber abrasion and tire wear are influenced by numerous factors, and part of these factors are difficult to be accurately expressed in mathematical form. Therefore, machine learning methods are introduced as a possible solution. Machine learning methods do not have to be explicitly programmed, but a large dataset is required. The performance of a machine learning based model, is heavily dependent on the quality of the dataset: the size of dataset, range of each input, correlation between inputs and response, etc. Thus, to collect a high quality dataset, the first step is to understand the physics behind abrasion/wear and understand which factors are necessary for a good wear model. With the correct choice of factors, the next step is to buy or develop a test machine that can control or measure all these factors during wear tests. Besides quality of dataset, performance of the trained model depends on the developed machine learning algorithm. There is no general “best” model, each model has its advantages and disadvantages, thus suits different situations.

Therefore, in the first section of this chapter, principles of crack initiation and propagation is explained, along with discussions of influential factors of rubber abrasion and tire wear, and current empirical wear models. In the following section, raw materials that go into rubber are described, and previous research on rubber oxidation are summarized. In the last section, several indoor/outdoor testing machines for friction/wear tests on rubber or tire are presented. In chapter 4, a comprehensive literature review of machine learning algorithms that have the potential of being used in wear modeling will be explained.

2.1 Physics behind Rubber/Tire Wear

To initiate this research, it is necessary to understand the physics behind rubber/tire wear phenomenon. In this section, previous research on crack initiation and propagation is summarized. Then the major factors affecting rubber abrasion and tire wear are listed. This is followed by review of the existing wear models.

2.1.1 Crack Initiation and Propagation

2.1.1.1 Overview

Numerous attempts have been made to discover the relationship between wear rate, physical conditions and rubber properties. Fukahori and Yamazaki discovered that the initial cracks were originated by micro-vibration and grew into abrasion patterns under a stick-slip motion (Fukahori & Yamazaki, 1994). After the needle scratch experiments of Schallamach (Schallamach, 1952), based on fracture mechanics, Champ et al. proposed a theory that directly relates abrasion of rubber by a knife edge to its crack-growth characteristics (Champ, Southern, & Thomas, 1974). This approach was widely used to predict fatigue crack growth (Busfield, Tsunoda, Davies, & Thomas, 2002) and to examine the physical process in rubber abrasion (Southern & Thomas, 1979) (Gent & Pulford, 1983). Fukahori and Yamazaki proposed a fracture mechanics approach to explain the periodic surface patterns, and thus rubber abrasion consists of two kinds of periodic motions: stick-slip oscillations and micro-vibration (Fukahori & Yamazaki, 1994). Their theory was supported by results from other researchers (Coveney & Menger, 1999) (Busfield, Liang, Fukahori, & Thomas, 2005).

2.1.1.2 Crack initiation

Fukahori and Yamazaki designed a tester to detect tangential frictional force and vibrations generated during sliding (Fukahori & Yamazaki, 1994). A rubber block (20 mm × 20 mm × 120 mm) is fixed on a damped steel plate which moves along a linear path. A steel blade is clamped at the end of a cantilever beam, and the blade is placed on the rubber block surface. After applying a normal load by a dead weight on the blade, the rubber block moves along the path while force is recorded.

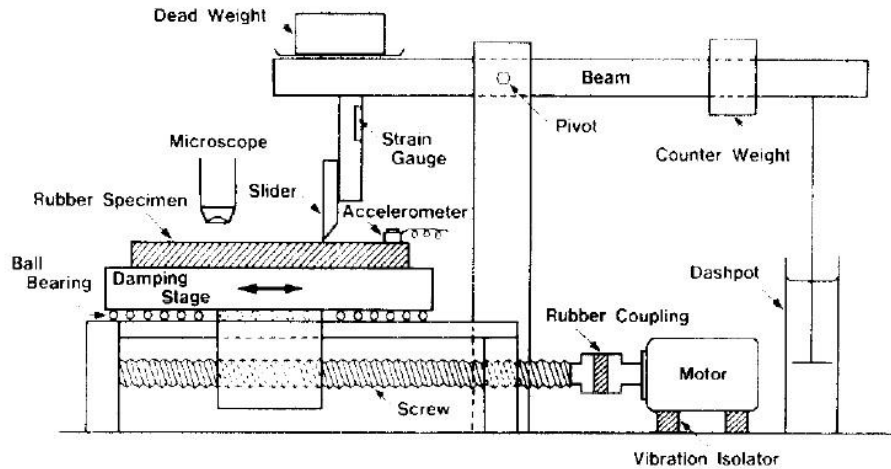


Figure 1. Apparatus for testing friction and wear of rubber (Fukahori & Yamazaki, 1994)

Due to jerk, friction force between a sliding hard surface and rubber is not constant. As the force increases, a hard slider will stick to rubber surface until a sudden break, then rapid slip occurs. This is called stick-slip motion, and is illustrated by the results from the tester. Figure 2 represents stick-slip motion, where region I and II correspond to stick and slip phases of the motion respectively. The acceleration vs. time plot in Figure 2 is the acceleration spectrum of the normal vibration of rubber surface, which includes high frequency micro-vibrations (500-1000Hz). At the end of each stick phase, rubber in front of the slider is compressed to the maximum limit and is suddenly released from the slider. At that moment, micro-vibration during each slip phase is generated.

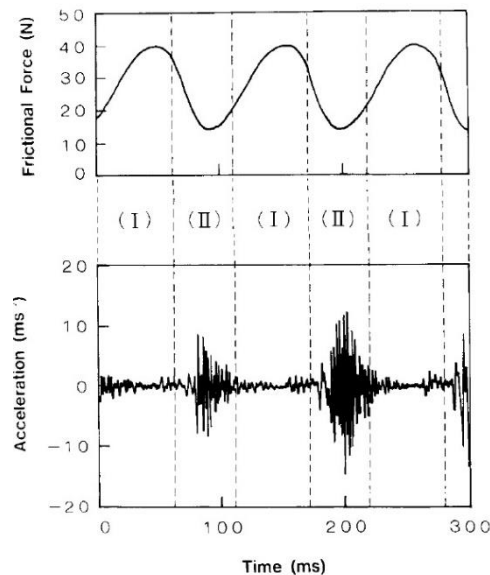


Figure 2. Friction vs. sliding time and acceleration vs. sliding time (*Fukahori & Yamazaki, 1994*)

After several sliding tests, numerous micro cracks were generated on the rubber surface. During micro-vibrations of the rubber surface, the surface moves up and adheres to the slider. The friction under the high relative sliding velocity generates high stress concentration at the edge of the contact area on the rubber, and a micro crack is formed. When test repeats, the slider will land on different locations of the rubber surface. As a result, slip zone of the new stick-slip motion can move into the previous stick zone. When the whole surface is covered by micro cracks, these micro cracks will grow in depth and pattern spacing. Finally, the pattern spacing will reach a critical value D_0 and stop increasing. Based on observations of abrasion test between rubber and a blade, Fukahori et al. figured out that the initial angle between crack and rubber surface is 30° to 50° , then is gradually reduced to about 20° (Fukahori, Liang, & Busfield, 2008).

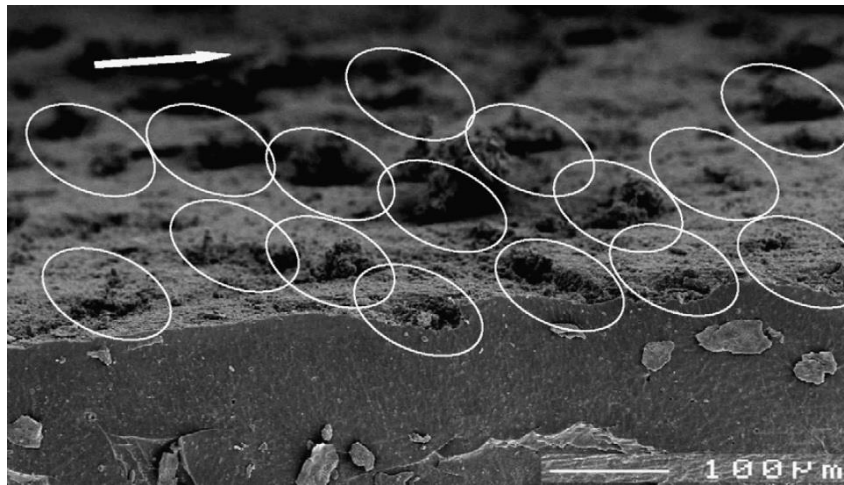


Figure 3. Initial cracks after 100 revolutions with 20 N normal load (*Fukahori, Liang, & Busfield, 2008*)

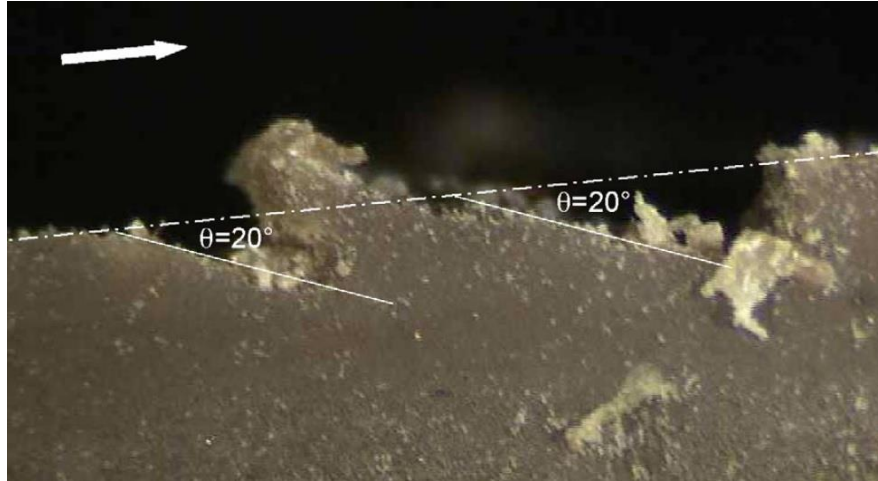


Figure 4. Abrasion pattern at the steady state at 20 N (Fukahori, Liang, & Busfield, 2008)

2.1.1.3 Crack propagation

When micro cracks are all over the rubber surface, during the stick phase, a hard slider not only compresses micro cracks, but also propagates the crack at the edge of contact area. When test repeats, small cracks will come together and form bigger cracks in depth and spacing. Meanwhile, during the process, micro-vibrations are continually generated, and keep forming micro cracks. Which means that micro cracks form on small ridges, small ridges on larger ridges. The crack propagation can be divided into two categories (Gent & Pulford, 1983):

- Propagation that takes place at the root of large ridges governed by adhesive force.
- Propagation of small cracks/ridges on large ridges' surface, which is governed by micro-vibration.

To model crack propagation rates, there are two approaches: fracture mechanics and energy dissipation. Brief derivation using these two approaches are presented in this section. Multiple crack growth rate models are listed in section 2.1.4.

From the view of fracture mechanics, abrasive wear can be related to crack growth resistance of rubber (Champ, Southern, & Thomas, 1974). Assume rubber is pulled by a tangential friction τ , which generates crack growth Δc in the direction of θ . Then crack growth per cycle dc/dn is:

$$\frac{dc}{dn} = AT^\alpha \quad (2.1)$$

A and α are empirical constants, T is tearing energy. Based on tests, $T = \tau(1 + \cos\theta) / h$ (Rivlin & Thomas, 1953), where h is the sample width. Assume that the rate of crack growth is equal to the rate of abrasion loss, then the rate of abrasion loss is:

$$\bar{V} = h \sin\theta \frac{dc}{dn} \quad (2.2)$$

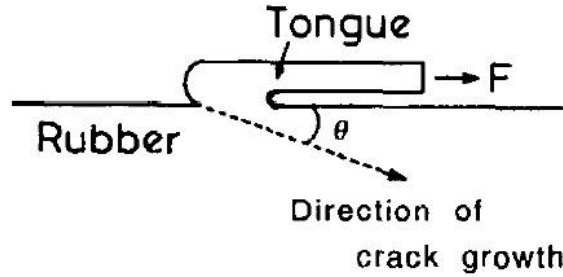


Figure 5. Model of a single ridge subject to friction (Fukahori & Yamazaki, 1995)

Now consider linear wear rate in the direction of θ :

$$D = \frac{\bar{V}}{h} \sin\theta \quad (2.3)$$

\bar{V} and θ can be measured. Thus D can be calculated.

Under pure shear condition, the rate of crack growth per cycle dc / dn can be measured as a function of strain. Which means that, if the strain amplitude at root of ridges can be estimated, wear rate can be obtained. Assume perfect sticking between hard slider and rubber, and the stress is restricted within an area of abrasion pattern, then the mean strain amplitude is:

$$\bar{\varepsilon}_{id} = \frac{L_{st}}{L_{sl}} \quad (2.4)$$

L_{st} is the distance that slider moves in the stick phase and L_{sl} is the distance that slider moves in the slip phase. In reality, perfect sticking does not exist, and the mean strain amplitude becomes:

$$\bar{\varepsilon}_{ac} = \frac{L_{st} - \Delta r}{L_{sl}} \quad (2.5)$$

Δr is the distance that slider slides in the stick phase.

The relationship between D and crack growth rate at mean strain $\bar{\epsilon}$ is:

$$D = \frac{dc(\bar{\epsilon})}{dn} \quad (2.6)$$

This relationship had been proven by tests. As a result, the linear wear rate can be estimated from crack growth rate under cyclic deformation. In reality, the actual mean strain is $\bar{\epsilon}_{ac} = \frac{\mu P}{ES} - \frac{\Delta r}{S_{sl}}$. E is Young's modulus of rubber, S is the cross sectional area in

Figure 6, μ is friction coefficient, and P is normal load. Now it is clear that the mean strain is governed by friction coefficient, Young's modulus E , normal load and area S .

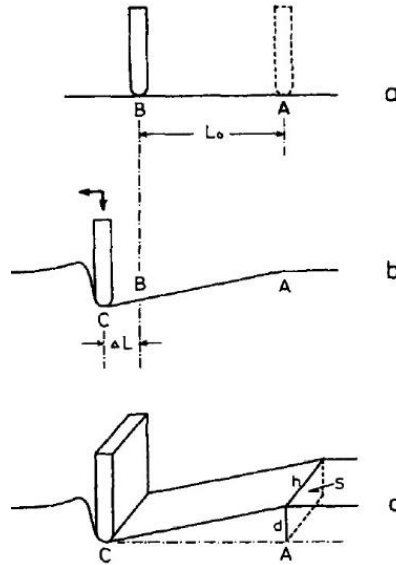


Figure 6. Model of hard slider on rubber surface (Fukahori & Yamazaki, 1995)

Researchers also studied crack propagation from the view of energy dissipation. For example, the high-velocity behavior of energy met Barenblatt model (Barenblatt, 1962) based crack propagation study by Barber, et. al (Barber, Donley, & Langer, 1989), and Persson and Benner's study on Crack propagation from the aspect of energy dissipation (Persson & Brener, 2005).

In Persson and Benner's study, the strength of adhesion and cohesion of elastomers can be characterized by the amount of energy G required to advance one unit area. Based on experiments, G can be expressed as (Gent A. N., 1996):

$$G(v,T) = G_0 [1 + f(v,T)], \quad (2.7)$$

where v is the crack-tip velocity, T is temperature, $f \rightarrow 0$ as $v \rightarrow 0$, G_0 is a threshold value below which fracture won't occur. The measured value of G at extremely low v and high T can be treated as G_0 . In a viscoelastic solid, the energy dissipation at a crack has two contributions. The first contribution is the effect on the inner most region at crack tip, which is described as $G_0 = 2\gamma_0$. The second contribution is in front of the tip.

Consider a crack loaded in tension (mode I) in a visco-elastic solid. Firstly, calculate energy dissipation per unit time and unit length of crack, P :

$$P = \int d^2x \dot{\epsilon}_{ij} \sigma_{ij} \quad (2.8)$$

$\dot{\epsilon}_{ij}$ is strain rate tensor and σ_{ij} is stress tensor. For a homogeneous material, the stress has the form of (Anderson, 2017):

$$\sigma(\mathbf{x}, t) \approx K(2\pi |\mathbf{x} - \mathbf{vt}|)^{-1/2} \quad (2.9)$$

Therefore,

$$P = \frac{2\alpha K^2 v}{\pi} \int_0^1 dx \frac{(1-x^2)^{1/2}}{x} \text{Im} \frac{1}{E(x\omega_c)} \quad (2.10)$$

where $\omega_c = 2\pi v / a$. Consider the energy conservation condition related to crack propagation. The elastic energy stored in the solid in front of the crack tip is dissipated at the crack tip (Persson & Brener, 2005). Elastic energy that flows into the crack is Gv , which should equal to fracture energy plus the bulk visco-elastic dissipation P , yields:

$$G = G_0 + \frac{2\alpha K^2 v}{\pi} \int_0^1 dx \frac{(1-x^2)^{1/2}}{x} \text{Im} \frac{1}{E(x\omega_c)} \quad (2.11)$$

α can be determined by considering γ_{eff} for very large crack velocities.

Based on experiments, crack tip radius a in polymers increases with increasing speed of crack tip, which is:

$$\frac{a}{a_0} = \frac{1}{1 - \kappa \int_0^\infty d\tau H(\tau) \left\{ \left[1 + b^{-2}(\tau) \right]^{1/2} - b^{-1}(\tau) \right\}} \quad (2.12)$$

where $b = \omega_c \tau$, $\kappa \approx 0.999$, $H(\tau) = \frac{H(\tau)}{d\tau' H(\tau')}$. With the value of a , fracture energy can be

calculated from (2.11).

2.1.2 Major Factors Affecting Rubber Abrasion

2.1.2.1 Pressure dependence of sliding abrasion

Based on abrasion experiments, abrasion is generally a non-linear function of pressure:

$$abr = abr_{ref} \left(\frac{p}{p_0} \right)^n \quad (2.13)$$

The reference abrasion loss abr_{ref} at reference pressure p_0 and n , are depend on rubber compound and track. If the track is smooth, the abrasive loss can be small at very high friction. On the other hand, if the track is rough, the abrasive loss might be high at moderate friction.

2.1.2.2 Energy consumption in the contact patch

For sliding, energy dissipation is:

$$W = F_f s \quad (2.14)$$

F_f is the friction, s is distance travelled. On extremely sharp tracks, abrasion loss is almost proportional to friction force (Gent & Walter, 2006).

2.1.2.3 Relationship between cut growth rate and tearing energy

The relationship between cut growth rate and tearing energy can be divided into four regions (Lake & Lindley, 1965).

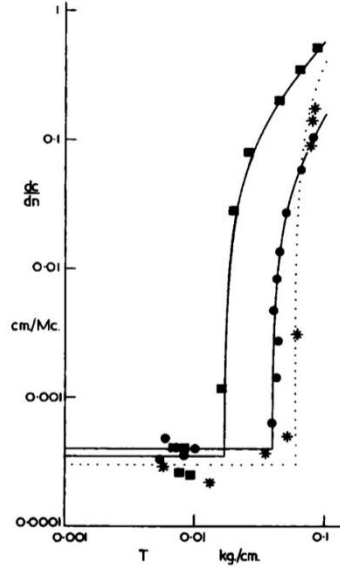


Figure 7. Cut growth rate vs. tearing energy (Lake & Lindley, 1965)

- Below a tearing energy T_0 , there is no tearing.
- Above T_0 , there is a region where cut growth rate is proportional to tearing energy.

$$\frac{dc}{dn} = A_{cr}(T - T_0) \quad (2.15)$$

A_{cr} is a material property influenced by temperature and oxygen.

- In the third region, the relationship becomes:

$$\frac{dc}{dn} = B_{cr}T^\beta \quad (2.16)$$

B_{cr} is also a material property influence by temperature and oxygen.

- In the last region, when tearing energy approaches T_c , rupture occurs, and cut growth rate becomes very large.

In most cases, abrasion occurs mainly in the third region. If the track is very sharp, then the cut growth rate becomes much higher, and the abrasion rate is proportional to the energy density at break (Gent & Walter, 2006).

2.1.2.4 Temperature dependence of sliding abrasion

For simple unfilled, non-crystallizing rubber compounds, the temperature dependence of sliding abrasion on sharp tracks is dominated by the visco-elastic property of rubber (Gent & Walter, 2006). Abrasion rate decreases with decreasing temperature and reach a minimum value. As temperature keeps decreasing, abrasion rate begins to increase. This phenomenon is accompanied by obvious change in the abraded surface.

For tire tread compounds, temperature dependence is smaller, but the trend is similar. Compared with corresponding unfilled compounds, abrasion rate of tire tread compounds is much higher.

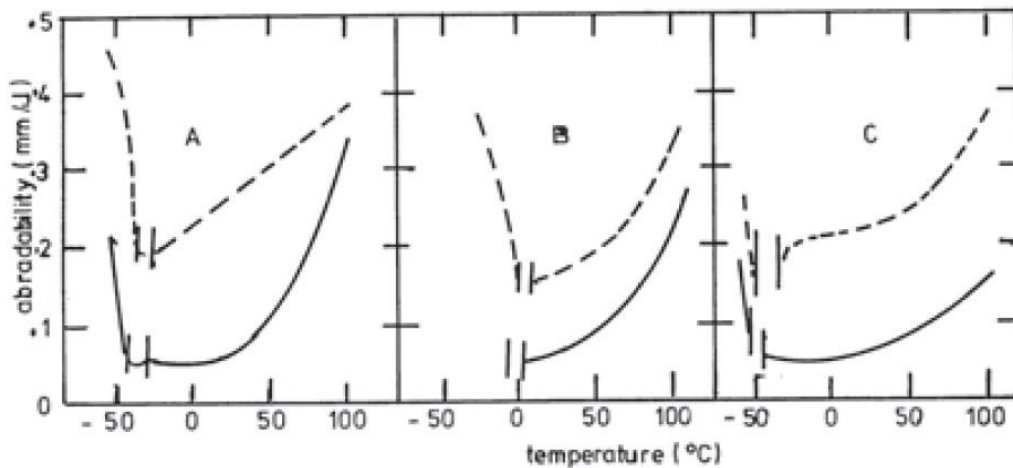


Figure 8. Sliding abrasion vs. temperature at 0.01m/s sliding velocity. (A) SBR, (B) ABR, (C) NR. --- tread compound, - gum compound (Gent & Walter, 2006)

2.1.2.5 Abrasion as a function of slip and load

Abrasion tests were carried out on multiple tread compounds with given slip angle (-40° to 40°) and a range of loads (10 to 150 N). Figure 9 shows the abrasion rate vs. load at different slip angles. From the figure, we can see that at small slip angles, abrasion rate is less dependent on load. When slip angle increased, the load dependence also increased.

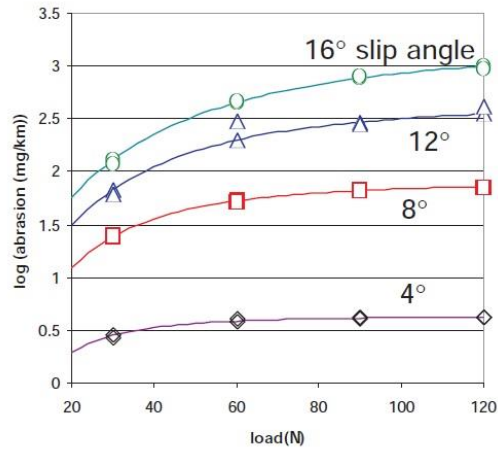


Figure 9. Log abrasion rate vs. load at different slip angles at a speed of 19.2km/h (*Gent & Walter, 2006*)

Figure 10 (a) Shows abrasion rate vs. slip angle for two compounds: OE-SBR and 80NR/20BR. It is obvious that abrasion depends on slip angle: abrasion rate increases with increasing slip angle. If both abrasion rate and slip angle are plotted on log scales, the curves become straight lines as in Figure 10 (b).

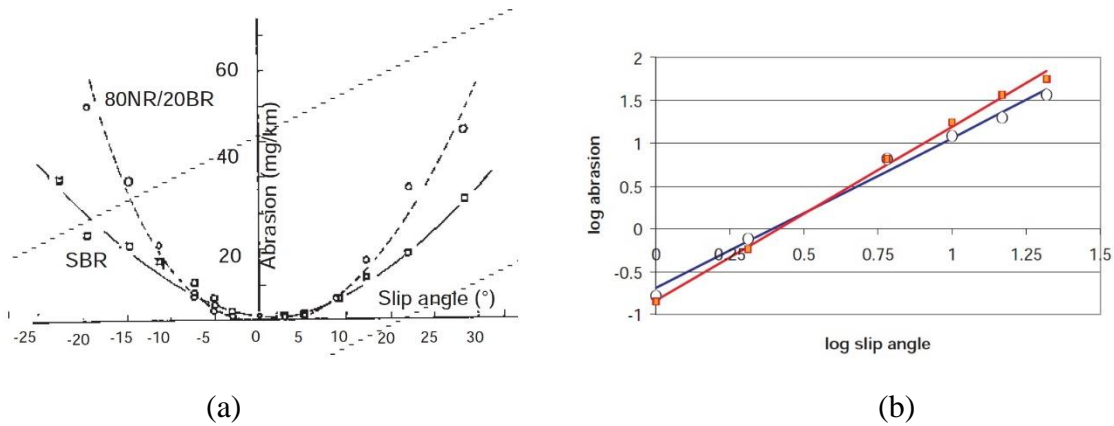


Figure 10. (a) Abrasion rate vs. slip angle at 76 N load and 19.2km/h speed (b) logarithmic scales (*Gent & Walter, 2006*)

If side force and slip angle are recorded, abrasion rate can be plotted as a function of energy dissipation. As in Figure 11, Straight lines are obtained again on logarithmic scales. At low energy levels, the lines of different compound will cross.

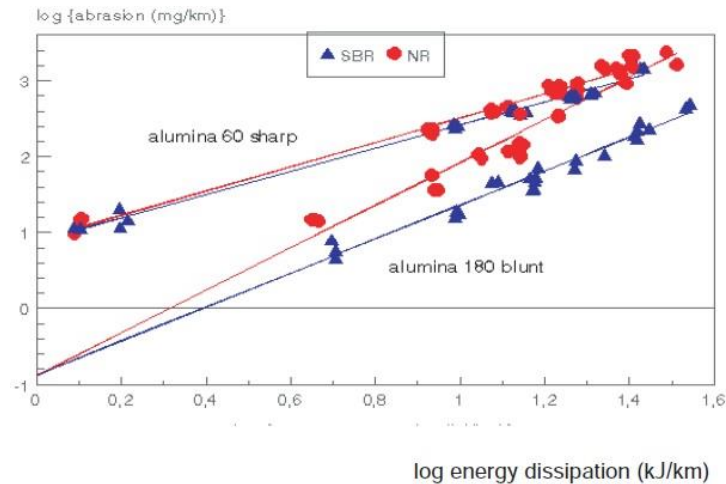


Figure 11. Log abrasion vs. log energy dissipation for two compounds and two surfaces (Gent & Walter, 2006)

2.1.2.6 Speed dependence of abrasion rate

Experiments were carried out on different tread compounds at different speeds. On log plots, the abrasion rate vs. speed is straight line again. For different speed and different tread compound, the lines' slopes are different.

When vehicle speed increases, energy dissipation increases, and the tire surface temperature will rise. Rising surface temperature will affect rubber strength, thus affect abrasion rate. When it comes to tread compound difference, compounds have better resistance of strength loss and thermos-oxidative degradation in high temperature are affected less by speed.

2.1.3 Major Factors Affecting Tire Wear

2.1.3.1 Slip angle and temperature effects

Schallamach carried out tire wear tests under controlled load and slip angle with three different tire tread compounds (Grosch & Schallamach, 1961). Wear rate vs. slip angle was plotted on log scales, which results in straight lines. NR and SBR compounds cross at low slip angle, SBR and 50NR/50BR compounds cross at high slip angle.

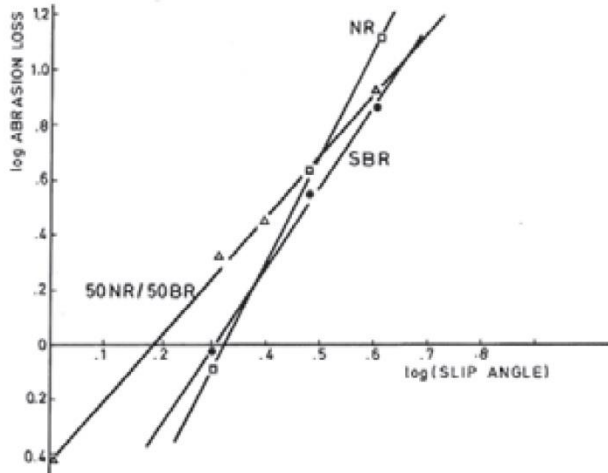


Figure 12. Log tire wear rate vs. long slip angle (*Grosch & Schallamach, 1961*)

Tire wear rate vs. tire surface temperature is plotted in Figure 13. The lines of SBR (A) and NR (B) cross at about 48°, after which NR compound has a much high wear rate. Since NR/BR has a much higher cross point, it has better thermal stability.

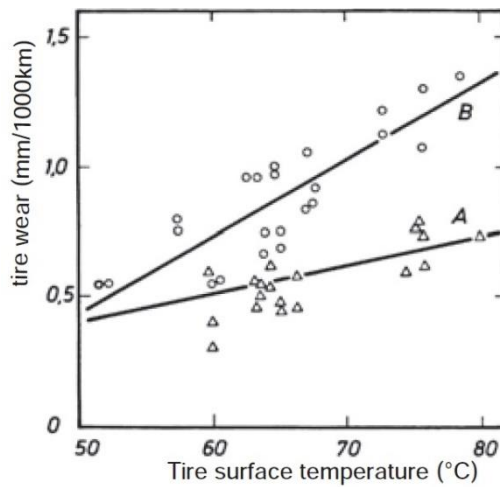


Figure 13. Abrasion of NR and SBR compounds vs. tire surface temperature (*Grosch & Schallamach, 1961*)

It must be mentioned that, although temperature affects properties of rubber, the main reason of higher abrasion is accelerated thermal oxidative process caused by higher temperature.

2.1.3.2 Road surface effects

Consider a test car running on a 600 km test course. Along the test course, there will be road surface change, which needs to be measured and averaged. Also, road surface varies in different seasons. For example, road surfaces in moderate climate areas are much sharper in winter (Gent & Walter, 2006). And of course, road surface profile changes according to weather.

Due to these effects, the repeatability of road tests is low, and one road test result only have limited validity.

2.1.3.3 Tire construction effects

During a tire wear test, depending on if the tire is force controlled (road wear), or slip controlled (laboratory tester), will have a large influence on the test results. In Figure 14, the effect is obvious. When tires were mounted on trailer axle for equal slip angles, the tires will have same side force. The consequence is that the slip angle of stiffer (radial ply) tire was reduced, and the slip angle of softer tire (bias ply) was increased. As a result, if test tires were mounted with controlled slip angles, stiffer tires will have a higher wear rate than force controlled situation, while softer tires will have a lower wear rate.

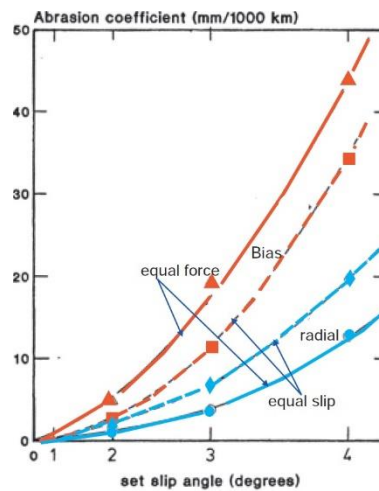


Figure 14. Wear rate of bias ply tire compared with radial ply tire (Gent & Walter, 2006)

2.1.3.4 Driving effects

Tire wear rate will change due to cornering, accelerating, braking, wind pressure, and rolling resistance. To estimate their effects, test course was divided into small sections where speed and force can be treated as constant. Figure 15 (a) shows the

distribution of lateral acceleration during cornering in a controlled road test, it is very similar to a normal distribution. Figure 15 (b) shows the distribution of acceleration during accelerating and braking, it is also similar to a normal distribution. The rolling resistance is mainly related to load. Wind pressure is a function of vehicle speed and dimension. Figure 16 shows vehicle speed distribution during a controlled road wear test. The distribution is approximately the sum of two normal distribution.

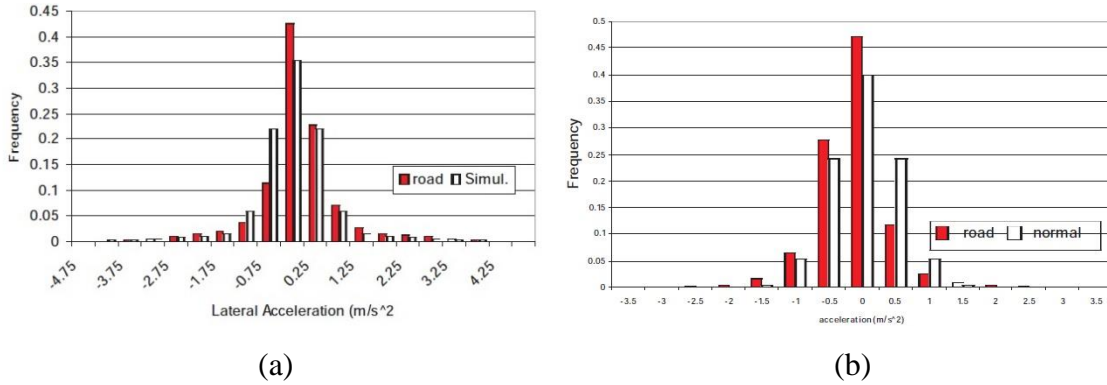


Figure 15. In a controlled road wear test (a) Distribution of cornering acceleration (b) Distribution of fore and aft accelerations (*Gent & Walter, 2006*)

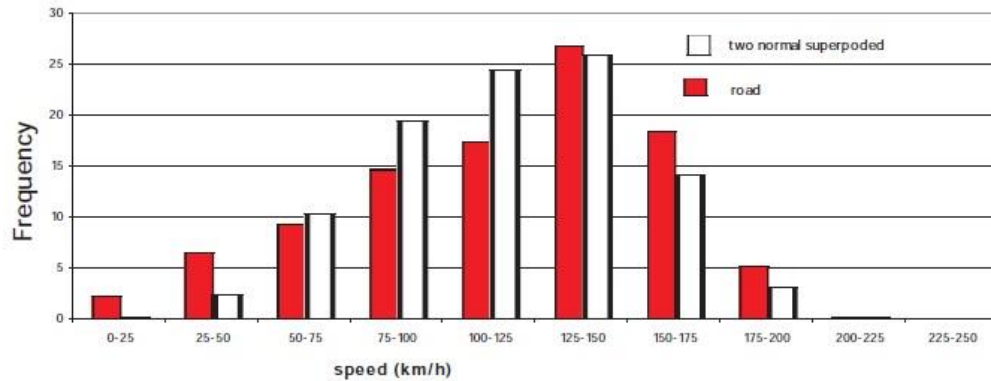


Figure 16. Distribution of speed in a controlled road wear test (*Gent & Walter, 2006*)

2.1.4 Empirical Wear Models

By applying a steel blade on rubber, Thomas (Thomas, 1974) proposed that:

$$r = B \left(\frac{F}{h} \right)^\alpha \quad (2.17)$$

where r is crack growth per cycle, B is a coefficient, F is frictional force, h is width, and α varies from about 2 for natural rubber to 4 or more for noncrystallizing unfilled rubbers such as SBR (Gent, Lindley, & Thomas, 1964).

By sliding polymers against metal surfaces (cast iron and chromium), Rhee (Rhee, 1970) proposed an empirical wear equation:

$$\Delta W = KF^a V^b t^c \quad (2.18)$$

where ΔW is weight loss, K is a wear factor, F is load, V is velocity, t is the time of sliding, and a, b, c are constants for a given system.

By applying a steel blade on rubber block, Gent, et. al (Gent & Pulford, 1983) summarized that wear rate of elastomeric material is proportional to a power n of the applied friction:

$$A = k \cdot F^n \quad (2.19)$$

where A is wear rate, k is a coefficient, F is frictional force. The value of n depends on the material, ranging from about 1.5 for carbon black filled SBR to over 3 for unfilled PB material.

Liang, et. al. (Liang, Fukahori, Thomas, & Busfield, 2010) summarized that the relationship between crack growth rate per cycle is:

$$\frac{dc}{dn} = X \left(\frac{T}{T^*} \right)^\psi \quad (2.20)$$

Where c is the crack length, n is the number of cycles and X and ψ are rubber crack growth parameters determined by an independent pure shear fatigue crack growth test, and the stored energy release rate $T \cdot T^*$ has a value of 1 Jm^{-2} . The simulation results were compared with blade abrasion tests of four rubber materials: NR, SBR, BR and carbon black filled SBR. Simulation gives a reasonable abrasion rate prediction for SBR and BR materials, while the simulated NR material abrasion rate is 30 times worse than the test results.

Grosch and Schallamach (Grosch & Schallamach, 1970) proposed the load dependence of rubber abrasion and tire wear. Wear of an Akron sample (flat sample of about 6 cm^2 contact area) is:

$$W_A = [\text{const.} / (n + 1)] \zeta b (\rho / \mu)^n \theta^{n+1} L^{0.48+0.11n} \quad (2.21)$$

where the constant, n, ζ depends on the elastic properties of the compound, b is the width of contact area, ρ is resilience of the whole wheel, μ is friction coefficient, θ is slip angle, and L is normal load. Wear of tires is greatly influenced by the side forces. Therefore, tire wear can be expressed in terms of the side force:

$$W = [2^{n+1} / (n+1)] \zeta (1/ab)^n (1/Ma) (\rho / \mu)^n S^{n+1} \quad (2.22)$$

where a is length of the contact area, M is wheel stiffness, and $S = \Delta v / v$, v is travelling velocity, Δv is slip velocity.

Since plots of abrasion rate against both sliding energy and sliding speed are straight lines in logarithmic scales (Gent & Walter, 2006), Grosch also proposed that rubber abrasion rate can be modeled as:

$$\log(A) = a + b_1 \log(W) + b_2 \log(v) + b_3 \log(W) \cdot \log(v) \quad (2.23)$$

Where A is abrasion volume loss per km, W is energy dissipation per km and v is the forward speed of abrasive disk. To estimate the coefficients a, b_1, b_2, b_3 , at least four different test conditions are required. For better results, more conditions are better, as in Figure 17. The four coefficients are calculated from test results using least square deviations from the mean.

| | | speed (km/h) | | | | | | | | | |
|----------------|------------|--------------|------|------|------|------|-------|-------|-------|-------|--|
| energy (kJ/km) | log energy | 1.00 | 1.58 | 2.51 | 3.98 | 6.31 | 10.00 | 15.85 | 25.12 | 39.81 | |
| 1.00 | 0 | | | | | | | | | | |
| 1.58 | 0.2 | | | | | | | | | | |
| 2.51 | 0.4 | | | | | | | | | | |
| 3.98 | 0.6 | | | | | | | | | | |
| 6.31 | 0.8 | | | | | | | | | | |
| 10.00 | 1 | | | | | | | | | | |
| 15.85 | 1.2 | | | | | | | | | | |
| 25.12 | 1.4 | | | | | | | | | | |
| 39.81 | 1.6 | | | | | | | | | | |

Figure 17. Testing scheme for evaluating coefficients of abrasion equation

Lowne (Lowne, 1970) proposed the relationship between road surface texture and tire wear, which is:

$$W \propto \overline{D \cot \alpha} \quad (2.24)$$

where D is the density of asperities, and $\overline{\cot \alpha}$ is the average value of $\cot \alpha$ for all asperities. Coefficients of this relationship is calculated by regression analysis using test data. Wear tests were conducted in two methods: accelerated wear tests were performed

by running a free-rolling wheel with its plane at 20° to the direction of travel; the other method is less severe, which used the offside front wheel of a front wheel drive passenger car.

Although several empirical crack growth models have been proposed, it is difficult to correlate crack growth rate with rubber or tire wear rate. In Grosch's models, although road profile is a major factor that influence wear rate, it was not included in the models. In Lowne's wear model, besides road surface texture, all other parameters, like load, slip angle, rubber property, etc., are neglected. In conclusion, current empirical wear models are highly restricted, thus proposing an empirical rubber/tire wear that considers all major influential factors is great contribution to this field of research.

2.2 Materials of Rubber/Tire and oxidation

Besides the factors mentioned in section 2.1, oxidation is another important factor that influence rubber/tire wear. However, since oxidation is a polymer chemistry problem that mainly relies on experiments, no models that can describe the relationship among compound, oxidation and rubber properties have been proposed yet. To understand rubber oxidation and its potential influence on wear, basic knowledge of the raw materials that go into tire rubber is necessary. After that, previous research on rubber oxidation are summarized.

2.2.1 Materials

Rubber compounds are made up of over 200 raw materials, including elastomers, reinforcing fillers, plasticizers, and other chemical elements (Michelin, n.d.).

2.2.1.1 Elastomers

The major material of rubber compounds, is elastomers/rubber, which is a polymer with viscoelasticity, weak intermolecular forces, usually low Young's modulus and high failure strain (De & White, 2001). There are two types of elastomers used in rubber compounds: natural rubber and synthetic rubber. 60% of rubber used in tire industry is synthetic rubber, while the remaining 40% is natural rubber (Michelin, n.d.).

Natural rubber is obtained from latex of rubber trees, which are mainly grown in Southeast Asia, Latin America and Africa. Natural rubber is synthesized from 2-methyl-1,3-butadiene, where most of the double bonds in the polymer chain have the Z configuration, therefore rubber gets its elasticity. Generally, natural rubber can reduce internal heat generation while providing high mechanical resistance. As a result, natural rubber is preferred in heavy-duty conditions, such as tire tread of truck and earthmover.

Unlike natural rubber whose source is trees, synthetic rubber is produced from petroleum-derived hydrocarbons: isoprene, 1,3-butadiene, chloroprene, and isobutylene. These and other monomers are mixed in different proportions to produce rubber with a wide range of physical, mechanical and chemical properties. Some well-known synthetic rubbers are:

- Styrene-butadiene rubber (SBR): copolymer of 1,3-butadiene and styrene.
- Nitrile rubber (NBR): copolymer of butadiene and acrylonitrile.
- Butyl rubber (BR): copolymer of isobutylene and isoprene.

Synthetic rubber returns to its original shape when stress is released, which means higher grip. Also, compared with natural rubber, synthetic rubber generally has longer life and better rolling resistance. Therefore, it is mainly used for tires of passenger cars and motorcycles.

2.2.1.2 Reinforcing Fillers

To enhance physical properties of rubber, reinforcing fillers are added, such as carbon black and silica.

Carbon black is generated from incomplete combustion of heavy petroleum products, and has the form of paracrystalline carbon. While pure rubber has less than 2 MPa tensile strength, adding carbon black can increase the tensile strength to more than 20 MPa. Besides tensile strength, carbon black also improves rubber's wear resistance (Donnet, 1993), and give tires the distinctive color, which is very effective against ultraviolet and prevent tires from cracking.

Silica was originally used for improving rubber's tear resistance. In 1992, Michelin developed a mixing process of silica and elastomer, and the resulting compound has both low rolling resistance (requires low hysteresis at low frequency) and good grip

(requires high hysteresis at high frequency). This innovation is at the beginning of eco-friendly tires, which demand good grip and low rolling resistance (reduce fuel consumption) at the same time.

2.2.1.3 Plasticizers and Other Chemical Elements

Plasticizers changes viscoelasticity of rubber. In tire industry, two common types of plasticizers are oils and resins.

Various other chemicals are also added into rubber compound to change its mechanical-physical properties. For example, zinc oxide, antioxidant, peroxide, and Sulphur. Sulphur is used during a process called sulfur vulcanization, which is heating natural rubber or synthetic rubber with sulfur (Mark, Erman, & Roland, 2013), and transforms the rubber from plastic to elastic state. During vulcanization, sulfur bridges are crosslinking polymer chains. The extent of crosslinking and the number of sulfur atoms in the crosslink influence rubber properties (Nasir & Teh, 1988):

- Too many crosslinks can convert the rubber into a hard and brittle material.
- Short crosslinks with less sulfur atoms can improve the rubber's resistance to heat and wear.
- Long crosslinks with more sulfur atoms can improve the rubber's tensile strength.

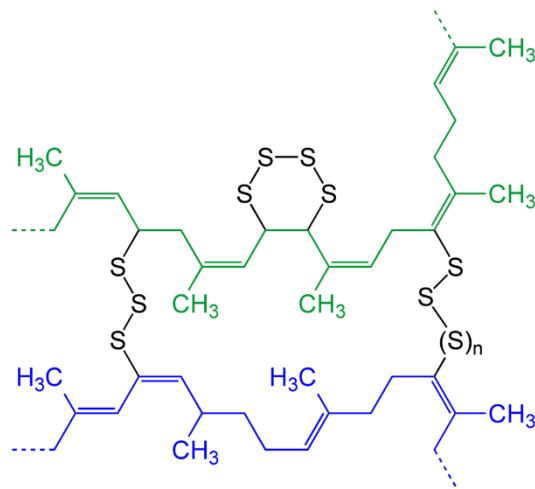


Figure 18. chemical structure of vulcanized natural rubber (Jii, 2011)

2.2.2 Rubber Oxidation

Oxidation worsens physical and mechanical properties of rubbers. During the past 60 years, lots of research has been done to understand the effects of oxygen and ozone on rubber. The heavily chemistry-based theory of rubber oxidation has been explained (Cunneen, 1968) (Shelton, 1972). In this literature review, what will be discussed are the factors that control rubber oxidation kinetics and how oxidation affect rubber properties.

2.2.2.1 Rubber oxidation kinetics

To understand rubber oxidation kinetics, the diffusion limited theory was introduced. Oxidation consumes oxygen that has to diffuse from the rubber surface. Consider the situation when the oxidation rate is high enough, oxygen will be consumed before it completely diffuse through the rubber. This procedure creates oxygen concentration, which leads to a gradient in oxidation through the material (Baldwin & Bauer, 2008). In constant conditions, oxidation rate is relatively constant with time, which can be expressed as:

$$\frac{d[\text{O}_2]}{dt} = -\rho(T)^* \frac{[\text{O}_2]}{1+a[\text{O}_2]} \quad (2.25)$$

When oxygen concentration is low, oxygen consumption rate is proportional to oxygen concentration; at high oxygen concentration, the rate is independent of oxygen concentration. Meanwhile, oxygen concentration is decided by consumption rate and oxygen permeability ρ . Both oxygen consumption rate and permeability are depends on temperature. At high temperatures, oxidation rate becomes faster than permeability, leading to oxygen starvation in the rubber. Since different rubber compounds have different permeability curves, their oxidation rates varies. A finite element kinetic model has been developed to predict oxidation rate of the different layers inside a tire (Ellwood, Baldwin, & Bauer, 2006).

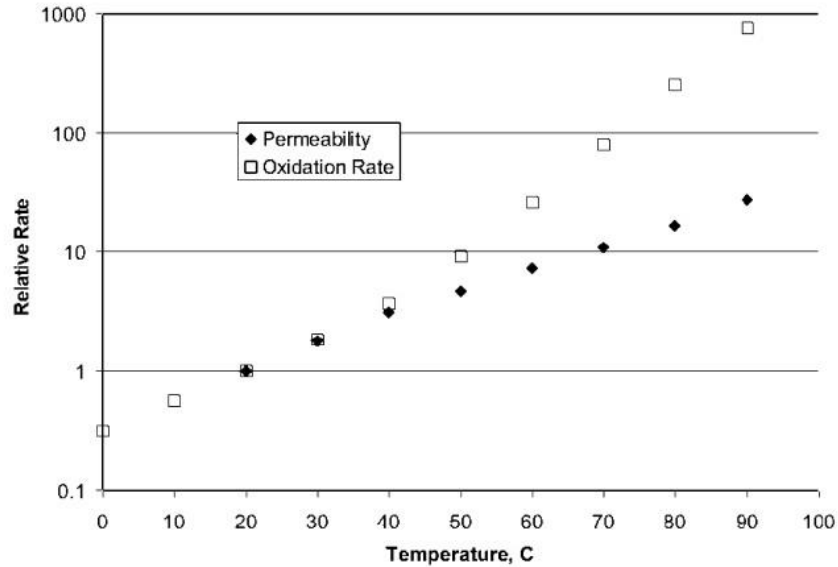


Figure 19. Relative temperature dependence of permeability and oxidation rate of NR (Baldwin & Bauer, 2008)

There are two main theories about the mechanism of protecting rubber from oxidation (Choi, 1997):

- Block method: incorporate a mixture of paraffin waxes (Abu-Abdeen, 2001). The waxes form a protective layer on rubber surface that prevents oxidation.
- Reaction method: stabilizers preferentially react with ozone, so that the rubber is protected. Alkyl and aryl-substituted p-Phenylenediamines stand out among stabilizers because of their ability of preventing thermal oxidation, reducing mechanical-oxidative fatigue, and resisting ozone cracking (Lewis, 1972).

Usually, these two method are combined together to protect rubber from oxidation.

2.2.2.2 Effects of oxidation on rubber properties

To study the effects of oxidation on rubber properties, there are two main source of oxidized rubber: field-retrieved tires and laboratory-aged tires.

Ford Motor Company retrieved over 1500 on-road and spare tires from 6 different vehicle types, 3 tire manufacturers, and 6 cities. Tire ages range from 2 week to 6 years.

Skim rubber crosslink density and peel strength, and wedge rubber modulus and elongation-to-break were measured (Baldwin, Bauer, & Hurley, 2005).

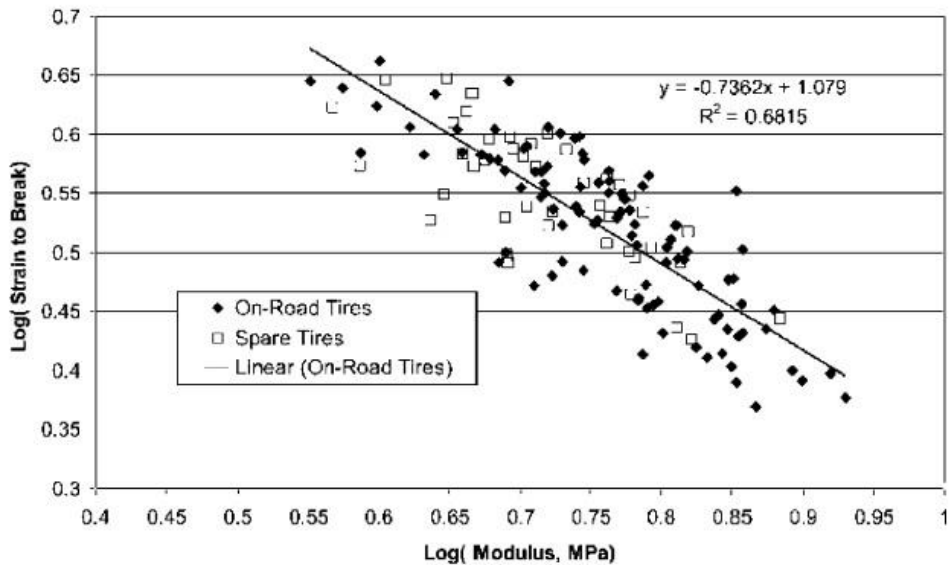


Figure 20. Ahagon plot of retrieved on-road and spare tires

The most important discovery is that both on-road and spare tires were aerobic oxidized. Skim rubber crosslink density and modulus increase with time linearly, indicating a constant oxidation rate. Wedge rubber modulus increase with aging while strain-to-break decrease. The study concludes that spare tires are aging only slightly slower than on-road tires, mileage is less important than time in tire aging. The most important factors are ambient temperature and tire type.

For laboratory-aged tires, researchers indicated that to replicate actual field aging conditions, tires should be mounted on wheels and inflated before aging in oven (Baldwin, Bauer, & Ellwood, 2004). Figure 21 is Ahagon plot of light truck tires aged in oven at 40 - 70 °C for 12 weeks. For tires aged at 70 °C for a long period of time, measurements of cavity air composition indicated that oxygen depletion occurred and the tire deviates from aerobic oxidation.

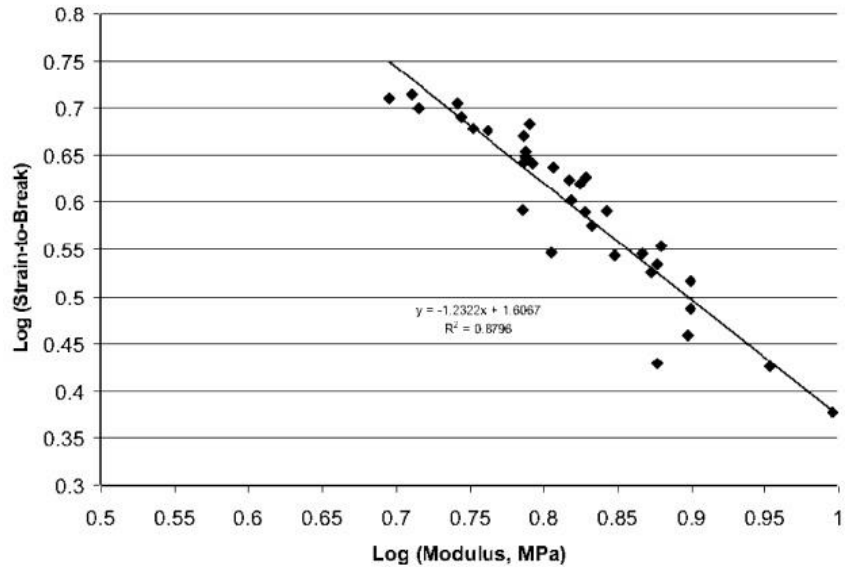


Figure 21. Ahagon plot of oven aged tires (*Baldwin & Bauer, 2008*)

Ford Motor Company aged light truck tires under 40-100 °C, fill gas (100% N₂ to 100% O₂) and up to 2 times of maximum sidewall pressure, as well as tires of different sizes and manufacturers. By comparing the strain-to-break distribution in Figure 20 and Figure 21, it is obvious that strain-to-break of oven aged tires can be fitted to a curve better than that of field-retrieved tires. This advantage of data consistency also applies to other rubber properties, thus researchers were confident to fit oven aged tire data to curves. Such as peel strength vs. shifted time in Figure 22. Oxidation rate vs. oven temperature is shown in Figure 23, as well as FEA prediction. Oxidation rate increase with increasing temperature up to 70 °C, then oxidation rate decreases. From the collected data, researchers also concluded that high pressure and high oxygen concentration can increase oxidation rate, although the increase is small.

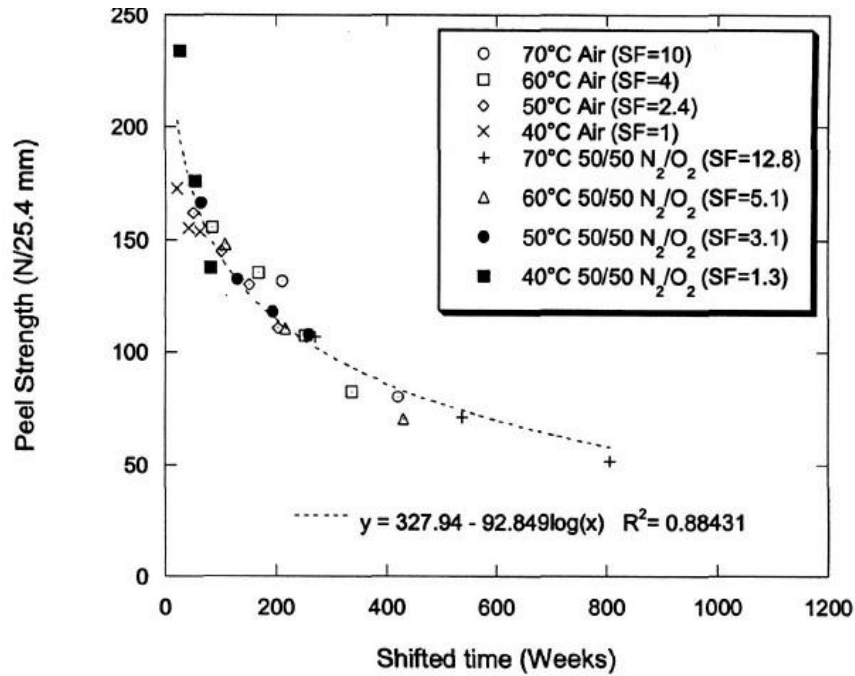


Figure 22. Peel strength vs. shifted time. Shift factors (SF) are in the legend (Baldwin, Bauer, & Ellwood, 2005)

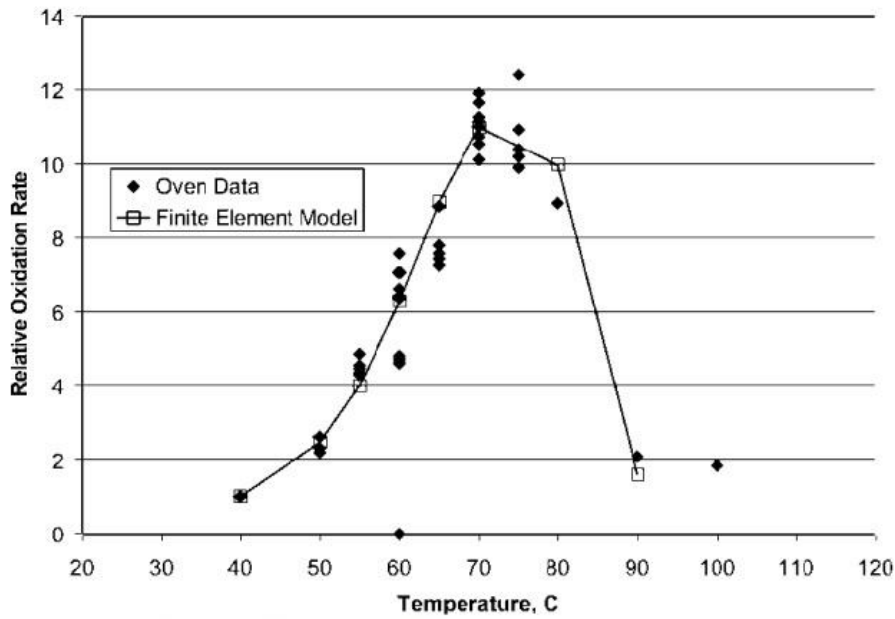


FIG. 12. — Dependence of rubber oxidation on oven temperature.

Figure 23. Dependence of rubber oxidation on oven temperature (Baldwin & Bauer, 2008)

A correlation between oven aging and field aging has been established. 5 tires that have field aging data were oven aged (Bauer, Baldwin, & Ellwood, 2007), including a

small car tire, 3 SUV tires, and a large car tire. From Ahagon analysis, researchers concluded that all properties of the small car tire can be correlated, skim rubber properties of the SUV tires can be correlated, and only wedge rubber elongation-to-break property of the large car tire can be correlated. By analyzing tire properties from oven aging and field, an empirical method was established: oven aging at 65-70 °C can represent field aging, and the acceleration factor is independent of tire size. For example, acceleration factor is 36 when a tire is oven aging at 65 °C using 50/50 blend of N₂/O₂ as the fill gas. Which means that 8 weeks of oven aging under this condition will produce a tire that needs 5.5 years of field aging.

2.3 Rubber/Tire Friction/Wear Test Machines and Methods

Empirical models are always accompanied by tests. During the past decades, along with the progression of research on rubber/tire's friction and wear, numerous friction or wear test machines and methods have been developed. Before getting into details of different test methods, is a brief review of the basic principles of experimental design. After that, several friction/wear test machines and methods are presented, which are divided into three categories: indoor rubber tests, indoor tire tests, and outdoor tire tests. At the end of this section, a summary of all the mentioned test machines and methods is provided. This will show if any of the test setups is capable of controlling and/or measuring all major factors that influence wear.

2.3.1 Principles of Experimental Design

Design of experiments is the design of any task that aims to describe or explain the variation of information under conditions that are hypothesized to reflect the variation (Fisher, 1937). Usually, there are three main concerns:

- **Randomization.** To ensure that each individual has the same weight in the study, in an experiment, individuals should be assigned to groups randomly. This act tends to reduce confounding, which is an unexpected variable that influence both the dependent variable and independent variable (Greenland, Robins, & Pearl, 1999).

- **Replication.** Replication is the repetition of an experimental condition so that the variability associated with the phenomenon can be estimated (Replication (statistics), 2017). Because of variation and measurement uncertainty during measurements, researchers usually repeat measurements and replicate full experiments, so that reliability and validity of the experiment can be improved.
- **Reliability.** Reliability is the overall consistency of measurements. If experiments were repeated and generate same results, it means that the experiments are highly reliable. To distinguish reliability and validity, an example can be used: a load cell for measuring normal loads always shows 10 N more than true value, then the load cell is reliable, but not valid. However, a test that is not reliable cannot be valid (Davidshofer & Murphy, 2005)

2.3.2 Indoor Rubber Tests

Indoor rubber friction tests are fast and economical; thus they are widely conducted on a variety of test machines. Four different indoor rubber testers are described below.

2.3.2.1 JLU Dynamic Frictional Property Test Machine

In Jilin University, an All-weather tire tread-road surface friction property testing system was developed. Main parameters of the machine are listed below (Frictional property tester of JLU, 2012):

- Sampling frequency: 200Hz
- Slip velocity: 8.5 to 150 km/h
- Pressure: 0 to 1.86 MPa
- Environmental chamber temperature: -25 to 50 °C

The system includes console, hydraulic source, motor, rotating disk, pressure disk, hydraulic load cylinder, vertical pressure sensor, environmental chamber, environment control unit, speed sensor, horizontal force sensor, road material, and so on. The pressure disk (5) is mounted under the hydraulic load cylinder (6), tire tread sample (8) is fixed under the pressure disk. During a test, the hydraulic load cylinder drives the pressure disk to move downward, makes the tire tread sample touches road material that is on the rotating disk (4). A horizontal force sensor (14) is installed between pressure

disk and main frame (13), which measures horizontal force of the pressure disk, and friction of sample can be calculated. A vertical pressure sensor (7) is installed between pressure disk and hydraulic load cylinder, which measures vertical force of pressure disk.

This testing system can be used for testing tire tread, acquiring testing curves of variable coefficient between tire tread and different road surfaces under different slip velocity, vertical load, temperature, and humidity.

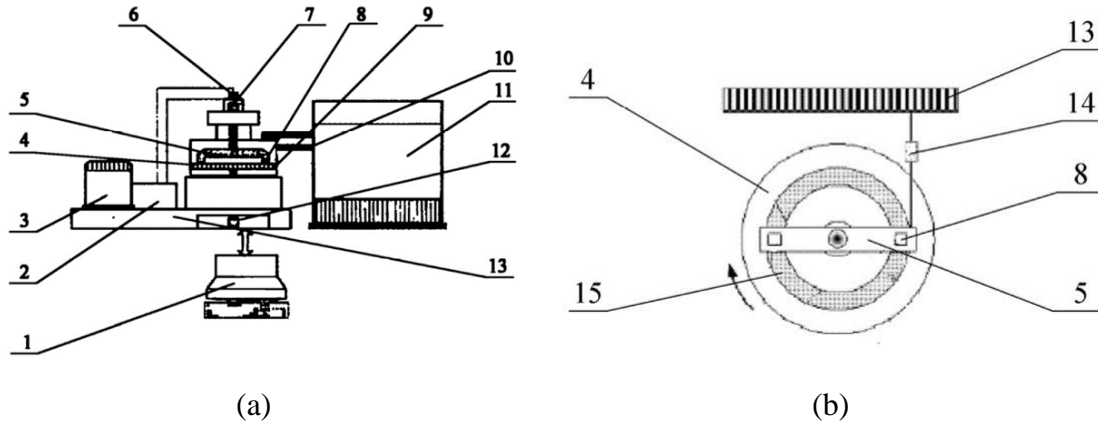


Figure 24. (a) Sketch of the Dynamic Frictional Property Test Machine; (b) Principle of friction measurement (*Frictional property tester of JLU, 2012*)

2.3.2.2 TE 75 Rubber Friction Test Machine

This tester was developed by Phoenix Tribology Ltd. This machine aims at investigating the fully frictional behavior of rubber materials in dry and lubricated environments (George, 2017). Main parameters of the machine are listed below:

- Normal load: 0.1 to 50 N
- Friction force range: 0 to 50 N
- X axis speed range: 0.01 to 10 mm/s
- Y index speed: 10 mm/min maximum

To measure friction coefficient of rubber, it is important to have a well-defined contact geometry. For a flat-on-flat contact between rubber and surface, repeatability is poor because it's difficult to achieve and hold the surfaces flat against each other, during motion, frictional tilt will happen. The TE 75 has the load and force axes at right angles and allows the link to the force transducer to slide vertically, so that the friction force measurement is independent of the degree of misalignment or indentation of rubber

samples. Tests can be carried out with flat-on-flat or ball-on-flat geometry, and the area of contact is defined by the elastic deformation of rubber on a macro scale. The fixed upper sample is loaded with dead weights onto another sample which is mounted on a single axis linear traverse. When the lower sample moves, friction force on the upper sample is measured. Test parameters include speed, stroke, sliding path, load, contact geometry, contact time, lubrication, temperature and humidity. A plastic safety cover acts as a chamber for humidity controlled tests, and has a temperature and humidity sensor mounted inside.

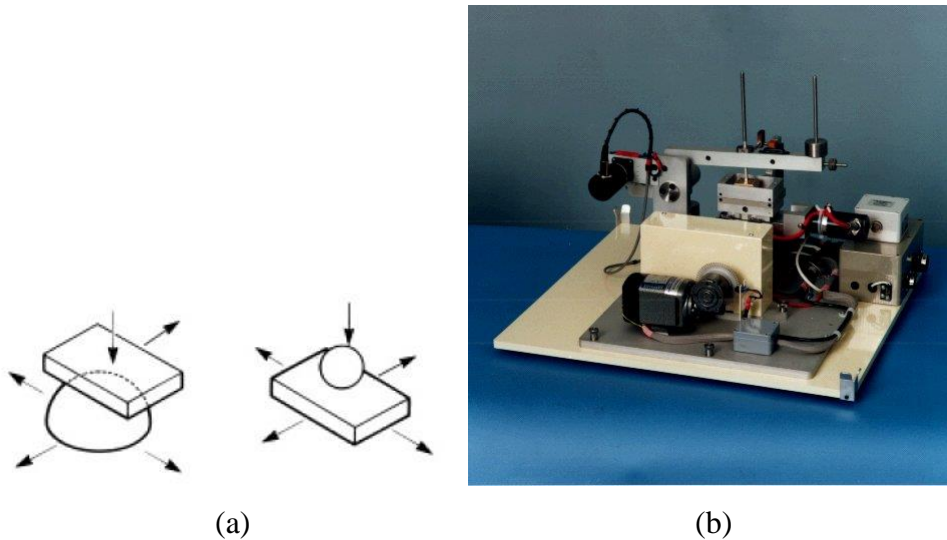


Figure 25. (a) Contact geometries; (b) TE 75 rubber friction test machine (*George, 2017*)

2.3.2.3 High Speed Linear Friction Tester

In Altracon, a system called High Speed Linear Friction Tester (HSLFT) was developed. The HSLFT offers a unique possibility to determine friction coefficients of rubber samples on different surfaces and under various operating conditions in order to predict compound and pattern influences on the grip and traction performance of tires (*Berres & Barz, 2017*). Main parameters of the machine are listed below:

- Normal load: 7500 N
- Sliding distance: 2500 mm
- Sliding velocity: 0 to 8 m/s
- Longitudinal acceleration: 0 to 10 g

The test machine is equipped with a novel linear induction motor, which enables up to 8 m/s sliding velocity and up to 100 m/s² acceleration. To cover the full operating range of passenger car and truck tires, up to 5000 N vertical forces can be applied on specimen.

The most important features of the HSLFT system, is flexibility of testing conditions. Testing surface could be asphalt, concrete, snow and ice surfaces. Wet track and aquaplaning conditions are also possible. After installing the system in a climate chamber, tests can be conducted in a temperature range from -25°C to +40°C.



Figure 26. High Speed Linear Friction Tester (*Berres & Barz, 2017*)

2.3.2.4 LAT100 Compound Tester

This popular testing machine was developed by VMI Tire. LAT100, which is capable of measuring both the abrasion resistance and friction properties of rubber sample under a wide range of conditions (Description – Laboratory Abrasion & Skid Tester, 2014). Rubber samples are solid wheels made of the testing compound, and runs under load on a rotating disk with a slip angle. Disk speed, disk surface, slip angle and load on the sample can vary over a wide range. During laboratory abrasion tests, smearing can occur and lead to wrong results. The LAT100 applies magnesium-oxide powder to the abrasion disk, which binds abraded particles and keeps the disk surface dry and clean.

To cover a wide speed range, the abrasion disk is driven by a servo motor with timing belts, electro-magnetic clutches and a gearbox. The rubber sample holder ensures

that rubber samples contacts the abrasion disk with a 159.15 mm radius from its center, so that each disk revolution means 1 meter of abrasion distance. A tri-axial force transducer is mounted axially to the rubber sample axle to measure load, friction force and side force. The sample load is provided by a low friction pneumatic cylinder and a leverage system. When a test is running, a sliding door in front of the abrasion disk is closed and locked, thus the environment is protected from rubber particles and water spray.



Figure 27. LAT100 Compound Tester (*Description – Laboratory Abrasion & Skid Tester, 2014*)

2.3.3 Indoor Tire Tests

Obviously, to understand tire wear, testing only rubber samples is not enough. As a result, tire testing is necessary. Compared with outdoor tests, indoor tire tests are more economical, and have better repeatability. Here are four examples of indoor tire test machines.

2.3.3.1 Rotating Disc Machine in UNIPD

This tester was built in Motorcycle Dynamics Research Group, university of Padova (Berritta, Cossalter, Doria, & Ruffo, 2002). This testing machine is specially designed for motorcycle tire testing, which requires large camber angles. To achieve more realistic contact patch, instead of a drum, a rotating disc acts as the road surface in this machine. Test wheel is mounted on a hinged arm, the arm makes it possible to set desired side slip and camber angles. The machine is equipped with 3 load cells to measure lateral force, lateral axis moment and vertical axis moment.



Figure 28. Rotating disk machine (*Berritta, Cossalter, Doria, & Ruffo, 2002*)

2.3.3.2 Tire Rolling Resistance Measurement System

This system was developed by MTS for accurate and repeatable results needed to assess tire rolling resistance for a wide variety of tires (Tire Rolling Resistance Measurement System, 2014). The drum is driven by a motor and has sandpaper belt mounted on its surface. To minimize the F_z into F_x cross talk, the reference forces are aligned with drum axis, and the load transducer's output signal is digitally compensated with a calibration matrix. This system-level calibration is able to maximize accuracy. Off-axis loading is minimized by using tight machine tolerances and laser alignment. The tire load mechanism meets class AA load standard to achieve tire load accuracy required by ISO and SAE standards.



Figure 29. MTS Tire Rolling Resistance System (*Tire Rolling Resistance Measurement System, 2014*)

2.3.3.3 Flat-Trac® Tire Test Systems

Virtually every major tire manufacturer and vehicle maker in the world depends on MTS Flat-Trac Tire Test Systems to deliver its most critical tire performance data (Flat-Trac Tire Test Systems, 2014). The system provides access to all important test parameters, like: road speed, tire spindle speed, normal force, lateral force, torque, loaded effective radius, slip angle, inclination angle, and inflation pressure.

On this system, forces and motions are applied to a tire running on a continuous flat belt. The signature robust A-frame carriage ensures extremely low deflections when applying loads on test tires. This geometry also provides a base for wide range of slip angle and inclination angle movement. The radial actuator is mounted in the apex of the A-frame, its piston rod guides the radial motion and allows the tire spindle to steer for slip angle control.

The steel belt is coated with an abrasive surface that provides a flat, simulated road surface. This belt surface is tensioned around two drums, and test tire load is supported by a hydrodynamic water bearing between the drums. This bearing ensures a large stiff and flat testing surface. Tire inflation pressure is also servo controlled using an inflation pressure assembly.



Figure 30. Flat-Trac® Tire Test System (*Flat-Trac Tire Test Systems, 2014*)

2.3.3.4 Tire Tread Wear Simulation System

Developed by MTS, this system offers fast and precise indoor tread wear testing. The system has a specially designed multi-axial sensor package and motion systems, which provides dynamic simultaneous control of normal force, lateral force, torque, and inclination angle. This control enables highly accurate replication of tread wear, and improved correlation between indoor tests and outdoor driving (Tire Tread Wear Simulation System, 2014).

On this system, the 3-meter diameter drum minimizes tire contact patch distortion relative to a flat surface. To remove rubber particles shed from testing tire, a talc delivery system is installed. The talc system sprays controlled volume of talc on the drum surface near the tire contact patch, then talc will coat rubber particles, and extracted by a vacuum system. The result is clean and unchanged roadway surface during a test.

The complicated drive system allows a maximum road wheel speed of 160 km/h, and is capable of handling tractive force from tire braking and driving, as well as drag force from slip angle. To simulate all four tire positions, the system is capable of both forward and reverse rotation.

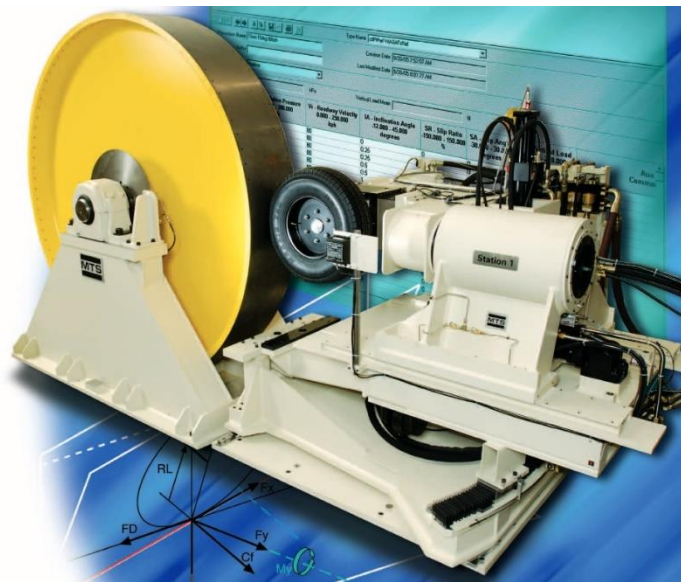


Figure 31. Tire Tread Wear Simulation System (*Tire Tread Wear Simulation System, 2014*)

2.3.4 Outdoor Tire Tests

2.3.4.1 Wheel force transducer

To collect tire data during a road test, a popular method is installing wheel force transducers on testing wheels. With several load cells incorporated inside, a wheel force transducer replaces a standard wheel and measures the forces and moments applied through the tire contact patch (Kistler, 2010). Signals from the load cells are converted into digital form, then transmitted from the rotating wheel to a fixed stator, and then to on-board electronics device, where the three forces and three moments of test tire are calculated.

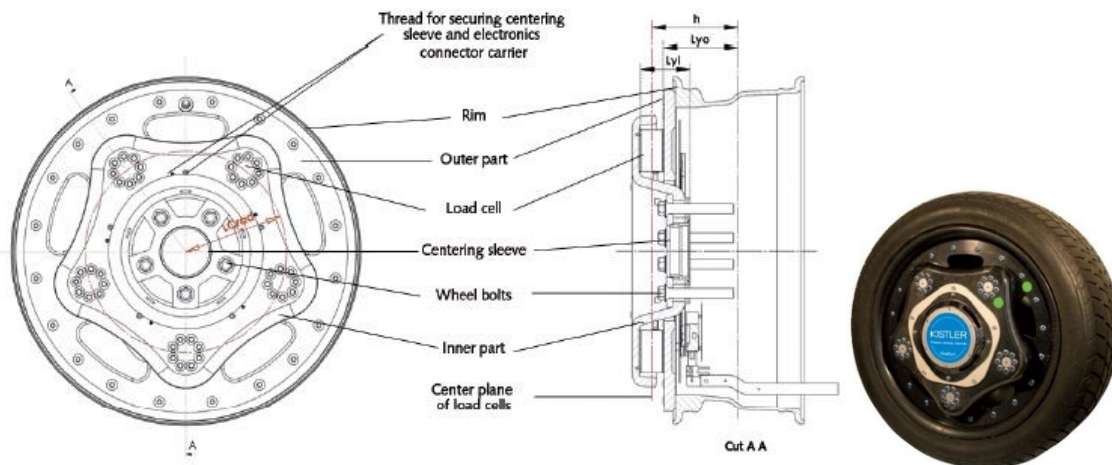


Figure 32. RoaDyn[®] S630 sp System 2000 (Kistler, 2010)

2.3.4.2 ASFT Mk IV Rear -axle

This system was developed by ASFT, aiming at continuous, accurate and reliable friction measurement for the entire length of test surface (Fernando, 2009). Test tire is attached to both reference tires, and braked for 13% slip ratio. Load is provided via a spring arm. The most unique design of this system is that the test tire is not attached to the body of the trailer or vehicle, and is only attached to the rear axle via a spring. This design prevents the test wheel from receiving any disturbance from moments in the vehicle. A water nozzle is located ahead of the test tire to provide uniform thickness of water across the width of the test tire over the full range of test speeds (65 and 96 km/h, within a tolerance of ± 5 km/h).

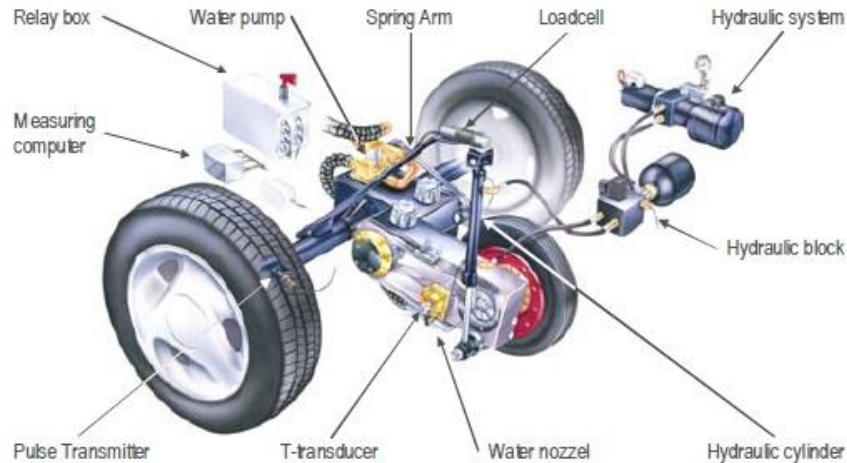


Figure 33. ASFT Mk IV Rear -axle (*Fernando, 2009*)

2.3.4.3 Procedures for tire treadwear testing in Uniform Tire Quality Grading (UTQG)

Created by U.S. Department of Transportation, National Highway Traffic Safety Administration, this is the standard for tire treadwear testing. The UTQG test facility is in San Angelo, Texas.

Before testing, all test tires should be marked with an inventory number, and inspected carefully. Test rims should also be verified by physical measurement and visual inspection. After tires have been mounted, they will be inflated to prescribed pressure with vehicle ballasted with the test load.

A test convoy should consist of maximum of four vehicles, or two vehicles. One vehicle should be equipped with four monitoring tires of the same construction type as the candidate tires. The remaining vehicles should be equipped with the candidate tires (Beebe, 2004). The 400-mile test course consists of three loops: southern loop, eastern loop and northwestern loop, which is shown in the figure below.

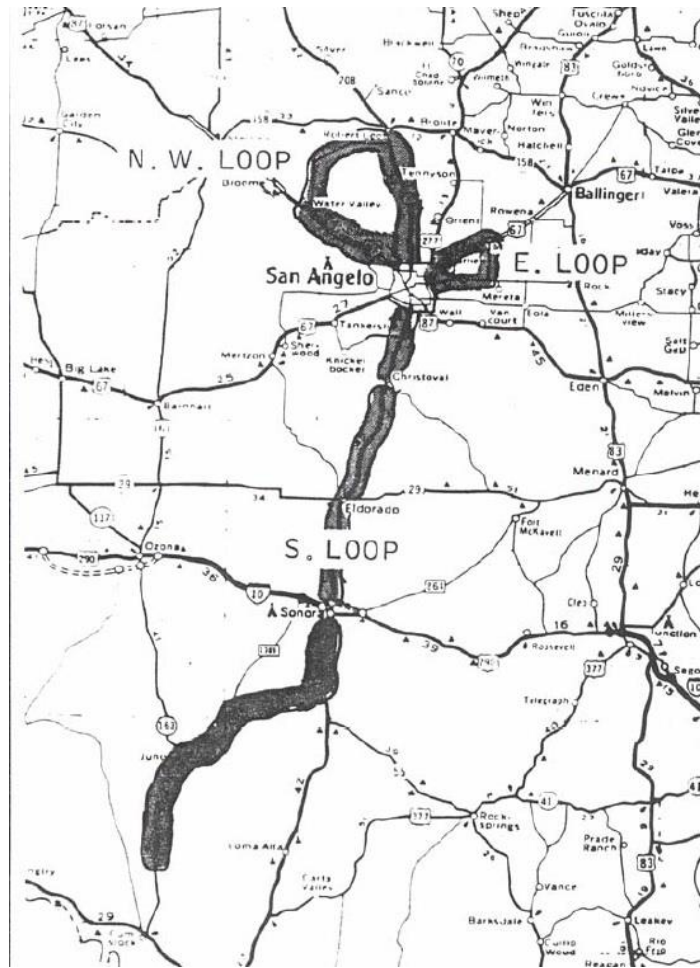


Figure 34. Test course (Beebe, 2004)

During driving, vehicle speed should be maintained as the posted speed limits throughout the course. After the first circuit, testing tires will be rotated using the “Forward X” plan.

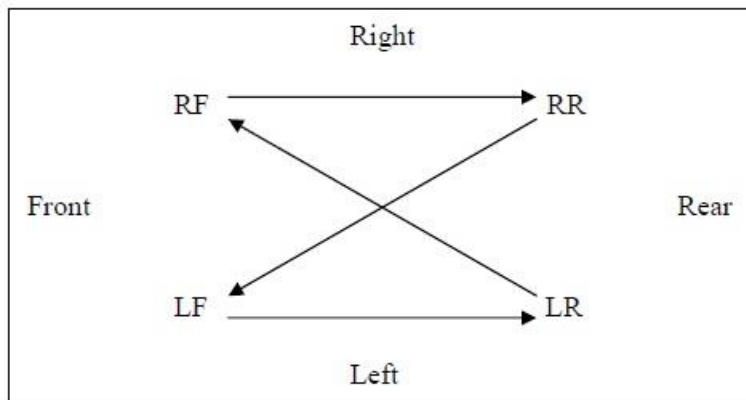


Figure 35. The “Forward X” rotation plan (Beebe, 2004)

After tire rotation, the convoy will be driven on the test course for another circuit, for a total of 800 break-in miles. After that, test tires will be immediately removed from the vehicles and prepared for tread depth measurement.

Before tread depth measurement, test tires will be allowed to cool until they reach the initial inflation pressure or two hours. Also, anything that may impair tread depth measurement, like dirt or stones, should be cleaned. Test tires should be marked across the tread radially at six even spaced locations, where tread depth measurement will take place. When measurement takes place, a digital probe tread depth gauge will be used to measure each tread groove at the six marked locations.

Upon completion of measurement, test tires will be mounted onto their original positions of vehicles. The remaining 6400 miles of test will follow 800-mile increments. For every 800 miles, tread depth measurement procedures will be repeated as follows (Beebe, 2004):

1. Tire removal
2. Tire cleaning
3. Tire pressure check
4. Tire measurement
5. Tire marking
6. Tire rotation
7. Confirm that vehicle load has not changed
8. Check vehicle front end alignment

Before the start of every 800-mile test run increment, the convoy order will be changed: shift each vehicle back by one position, the last vehicle will be placed in the 1st position. After each 1600 miles (exclude the first 800 miles) of test, tires of vehicle number 1 will be mounted on vehicle number 2, tires of vehicle number 2 will be mounted on vehicle number 3, tires of vehicle number 3 will be mounted on vehicle number 4, tires of vehicle number 4 will be mounted on vehicle number 1.

2.3.5 Summary of Wear Test Machines and Methods

JIU Dynamic Frictional Property Test Machine is a good platform for rubber sample wear tests: the machine is capable of controlling three major wear influencing factors: load, sliding velocity, and temperature. Its rotating road ensures changeable road

surface and continuous sample motion in one direction, which is critical for wear testing. However, for our lab, the machine's hydraulic system is too expensive. TE 75 and Altracon HSLFT provides accurate sliding velocity control, but they have one similar problem: due to their linear motion design, continuous sample motion in one direction is not possible, thus are not suitable for sample wear testing. LAT100 is a mature tester that is widely used in industries. With its excellent test condition control, it is almost an ideal platform for rubber sample wear tests. However, wear data collected from LAT100 will miss one critical parameter: sliding velocity. Due to its lacking of sliding velocity control, rubber sample is limited to free rolling and skidding.

The main problem of the rotating disc machine in UNIPD is also lacking sliding velocity control, which makes it not suitable for tire wear testing. Among the three test rigs from MTS, the tire tread wear simulation system is ideal for indoor tire wear tests, but the machine is expensive for even companies.

For outdoor tire wear tests, repeatability is a major concern. If tests are conducted on public road, parameters like temperature, road profile, driving effects (speed, accelerating, braking, turning, etc.) are variable and the repeatability is low. This issue can be solved by running tests on a test track, where the road profile is relatively uniform, and vehicle motion can be much more consistent. To compare UTQG and ASFT Mk IV Rear -axle, it is obvious that the latter one has much better control of parameters like normal load and sliding velocity, therefore a better platform for outdoor tire wear tests.

In conclusion, most test machines are not capable of controlling/measuring all major factors that influence wear, some machines are capable of that but are too expensive. Therefore, we have to design and build our own test machine, which is capable of collecting required wear test data for developing machine learning based wear model, and is economical friendly.

3. Design/build Test Rigs

The first step of developing a machine learning based wear model, is collecting wear data that includes as many wear influencing factors as possible. As mentioned in introduction, both rubber sample and tire wear data should be collected. After reviewing existing wear test rigs, I concluded that it is necessary to design and build our own rubber sample/tire testing machine.

In this chapter, two test machines that were designed for rubber sample and tire wear tests are presented. The first test rig is called dynamic friction tester (DFT), which is designed for rubber sample wear testing. The structure of DFT, main concerns during design fabrication and assembly, and procedures of running sample wear tests are discussed. The second test rig is Trailer-Axle Tire Friction Tester, which is designed for on-road tire wear test. Its structure, main concerns during design, and why it was not fabricated, are explained. Tire wear data will be collected from a modified rolling resistance machine, which is a collaboration work of our lab members. The machine's structure, main concerns during design is presented in this chapter.

3.1 Design and build the Dynamic Friction Tester (DFT)

With a good understanding of factors that affect rubber abrasion, requirements of a new rubber sample wear test rig were decided. The new test rig should be able to control/measure these parameters:

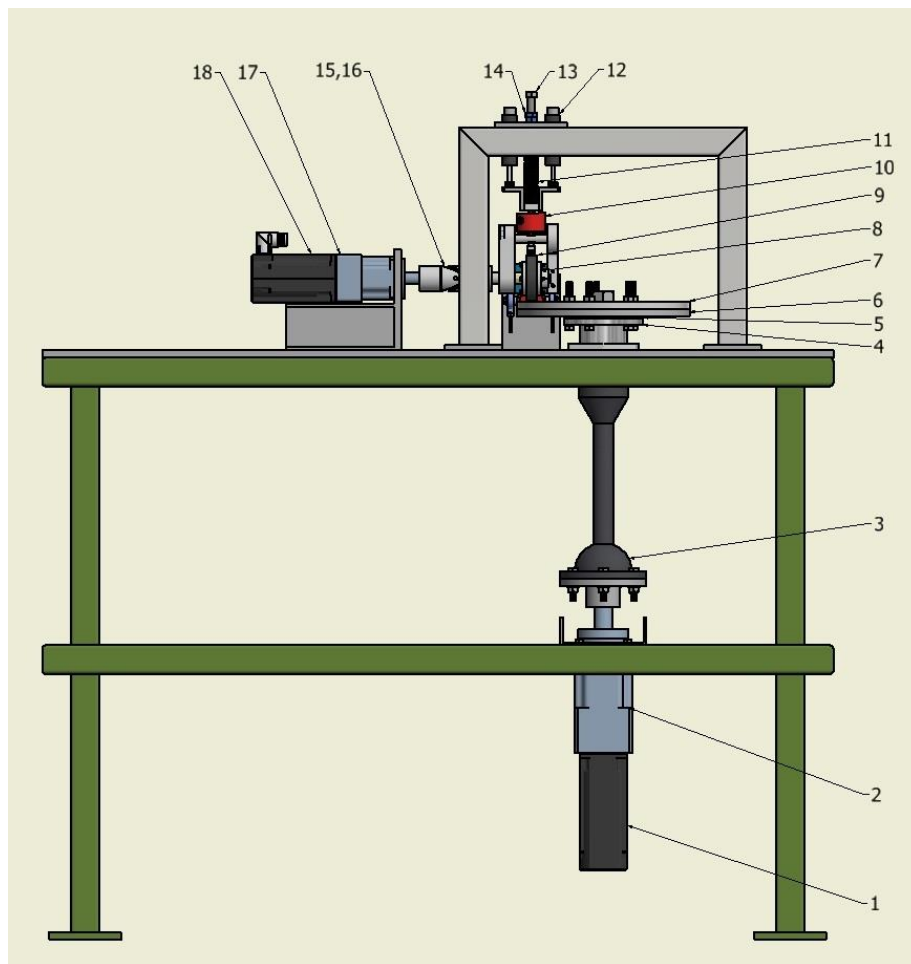
- contact patch pressure,
- flash temperature at contact patch,
- slip angle,
- sliding velocity,
- speed,
- road surface profile

3.1.1 Structure of the DFT

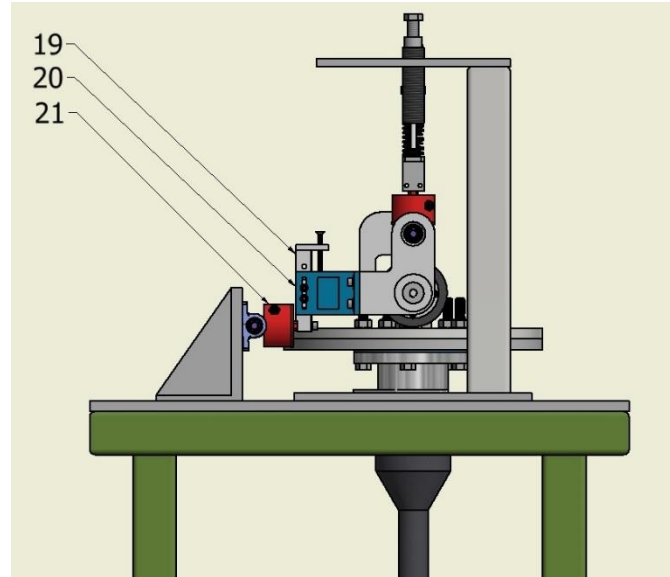
Basic structure of the DFT is illustrated in Figure 36. Drive force from disk motor (1) is transmitted to road disk (5) via disk gearhead (2), half shaft (3) and hub (4).

Meanwhile, drive force from sample drive motor (18) is transmitted to rubber sample (8)

via sample gearhead (17), universal joint (16) and drive shaft (15). Rubber sample runs on changeable surface disk (6), and thickness difference of surface disks is compensated by spacers (5) underneath road disk. Normal load is measured by a load cell (9) that sits right above rubber sample. And normal load is provided by a die spring (11). The spring and two dampers (12) compensate for sample vibration during tests. Another load cell (21) is used for measuring longitudinal friction force. This load cell is able to slide up and down against a rail in part (20), so that the center line of the load cell is kept at the same height as contact patch between sample and surface disk. A temperature sensor measures the temperature of rubber surface as it leaves the contact patch, and a vacuum cleaner cleans rubber particles generated during wear tests. A blower that blows cold air prevents rubber sample from getting warm. The temperature sensor, vacuum cleaner and blower are not shown in the drawings.



(a)



(b)

Figure 36. Front view (a) and left view (b) of the DFT

Main testing parameters of the DFT are as follows:

- Sampling frequency: 1000 Hz
- Normal load: 0 to 100 lb
- Slip velocity: -0.5 to 0.5 km/h
- Road surface: changeable surface, including sandpaper, and other materials that can be made into a 12 inch diameter disk with less than 0.75 inch thickness.

To compare the capability of DFT with design requirements, we have:

- Contact patch pressure: normal load on the DFT is controlled and measured, contact patch area under different normal loads can be measured via independent tests. Thus contact patch pressure is acquired.
- Flash temperature at contact patch: measured by a temperature sensor.
- Slip angle: due to the increasing complexity of design, slip angle of rubber samples is fixed at zero degree.
- Sliding velocity: the road disk and sample are driven independently by servomotors, whose rotating speed can be controlled and measured.
- Speed: same as above.

- Road surface profile: on the friction tester, sandpaper or any other material that can be made into a 12-inch disk with less than 0.5 inch thickness, can be mounted on the road disk as road surface. Surface profile of the material is measured by a Nanovea JR25 profilometer in our lab.

Thus, the DFT can fulfill all requirements of the new test rig. In the following sections, realization of design requirements is explained in details.

3.1.2 Choice of Sample Shape and Motion Type

The first concern of the design, is to choose proper rubber sample shape and type of motion. This is crucial for collecting desired wear data. From literature review, comparison of different solutions is listed in Table 1.

Table 1. Comparison of sample shapes and types of motion

| Sample shape | Motion | Road surface | Pros | Cons |
|--------------|----------|--------------|--|--|
| square | sliding | stationary | 1. high sliding velocity | 1. short running distance 2. difficult to cool sample |
| square | sliding | rotating | 1. high sliding velocity 2. long running distance | 1. difficult to cool sample |
| round | rotating | rotating | 1. long running distance 2. easy cooling | 1. low sliding velocity |

The most important criteria are “running distance” and “sample cooling”. Wear tests require continuous motion that lasts several minutes, which means several hundred meters of running distance. Thus, a rotating disk is the better solution for the base of road surface. During a 1 minute rubber sample wear test in room temperature, rubber sample’s surface temperature can rise to 60 °C or even higher. Since temperature of rubber sample

has a significant impact on its properties and wear rate, sample must be cooled during tests, otherwise the change of test parameters will be out of control. For a rotating round sample, when a certain area leaves the contact patch, that area can be cooled before it enters the contact patch in the next rotation.

A rotating disk also makes removing rubber particles easier. If not removed, wear particles generated from test which accumulate on the road surface, and change the actual road profile. For a rotating disk, rubber sample can run on one area of the disk, a vacuum cleaner can collect all rubber particles from another area of the disk.

The final choice of rubber sample is an 80-mm diameter, 20-mm thick round sample. Dimension of these rubber samples is identical with samples for the widely used LAT100 tester, thus we can easily acquire samples from industry mentors. The base of road surface is a 12-inch diameter aluminum disk, where different materials (e.g. sand paper) can be mounted as the road surface.

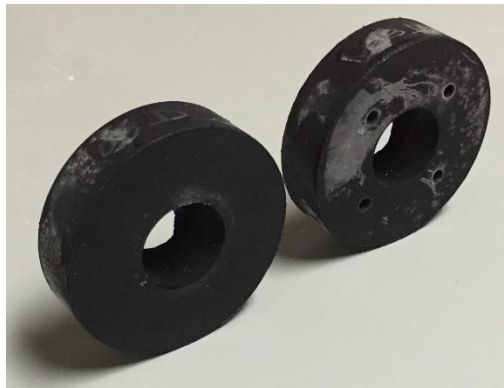


Figure 37. Rubber samples

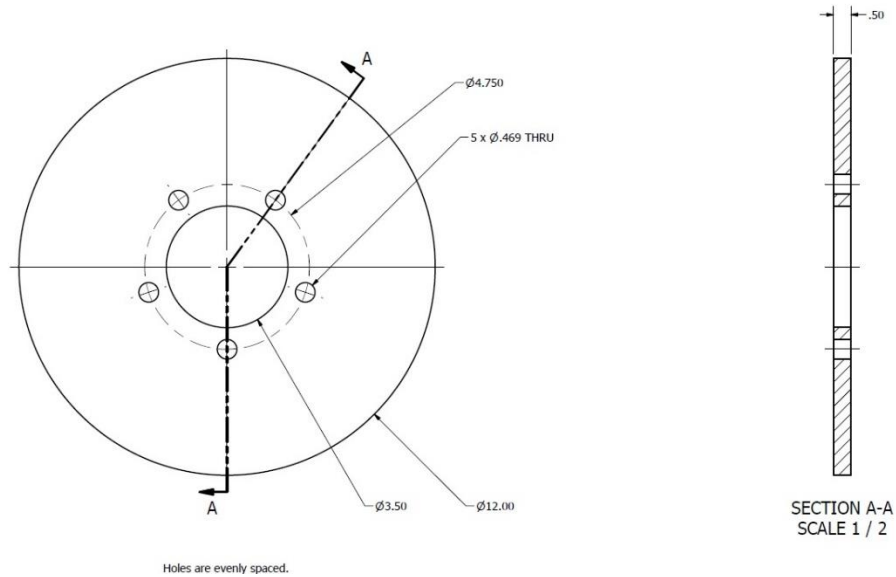


Figure 38. Base of road surface

3.1.3 Sliding Velocity Control

To maintain a steady sliding velocity during a test, the road disk and rubber sample are each driven by a servo motor:

- Disk motor: Kollmorgen AKM 44, with controller and gearhead.
- Sample motor: Kollmorgen AKM 42, with controller and gearhead.

Each servo motor is controlled by a Kollmorgen AKD servo drive. Servo motions are configured via Kollmorgen WorkBench on a laptop.



Figure 39. Kollmorgen AKM 4x servomotor

Before tests, based on distance from disk center to contact patch center L_{DC} , rubber sample effect radius R_C , and required sliding velocity v_s , RPM of both servo motors are calculated. To monitor the actual sliding velocity during every test, both motor shaft's position are recorded at 1 kHz.

3.1.4 Loading Mechanism

The loading mechanism, which applies normal load on rubber samples, is crucial for wear tests. During a wear test, dramatically fluctuating normal load will result in fluctuating contact patch area, which leads to even more unpredictable influence on wear rate. Comparisons of possible loading mechanisms are listed in Table 2.

Table 2. Comparisons of different loading mechanism

| | Pros | Cons |
|----------------------------|--|--|
| Hydraulic | High normal load; Steady load | Difficult to set up; Very expensive; Oil contamination |
| Elec Actuator | Easy to use; Moderate cost | Fluctuating load |
| Spring & damper | Easy to use; Low cost; Steady load | Low normal load |

Hydraulic actuators are widely used in industry, and they offer excellent loading performance: very high and steady load. However, the price and maintenance fee are too high. Also, after long time of use, hydraulic oil will leak inevitably and contaminate surroundings. Electric actuators are not expensive, and there is little difficulty in using them. But during a wear test, electric actuator cannot react fast enough to rubber sample vibration, which results in fluctuating normal load.

In the end, spring & dampers is chosen as the loading mechanism, which are capable of providing up to 200 lbs. of load. The core of this mechanism is the die spring in the center, which provides the desired normal loads. Function of the two dampers is reducing sample vibration during tests, and maintaining the stability of the applied normal load.



Figure 40. Loading mechanism

3.1.5 Wear Measurement

After each test, the amount of rubber sample wear should be calculated. Either sample weight or sample dimension can be measured as wear criterion. There are three steps of preparation before wear measurements:

1. Release loads. Load on rubber sample will cause deformation, which results in wrong dimension measurement.
2. Clean rubber sample. After wear test, there will be a coating of rubber particles covering the rubber sample. Basically, these rubber particles are the result of wear process, and should be excluded from measurements.
3. Check rubber sample's surface temperature. Although rubber sample will be continuously cooled during a test, its surface temperature will still be different from room temperature. As a result, before wear measurement, it is necessary to check rubber sample's surface temperature and bringing it back to room temperature.

Measuring sample weight is straight forward, the only requirement is to design a light-weight hub that hold the rubber sample and can be easily removed from the tester.

When it comes to dimension measurement, there are two approaches:

1. Use laser beams to measure the distance between a reference point and rubber sample surface.

2. Take pictures of rubber sample after each test, use image processing software (e.g. ImageJ (Ferreira & Rasband, 2012)) to acquire change of sample diameter.

The biggest advantage of dimension measurement approaches, is that rubber sample does not have to be removed from the tester. However, the rubber sample needs to be cleaned and cooled before measurement, which is easier to be done when rubber sample is removed. However, dimension measurement has higher cost (laser measurement device or camera) and doesn't have any significant advantage in data accuracy or preparation time cost.

The final choice is using sample weight as the criterion of wear. A light weight hub was designed for fast sample removal.

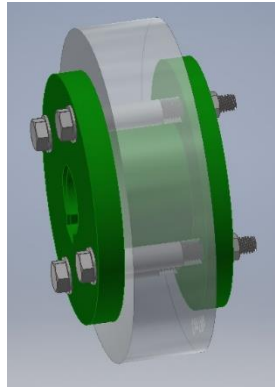


Figure 41. Rubber sample hub (transparent part is rubber sample)

Weight of rubber sample is measured by a LW Measurements HRB-303 high resolution balance, which has a measuring capacity of 300g, and resolution of 0.001g.



Figure 42. HRB-303 high resolution balance (Lim, 2016)

3.1.6 Sensors on the DFT

3.1.6.1 Load cells

There are two FUTEK LCF300 load cells on the friction tester for measuring forces: normal load on rubber sample and longitudinal friction force of rubber sample. Their main specifications are (lcf300, 2016):

- Capacity: 500 lb (normal load measurement), 250 lb (longitudinal friction force),
- Nonlinearity: $\pm 0.25\%$ of RO,
- Nonrepeatability: $\pm 0.05\%$ of RO,
- Rated output: 1mV/V (250 lb), 2mV/V (500lb),
- Maximum excitation: 20 V.

Mounting positions of the load cells are shown in the pictures. Normal load sensor is installed between loading mechanism and sample hub. To acquire actual normal load, weight of sample hub is added to readings of normal load sensor. Height of the friction sensor is adjusted until its center is at the same height as the sample's contact patch.

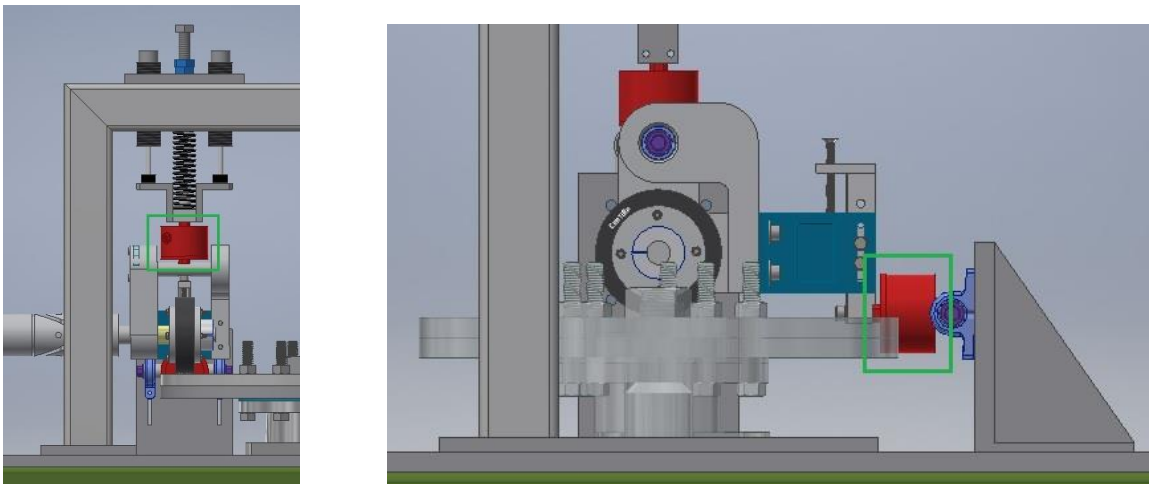


Figure 43. Load cells measuring normal load and longitudinal friction force (highlighted in green squares)

3.1.6.2 Temperature sensor

It is almost impossible to directly measure the temperature of the contact patch. Instead, temperature of rubber sample surface that just left the contact patch is recorded.

The temperature sensor is an Omega OS136-1-MVC non-contact infrared temperature sensor. Its main specifications are:

- Range: -18 to 204 °C,
- Accuracy (at 22 °C ambient): 3% of Reading or 4.4 °C, whichever is greater,
- Response time: 150 msec, 0 to 63% of final value,
- MVC: 10 mV/°C,

Frequency of temperature data collection is 1000Hz.

3.1.7 Procedures of Rubber Sample Wear Test

After numerous friction and wear tests on the DFT, test procedures are optimized and finalized as follows:

1. One day before running tests, take out rubber samples from refrigerator, leave them in room temperature.
2. Before tests, record room temperature, rubber sample compound label.
3. Configure LabVIEW front panel for data collecting. Temperature sensor needs 2 minutes to warm up.
4. For new samples, mount it on the hub, then run under 0.1m/s sliding velocity, 50 lb normal load for 30 seconds. Clean the samples, remove it from the hub, measure its weight for three times, and mount it back on the hub.
5. Measure the weight of sample + hub assembly for three times, measure sample diameter for three times.
6. Insert the sample + hub assembly into the drive shaft, tighten the shaft collar.
7. Based on test parameters, calculate RPMs of both servo motor, enter the values into Kollmorgen workbench. Then enable both motors and reset shaft positions.
8. Start data collection in LabVIEW, adjust normal load to required value.
9. Start servo motors, vacuum cleaner and cooling system.
10. When both servo motors stop running, stop data collection in LabVIEW. Then stop vacuum cleaner and cooling system.

11. Release load on rubber sample, remove the sample + hub assembly. Clean the sample.
12. Measure the weight of sample + hub assembly for three times. Then measure sample's diameter for three times.
13. Repeat step 6 to 12, until all test parameter combinations are finished.
14. Put rubber samples back into refrigerator, clean up the test area.

The following software are necessary for running wear tests and recording data: Excel, MATLAB, LabVIEW, and Kollmorgen WorkBench.



Figure 44. Dynamic Friction Tester

3.2 Design of the Trailer-Axle Tire Friction Tester

Wear data from a standard tire wear test -- UTQG, is not ideal for training machine learned based wear model. There are two reasons:

- Although test vehicle is ballasted, actual normal load on test tire will fluctuate.
- Slip ratio is not controlled, and is heavily affected by traffic, which is random and unpredictable.

Based on factors that affect tire wear, requirements for the new test rig were decided. The new test rig should be able to control/measure these data:

- Contact patch pressure,
- Pneumatic pressure,
- Flash temperature at contact patch,
- Slip angle,
- Sliding velocity,
- Speed,
- Road surface profile,
- Wear rate.

Meanwhile, since tires are getting bigger and bigger these days, the test rig should be able to test tires up to 20 inches in diameter.

3.2.1 Structure

There are three basic component of the whole system:

- Pickup truck;
- Trailer;
- Test rig.



Figure 45. Trailer in our lab

The truck has two main roles: drag the trailer and run at desired speeds, and carry a generator that provide electricity for the test rig. The trailer is where test rig and controllers are installed.

The whole test rig will be installed on the trailer's axle, and has no connection to the trailer body. This design ensures the advantage of preventing moments from the trailer body affecting the test tire. Base (3) is firmly installed on trailer's axle, and act as foundation of all the other components. Servo motor (4) is installed on the base, and provides torque to maintain desired sliding velocity for test tires. Sprockets (5) transfer drive force from servo motor to test tire (7). The sprockets also reduce RPM and increase torque. Test tires are mounted on wheel hub (6), which can fit tires of different sizes. Normal load is provided by an airbag (2), which also serves as a damper. When test is not running, the elevation system (1) lift test tire from the ground, thus prevents unnecessary tire wear. A temperature sensor (not shown in the figure) measures temperature of tire surface aft of contact patch.

Wear measurement follows the standard procedures of UTQG. Test tire is cleaned and cooled before each measurement. The tire is marked across the tread radially at six evenly spaced locations. A tire tread gauge is used to measure tread depths of every tread at these six locations.

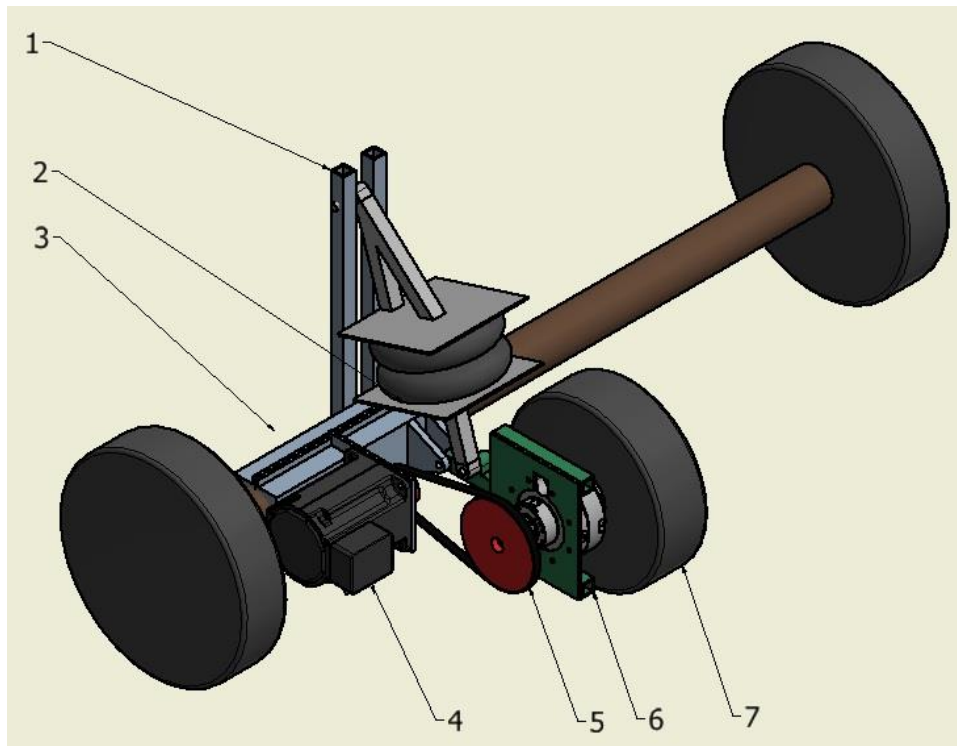


Figure 46. Trailer-Axle Tire Friction Tester

To compare the capability of Trailer-Axle Tire Friction Tester with design requirements, we have:

- Contact patch pressure: normal load is controlled and measured by an air spring, contact patch area under different normal load can be measured via independent tests. Thus contact patch pressure is acquired.
- Pneumatic pressure: measured before and after tests.
- Flash temperature at contact patch: measured by a temperature sensor.
- Slip angle: due to the increasing complexity of design, slip angle is fixed at zero degree. If a certain slip angle is needed, the truck will running under a fixed turning angle.
- Sliding velocity: test tire is driven by a servomotor, thus its rotating speed can be controlled and measured.
- Speed: vehicle speed is measured by a speed sensor.
- Road surface profile: using a Nanovea JR25 profilometer, road profile on different parts of the test course will be measured.
- Wear rate.

Thus, the Trailer-Axle Tire Friction Tester can fulfill most requirements of the new test rig.

3.2.2 Key Components

3.2.2.1 Sliding velocity control

To maintain a steady sliding velocity during wear tests, the test tire is connected with a Kollmorgen AKM 83 servomotor. The motor has enough torque output to maintain anticipated sliding velocity during tests.

When test is running, vehicle velocity measured by a VBOX speed sensor is sent to LabVIEW. After computing correct servomotor RPM for desired sliding velocity under current vehicle velocity, a signal is sent to an AKD servo drive, which controls motions of the servomotor. Meanwhile, since test tire is connected with the motor, its angular velocity can be easily calculated from motor's output signal. Thus no extra sensor is needed for tire speed measurement.

3.2.2.2 Loading mechanism

Normal load on test tire is provided by an airbag, which is connected with a gas tank and an outlet valve. This mechanism is capable of providing desired normal load, with acceptable cost of space and electricity. Also, the airbag acts as a suspension to reduce vibration of test tires.

When test is running, normal load measured by a load transducer is sent to LabVIEW. If current normal load is lower than desired value, gas tank infuse more gas into the airbag; if current normal load is higher than desired value, the outlet valve is opened to allow gas escaping.

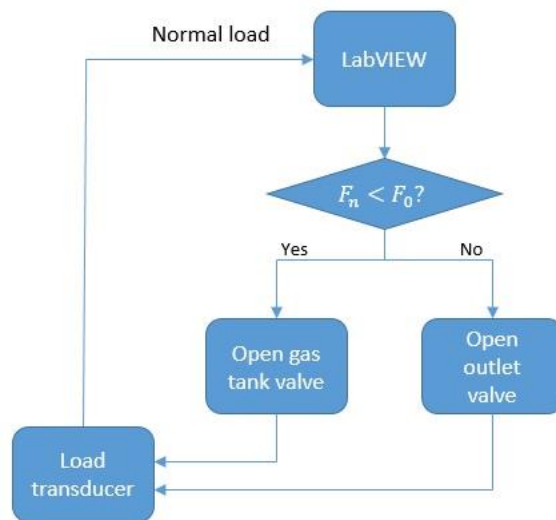


Figure 47. Normal load control

3.2.3 Sensors on the Trailer-Axle Tire Friction Tester

3.2.3.1 VBOX speed sensor

To measure vehicle velocity, a VBOX speed sensor will be installed on trailer roof to measure the trailer's velocity. Its main specifications are:

- Accuracy: 0.1 km/h
- Sampling frequency: 5| 10| 20| 100 Hz
- Maximum velocity: 1609 km/h
- Minimum velocity: 0.1 km/h
- Resolution: 0.01 km/h



Figure 48. VBOX speed sensor

3.2.3.2 Wheel load transducer

To measure normal load and friction on test tires, a LW12.8 Wheel Load Transducer will be installed on the test tire. The transducer collects data for vertical, lateral and longitudinal forces, and also measure camber, steer, and torque moments. It is much lighter than a force hub, and occupy less space. The LW 12.8 Wheel Load Transducer's main specifications are:

- Radial force capacity: 53.4 kN,
- Lateral force capacity: 26.7 kN,
- Nonlinearity: $\leq 0.5\%$ of full scale output,
- Hysteresis: $< 0.5\%$ of full scale output.



Figure 49. LW12.8 Wheel Load Transducer and its application (*LW12.8, 2017*)

3.2.3.3 Temperature sensor

Since measuring temperature at contact patch is almost impossible, temperature of tire surface aft of contact patch is recorded as an approximate of contact patch pressure. The temperature sensor is an Omega OS136-1-MVC non-contact infrared temperature sensor, same as the one on DFT.

3.2.4 Issues of the Design

Compared with traditional tire wear test methods, the Trailer-Axle Tire Friction Tester can collect wear data under much better controlled conditions. However, it still may not be an ideal source of wear data for training machine learning based tire wear model.

The dominating problem is repeatability. If wear tests are carried out in public roads, the 7200 miles of testing will take about 15 days. During this 15 days, a lot of conditions will change. For example, tire wear is influenced by humidity of the road, which will change during this long time period. Also, since the humidity on public roads keep changing, there is no good method to quantify the humidity of the whole test course. Similar problem happens on road profile. Although road profile can be sampled and measured for the whole test course, the slow speed of profiling and large number of samples (different roads, different lanes, profile changes at the same spot) makes it extremely difficult. If we have long-term access to a test track in car/tire companies, whose surface profile is much more uniform than public road, the Trailer-Axle Tire Friction Tester could be a good solution of collecting tire wear data.

As a result, the plan of building the Trailer-Axle Tire Friction Tester postponed to a late date. Tire wear data will be collected from indoor testing machines.

3.3 Modification of the Rolling Resistance Machine for Wear Testing

As was mentioned in the previous section, an indoor wear test machine is needed to perform tire wear tests. However, this kind of test equipment is expensive and it is also nearly impossible to get tire wear data from tire companies. In order to overcome these obstacles, the rolling resistance machine currently installed in CenTiRe Lab, was redesigned to have a new loading mechanism and camber and slip angle input capabilities. With the help of several lab members, the rig was successfully redesigned and reassembled. Now this modified rolling resistance machine is capable of rolling resistance tests, force and moment tests, and wear tests.

The original rolling resistance machine could only conduct rolling resistance tests. Its tire loading mechanism included dead weight and a lever system to apply desired load on test tires. Comparison of the original and modified machine is listed in Table 3.

Table 3. Comparison of original and modified rolling resistance machine

| | Original machine | Modified machine |
|-------------------|-------------------------|--|
| Drum speed | 80mph | 80mph |
| Tire sizes | - | 14" to 17" |
| Camber angle | - | $\pm 10^\circ$ |
| Slip angle | - | $\pm 15^\circ$ |
| Loading mechanism | Dead weight and lever | Motor driven screw |
| Test capabilities | Rolling resistance test | Rolling resistance test, slip test, cleat test, F&M tests, and wear test |

3.3.1 Structure

The rolling resistance machine consists of 4 main components: base, drum, drive motor, and loading mechanism.

- Base. The base is where the drum and loading mechanism are installed. To reduce vibration, some clearance is kept between the base and floor using bolts. Then the gap is filled with grout.



Figure 50. Vibration isolation of the machine

- Drum. A 5.5 feet diameter, 12 inch wide steel drum sits on the base. Sandpaper or other materials can be attached to the surface of the drum as road surface in tire tests.
- Drive motor. A 60 hp DC motor is placed vertically to the machine base. This motor drives the drum.
- Tire placement control mechanism. In the original machine, tire loading mechanism used dead weight and a lever. After the modification, tire placement control mechanism consists of two parts: tire positioning mechanism and loading mechanism.

3.3.1.1 Tire positioning mechanism

The tire positioning mechanism is where tire will be mounted. This mechanism also controls test parameters like slip angle and camber angle. According to SAE J1269, the mechanism should be rigid enough to hold the slip angle within $\pm 0.1^\circ$ and the camber angle within $\pm 0.3^\circ$. Since it is beneficial to have uncoupled tire positioning, slip angle change and camber angle change (Langer & Potts, 1980), the mechanism was designed based on this idea and consists of six main components: force hub mount (1), box assembly (2), beam (3), rear box (4), supporting plates (5), and reaction rod (6).

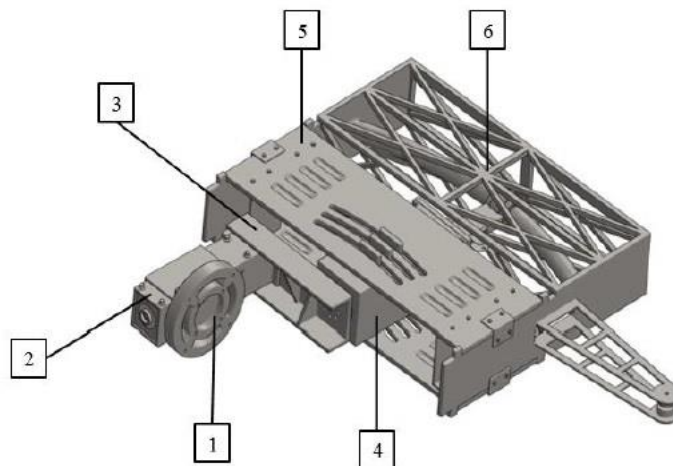


Figure 51. Tire positioning mechanism (Ramdasi, 2016)

The force hub mount (1) is where a force transducer and test tire are mounted. Main function of the box assembly (2) is to provide structural stiffness against lateral force acting on test tire. Inside the box assembly, there is a ball screw, which helps

positioning test tire radially with respect to the drum. The beam (3) compensates for the tire offset cause by the box assembly, thus center the slip angle about test tire's contact patch. Inside the rear box (4), there is a spline gearbox, whose output flange is bolted to the beam to change test tire's slip angle. Driven by a linear actuator, the rear box can slide between the supporting plates (5), thus change chamber angle of test tire. The back end of the rear box is connected with a reaction rod collar, which slides on a reaction rod (6). The usage of reaction rod ensures better normal load distribution from the loading mechanism to test tire. The whole assembly of tire positioning mechanism is sliding on linear bearings which are mounted to the machine base.

3.3.1.2 Tire loading mechanism

Based on SAE J2730, the loading mechanism should be capable of applying a maximum of 25000 N normal load. There are several potential ways to apply normal loads on test tires. The original dead weight & lever system is not accurate and cannot be automated. As discussed in previous sections, hydraulic system is too expensive and difficult to use in our lab. Screws driven by motor can provide high normal load, but their response is too slow. Compared to these methods, pneumatic systems is compact, fast-reacting, and easy to use. However, this kind of system is not rigid enough for cleat tests, during which large forces in the normal direction will generated when test tire passes over a cleat.

In the end, a motor driven screw is chosen as the loading mechanism. The output shaft of an AC motor is connected with a worm gearbox. Then the enhanced drive torque is transmitted to a lead screw. When the screw is driven, the motion is transmitted to the structure of tire positioning mechanism to apply desired normal load.

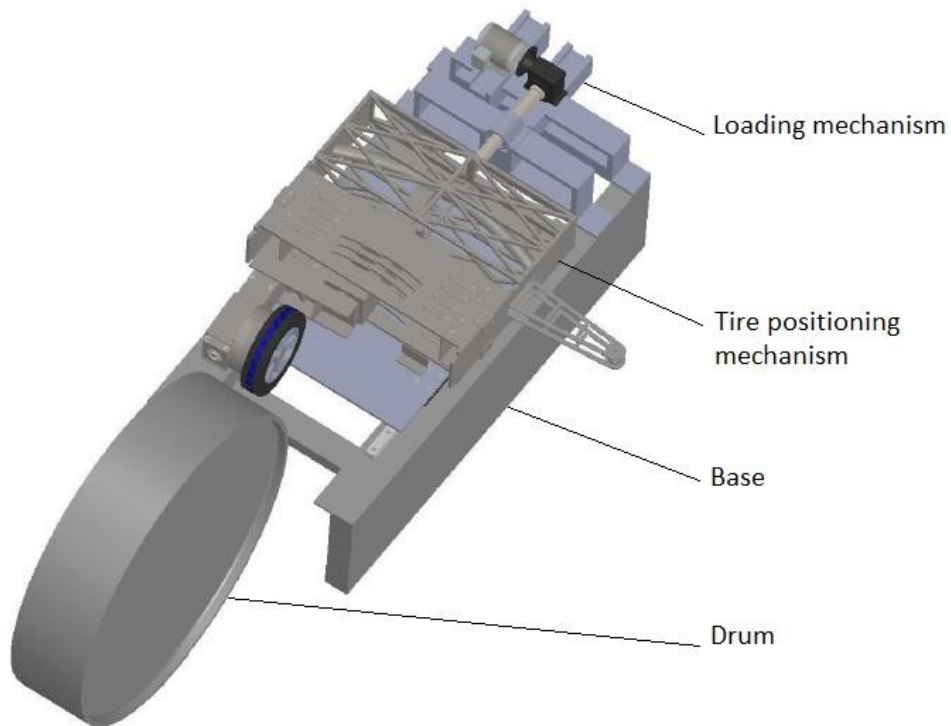


Figure 52. Modified rolling resistance machine (drive motor not included)

3.3.2 Sensors

Sensor selection for the rolling resistance machine are listed as below:

- LW 12.8 wheel load transducer. The same sensor as the one on the Trailer-Axle Tire Friction Tester. This load transducer collects data for vertical, lateral and longitudinal forces, and also measure camber, steer, and torque moments.
- OS136-1-MVC temperature sensor. A Same sensor is installed on the DFT. As an approximation of contact patch temperature, this temperature sensor will collect temperature data of tire surface that just leave the contact patch.
- LCF 450 load cell. To monitor the applied normal load, this load cell is installed between the tire positioning mechanism and loading mechanism.

The main specifications are:

- Capacity: 5000 lb,
- Nonlinearity: $\pm 0.1\%$ of RO,

- Nonrepeatability: $\pm 0.02\%$ of RO,
- Rated output: 2 mV/V nom,
- Maximum excitation: 20 V.

3.3.3 Comparison with Trailer-Axle Tire Friction Tester

Compared with the Trailer-Axle Tire Friction Tester, the modified rolling resistance machine has the following advantages:

- Environmental temperature is controlled. The rolling resistance machine is installed in our air-conditioned lab.
- Uniform road surface. On the rolling resistance machine, the road surface is material attached to the drum, whose profile is much more uniform than public roads.
- Repeatable testing. Test parameters, such as slip angle, velocity, are strictly controlled during a wear test on rolling resistance machine. On the Trailer-Axle Tire Friction Tester, since the test vehicles are running on public roads and must follow traffic regulations, vehicle speed is not constant, and lots of irregular accelerating, braking, turning, slipping will happen. These issues will significantly reduce the repeatability of the wear tests. However, since tire wear has a direct relationship with driving style and the final wear model should predict tire wear on the road, the future work for this project will include correlation of the sample wear data to road wear data.

However, there is one obvious issue of running tire wear tests on the modified rolling resistance machine. Curvature of the drum influences the shape of the contact patch, which is not the same as tire running on a road. Drum diameter of the MTS Tire Tread Wear Simulation System is 3 m, and they claim that the influence of surface curvature is minimized. On the rolling resistance machine, the drum diameter is 1.7 m. From the point of view of data processing, literature shows that rolling resistance on a drum is less than on a flat surface, and there are conversion factors to convert rolling resistance on drum to flat surface (Luchini, 1982). But there is no publication that provides conversion factors to convert wear rate on a drum to flat surface.

The other issue is that the modified rolling resistance machine cannot control the slip velocity of test tire, while slip velocity is a key parameter of rubber sample wear tests on the DFT.

In conclusion, with our currently available resources, the modified rolling resistance machine is an over-all better platform for tire wear tests. At the same time, there are differences between rubber sample wear tests on the DFT and tire wear tests on the rolling resistance machine, such as curvature of road surface and test parameters. These differences could cause problems when attempts are made to correlate rubber sample wear to tire wear. Additional modification on test rigs or data processing might be necessary.

4. Supervised Machine Learning

After collecting wear data, the next step is to use machine learning methods to develop the wear model. Therefore, it is necessary to understand the theory of machine learning, different machine learning methods and how to apply those methods in wear modeling. Machine learning explores the study and construction of algorithms that can learn from and make predictions on data (Kohavi & Provost, 1998). It allows computers to learn without being explicitly programmed.

Machine learning methods can be divided into three categories: supervised, unsupervised, and reinforcement learning.

- **Supervised learning.** Supervised learning is the machine learning task of inferring a function from labeled training data (Mohri, Rostamizadeh, & Talwalkar, 2012). The training data consists of multiple pairs of input and desired output. The result function of supervised learning, can be used for mapping new examples.
- **Unsupervised learning.** Unlike supervised learning, training data in unsupervised learning are unlabeled. In other words, there is no existing correct answers or degree of error.
- **Reinforcement learning.** Reinforcement learning concerns with how software agents take actions in an environment to maximized notion of cumulative reward (Jaksch, Ortner, & Auer, 2010).

In this research, wear data collected from test rigs contains clearly coupled inputs (testing parameters) and outputs (wear rate), thus a suitable machine learning method should be chosen from supervised learning methods. In this chapter, first, multiple models of supervised learning are introduced in details, followed by the criteria to evaluate model performance and their comparisons. In the end of this chapter, the feasibility of applying machine learning methods in rubber/tire wear modeling is validated using data from the DFT.

4.1 Additive Models and Trees

4.1.1 Generalized Additive Models

Traditional linear models often perform poorly in real life situations, where models are usually nonlinear. The solution is to introduce smooth functions into linear models, which results in generalized additive model (GAM). The form of a generalized additive model is

$$E(Y | X_1, \dots, X_p) = \alpha + f_1(X_1) + \dots + f_p(X_p) \quad (4.1)$$

X_1, X_2, \dots, X_p are predictors, Y is the outcome. f_i are smooth functions.

There is a simple iterative method called Backfitting algorithm to fit additive model, which is described below (Hastie, Tibshirani, & Friedman, 2001):

1. Initialize: $\alpha = \frac{1}{N} \sum_1^N y_i$, $f_j \equiv 0$, $\forall i, j$.
 $j = 1, 2, \dots, p, \dots, 1, 2, \dots, p, \dots$
2. Cycle: $f_j \leftarrow S_j \left\{ \left[y_i - \alpha - \sum_{k \neq j} f_k(x_{ik}) \right]_1^N \right\}$,
 $f_j \leftarrow f_j - \frac{1}{N} \sum_{i=1}^N f_j(x_{ij})$.

Until function f_j change less than a specified threshold.

4.1.2 Tree-based Methods

In tree-base methods, the feature space is divided into rectangles, then fit one simple model in each rectangle. One popular method, called Classification And Regression Tree (CART), was introduced by Breiman et al. (Breiman, Friedman, Stone, & Olshen, 1984).

Consider a regression problem with inputs X_1 , X_2 and continuous response Y . To simplify the problem, spaces are binary split. Firstly, the space is split into two regions, and using the mean of Y to model the response in both regions. Then one or both of the regions are split into two more regions. This process continues until a specified threshold is met.

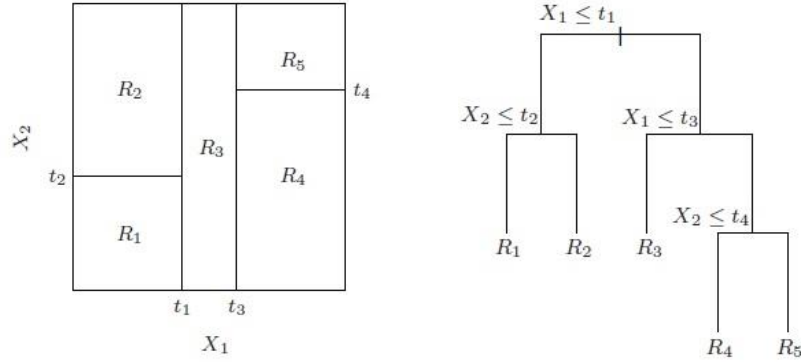


Figure 53. Partitions and CART (*Hastie, Tibshirani, & Friedman, 2001*)

For example, data consists of p inputs and a response, for each of N observations. If the data was partitioned into M regions R_1, R_2, \dots, R_M , the response can be modeled as:

$$f(x) = \sum_{m=1}^M c_m I(x \in R_m) \quad (4.2)$$

If least squares method is used, it is obvious that the best \hat{c}_m is:

$$\hat{c}_m = \text{ave}(y_i | x_i \in R_m) \quad (4.3)$$

Now the problem is to find the best binary partition. Begin from all of the data, define a split variable j , split point s , and the pair of half planes as:

$$R_1(j, s) = \{X | X_j \leq s\}, R_2(j, s) = \{X | X_j > s\} \quad (4.4)$$

Thus the problem converts into finding the j and s that solve:

$$\min_{j,s} [\min_{c_1} \sum_{x \in R_1} (y_i - c_1)^2 + \min_{c_2} \sum_{x \in R_2} (y_i - c_2)^2] \quad (4.5)$$

Inside each region,

$$\hat{c}_1 = \text{ave}(y_i | x_i \in R_1), \hat{c}_2 = \text{ave}(y_i | x_i \in R_2) \quad (4.6)$$

After finding the best split point, the data is partitioned into two regions. This process is repeated on all resulting regions. The tree will stop growing when some minimum node size is reached. Then this large tree T_0 will be pruned using cost-complexity pruning (Breiman, Friedman, Stone, & Olshen, 1984).

Subtree T is defined as any tree that can be obtained by pruning T_0 , $|T|$ is the number of terminal nodes in T , and

$$\begin{aligned} N_m &= \#\{x_i \in R_m\} \\ \hat{c}_m &= \frac{1}{N_m} \sum_{x_i \in R_m} y_i \\ Q_m(T) &= \frac{1}{N_m} \sum_{x_i \in R_m} (y_i - \hat{c}_m)^2 \end{aligned} \quad (4.7)$$

The cost complexity is

$$C_\alpha(T) = \sum_{m=1}^{|T|} N_m Q_m(T) + \alpha |T| \quad (4.8)$$

Now the problem becomes: for each α , find subtree $T_\alpha \subseteq T_0$ to minimize $C_\alpha(T)$. α is a tuning parameter, and $\alpha \geq 0$. For each α , the internal node that produces the smallest increase in $\sum_m N_m Q_m(T)$ will be collapsed successively. These procedures generate a sequence of subtrees, and the smallest subtree T_α is among them. The next step is calculating the cross-validation error for each α , and find α that minimize the cross-validation error. The final tree is T_α .

4.2 Boosting Methods

Boosting methods can be described as methods of combining multiple weak learners into one strong learner. Here “weak” means that the error rate of the learner is only slightly better than random guessing. There are many boosting algorithms, two typical boosting methods will be described.

4.2.1 AdaBoost

Schapire and Freund developed AdaBoost (Freund & Schapire, 1995), which might be the most popular boosting method. Consider a set of predictor variables X and output $Y \in \{\pm 1\}$. A weak classification algorithm is applied on repeatedly modified version of training data, which results in a sequence of weak classifiers

$G_m(x), m = 1, 2, \dots, M$. Predictions from all of these weak classifiers are combined into the final prediction:

$$G(x) = \text{sign}\left(\sum_{m=1}^M \alpha_m G_m(x)\right) \quad (4.9)$$

Where $\alpha_1, \alpha_2, \dots, \alpha_M$ are weights of $G_m(x)$, they provide higher weights to more accurate classifiers.

As mentioned previously, the training data is repeatedly modified. Each training observation $(x_i, y_i), i = 1, 2, \dots, N$ has a weight w_i . In the 1st iteration, all the weights are $\frac{1}{N}$. For all the rest iterations, w_i are individually modified. At each step, misclassified observations in the previous step will have their weights increased, and decreased weights for correctly classified observations. This algorithm is called AdaBoost.M1, its details are listed below (Hastie, Tibshirani, & Friedman, 2001):

1. Initialize the observation weights $w_i = 1/N, i = 1, \dots, N$.
2. For $m = 1$ to M :
 - a) Fit a classifier $G_m(x)$ to the training data using weight w_i .
 - b) Compute $err_m = \frac{\sum_{i=1}^N w_i I(y_i \neq G_m(x_i))}{\sum_{i=1}^N w_i}$
 - c) Compute $\alpha_m = \log\left(\frac{1 - err_m}{err_m}\right)$
 - d) Set $w_i \leftarrow w_i \cdot \exp[\alpha_m I(y_i \neq G_m(x_i))], i = 1, \dots, N$
3. Output $G(x) = \text{sign}\left(\sum_{m=1}^M \alpha_m G_m(x)\right)$

4.2.2 Boosting Trees

As discussed before, trees partition a space into regions $R_j, j = 1, \dots, J$. A constant γ_j is assigned to each region. As a result, a tree can be written as

$$T(x; \Theta) = \sum_{j=1}^J \gamma_j I(x \in R_j) \quad (4.10)$$

Where $\Theta = \{R_j, \gamma_j\}_1^J$. A Boosted tree model is the sum of such trees,

$$f_M(x) = \sum_{m=1}^M T(x; \Theta) \quad (4.11)$$

To fit the model, a method called Forward Stagewise Additive Modeling is used (Hastie, Tibshirani, & Friedman, 2001):

1. Initialize $f_0(x) = 0$.
2. For $m = 1$ to M :
 - a) Compute $\Theta_m = \arg \min_{\Theta_m} \sum_{i=1}^N L(y_i, f_{m-1}(x_i) + T(x; \Theta_m))$
 - b) Set $f_m(x) = f_{m-1}(x) + T(x; \Theta_m)$.

Where $\Theta_m = \{R_{jm}, \gamma_{jm}\}_1^{J_m}$, $L(y, f(x))$ is a loss function. In each region, if we have R_{jm} , the optimal γ_{jm} can be easily found from:

$$\hat{\gamma}_{jm} = \arg \min_{x_i \in R_{jm}} L(y_i, f_{m-1}(x_i) + \gamma_{jm}) \quad (4.12)$$

However, finding the regions is difficult. To solve this problem, numerical optimization methods come into play, and results in Gradient Tree Boosting. The algorithm is as shown below (Hastie, Tibshirani, & Friedman, 2001):

1. Initialize $f_0(x) = \arg \min_{\gamma} \sum_{i=1}^N L(y_i, \gamma)$
2. For $m = 1$ to M :
 - a) For $i = 1, 2, \dots, N$ compute: $r_{im} = -\left[\frac{\partial L(y_i, f(x_i))}{\partial f(x_i)}\right]_{f=f_{m-1}}$.
 - b) Fit a regression tree to the target r_{im} giving terminal regions $R_{jm}, j = 1, \dots, J_m$.
 - c) For $j = 1, \dots, J_m$, compute $\gamma_{jm} = \arg \min_{\gamma} \sum_{x_i \in R_{jm}} L(y_i, f_{m-1}(x_i) + \gamma)$.
 - d) Update $f_m(x) = f_{m-1}(x) + \sum_{j=1}^{J_m} \gamma_{jm} I(x \in R_{jm})$.
3. Output $f(x) = f_M(x)$.

4.3 Tree Bagging and Random Forest

Bagging is a method for generating multiple versions of a predictor and using these to get an aggregated predictor (Breiman L. , Bagging predictors, 1996). When applied in regression, the aggregated predictor is an average of those multiple versions, which are generated by making bootstrap replicates of the learning set. These multiple versions are also used to form new learning sets.

Bagging is usually applied to decision tree methods (Bootstrap aggregating, 2017), which results in Tree bagging. For inputs $X = x_1, x_2, \dots, x_n$ and response $Y = y_1, y_2, \dots, y_n$. Bagging repeat B times to select a random sample with replacement of the training set, and fit trees to these samples. The result model is an average of predictions of all individual trees:

$$f = \frac{1}{B} \sum_{b=1}^B f_b(x) \quad (4.13)$$

Random forests are a combination of tree predictors such that each tree depends on the values of a random vector sampled independently and with the same distribution for all trees (Breiman L. , Random forests, 2001). Each tree grows as:

1. If the number of cases in the training set is N , sample N cases at random - but with replacement, from the original data. This sample will be the training set for growing the tree.
2. If there are M input variables, a number $m \ll M$ is specified such that at each node, m variables are selected at random out of the M and the best split on these m is used to split the node. The value of m is held constant during the forest growing.
3. Each tree is grown to the largest extent possible. There is no pruning.

4.4 Neural Networks

With more than 70 years of history, neural networks are still highly competitive among all machine learning models. A neural network is a sorted triple (N, V, w) with two set N, V and a function w , where N is the set of neurons and V is a set

$\{(i, j) | i, j \in \mathbb{N}\}$ whose elements are called connections between neuron i and j . The function w defines the weights, where w_{ij} is the weight of the connection between neuron i and j (Kriesel, 2012).

4.4.1 Components of a Neural Network

Each neuron contains of these components: propagation function, activation function, and output function.

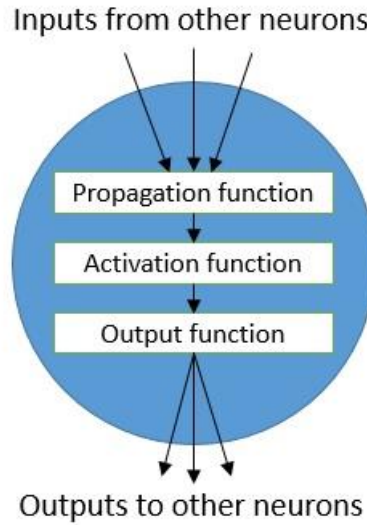


Figure 54. Data processing in a neuron

The propagation function computes the input $p_j(t)$ to neuron j from the outputs $o_i(t)$ of predecessor neurons, and has the form (Artificial neural network, 2017):

$$p_j(t) = \sum_i o_i(t) w_{ij} \quad (4.14)$$

Activation function determines the activation of a neuron dependent on network input and threshold value (Kriesel, 2012). For neuron j , its activation function σ satisfies:

$$a_j(t) = \sigma(p_j(t), a_j(t-1), \Theta_j) \quad (4.15)$$

Where $a_j(t)$ is the current activation state, Θ_j is threshold value. During a learning procedure, the value of Θ_j can be changed.

There are different activation functions. The simplest one is binary threshold function. When the input is larger than a threshold, function value changes from one to another, otherwise remains the same. Logistic function is another popular activation function, which has the form:

$$\frac{1}{1 + e^{-x}} \quad (4.16)$$

Logistic function maps from 0 to 1. If mapping range $(-1,1)$ is necessary, people can use hyperbolic tangent function.

For neuron j , its output function g satisfies:

$$o_j = g(a_j) \quad (4.17)$$

Where o_j is the output value. In most cases, g is the identity function, thus:

$$o_j = a_j \quad (4.18)$$

4.4.2 Fit a Neural Network

In the case of supervised learning, a training set consists of inputs and correct response. To fit a neural network to such data, assume that we use a feedforward neuron network with p inputs, one hidden layer with M neurons, and K responses. Then the problem is to calculate all the weights:

$$\begin{aligned} & \{\alpha_{0m}, \alpha_m; m = 1, 2, \dots, M\}, M(p+1) \text{ weights} \\ & \{\beta_{0k}, \alpha_k; k = 1, 2, \dots, K\}, K(M+1) \text{ weights} \end{aligned} \quad (4.19)$$

The error function will be:

$$R(\theta) = \sum_{k=1}^K \sum_{i=1}^N (y_{ik} - f_k(x_i))^2 \quad (4.20)$$

Where θ is the set of all weights. The generic approach to minimize $R(\theta)$ is by gradient descent, called back-propagation in this setting (Hastie, Tibshirani, & Friedman, 2001).

Let $z_{mi} = f_{act}(\alpha_{0m} + \alpha_m^T x_i)$, $z_i = (z_{1i}, z_{2i}, \dots, z_{Mi})$, then we have derivatives of $R(\theta)$

as:

$$\begin{aligned}\frac{\partial R_i}{\partial \beta_{km}} &= -2(y_{ik} - f_k(x_i))g'_k(\beta_k^T z_i)z_{mi} \\ \frac{\partial R_i}{\partial \alpha_{km}} &= -\sum_{k=1}^K 2(y_{ik} - f_k(x_i))g'_k(\beta_k^T z_i)\beta_{km}\sigma'(\alpha_m^T x_i)x_{il}\end{aligned}\tag{4.21}$$

Then the gradient descent update is:

$$\begin{aligned}\beta_{km}^{r+1} &= \beta_{km}^r - \gamma_r \sum_{i=1}^N \frac{\partial R_i}{\partial \beta_{km}^r} \\ \alpha_{ml}^{r+1} &= \alpha_{ml}^r - \gamma_r \sum_{i=1}^N \frac{\partial R_i}{\partial \alpha_{ml}^r}\end{aligned}\tag{4.22}$$

Where γ_r is learning rate, and usually its value is a constant.

Equation (4.21) can be written as:

$$\begin{aligned}\frac{\partial R_i}{\partial \beta_{km}} &= \delta_{ki}z_{mi} \\ \frac{\partial R_i}{\partial \alpha_{km}} &= s_{mi}x_{il}\end{aligned}\tag{4.23}$$

δ_{ki} are errors at the output layer, s_{mi} are errors at the hidden layer. These two types of errors satisfy:

$$s_{mi} = \sigma'(\alpha_m^T x_i) \sum_{k=1}^K \beta_{km} \delta_{ki}\tag{4.24}$$

At this point, updates in (4.22) can be calculated with a two-pass algorithm:

- Forward pass: current weights are fixed, and calculate the prediction $f_k(x_i)$.
- Backward pass: calculate δ_{ki} , then use (4.24) to calculate s_{mi} .

Implement the values of δ_{ki} and s_{mi} to (4.23), which updates (4.22). This procedure is called back-propagation.

4.4.3 Network Topology

The simplest neural network type is feedforward neural network, where connections are only permitted to neurons of the following layer (Kriesel, 2012).

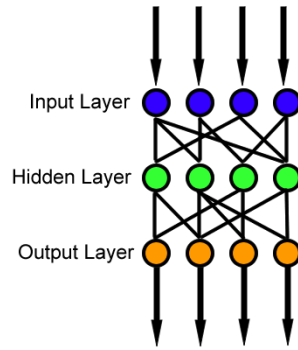


Figure 55. Feed forward neuron network (*Feedforward neural network, 2017*)

In some neural networks, neurons can influence themselves. They are called recurrent networks. Different types of recurrence are:

- Direct recurrence: neurons are connected to themselves.
- Indirect recurrence: connections are allowed towards the input layer.
- Lateral recurrence: connections are allowed between neurons in the same layer.
- Complete interconnection: every neuron can connect to every other neuron.

The order of neurons receiving and processing data is crucial, thus neuron networks can be divided into two types:

- Synchronous activation: all neurons of a network simultaneously calculate network inputs, activation and output, and pass them on (Kriesel, 2012).
- Asynchronous activation: neurons don't simultaneously change values, which can be further classified:
 - i. Random order: neurons are chosen and updated randomly.
 - ii. Random permutation: neurons are updated in a randomly chosen order, each neuron will be updated for only once.
 - iii. Topological order: neurons are updated in a fixed order

4.5 Support Vector Machines

In 1995, C. Cortes and V. Vapnik introduced Support Vector Machine (SVM) as a new learning machine for two-group classification problems (Cortes & Vapnik, 1995). Because of its general good performance, SVM has become popular since then.

4.5.1 Basic of SVM

Assume X is the input set, Y is the response set, and training sets are: $(x_1, y_1), \dots, (x_k, y_k)$, where $x \in R^n, y \in \{\pm 1\}$. Then there exists a hyperplane of the form

$$\vec{w}^T \vec{x} + b = 0 \quad (4.25)$$

Separate the training samples as

$$\begin{aligned} \vec{w}^T \vec{x}_i + b &\leq 0, \text{ for } y_i = -1 \\ \vec{w}^T \vec{x}_i + b &\geq 0, \text{ for } y_i = +1 \end{aligned} \quad (4.26)$$

Where \vec{w} is normal to the hyperplane, b is the perpendicular distance from the hyperplane to the origin.

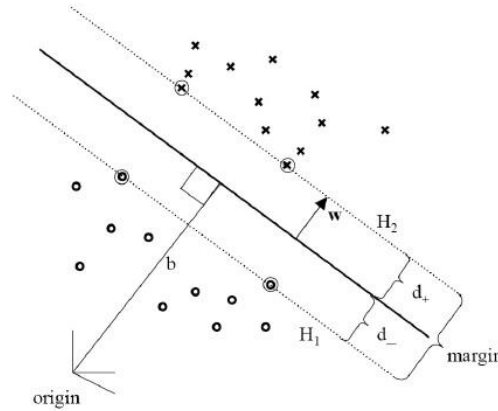


Figure 56. Optimal separating hyperplane with maximum margin (Hofmann, 2006)

It is obvious that there exists more than one separating hyperplane. To find the optimal separating hyperplane, let d_+ (d_-) be the shortest distance from a separating hyperplane to a positive (negative) training example, where $d_+ + d_-$ is called “margin”.

To maximize the margin, for all \vec{x}_i :

$$\vec{w}^T \vec{x}_i + b \geq +1, \text{ for } y_i = +1 \quad (4.27)$$

$$\vec{w}^T \vec{x}_i + b \leq -1, \text{ for } y_i = -1 \quad (4.28)$$

Combine these two equations:

$$y_i \left(\vec{w}^T x_i + b \right) \geq 1 \quad (4.29)$$

As a result, , the distance between every data point and the hyperplane is greater than 1 in

terms of the unit vector $\vec{w}_n = \frac{\vec{w}}{\|\vec{w}\|}$, $b_n = \frac{|b|}{\|\vec{w}\|}$.

For all data points that meet the equality in (4.27), they lie on the hyperplane

$\vec{w}^T x_i + b = 1$. For all data points that meet the equality in (4.28), they lie on hyperplane

$\vec{w}^T x_i + b = -1$. Thus, the margin length is $\frac{2}{\|\vec{w}\|}$. As a result, finding the optimal separating

hyperplane is equivalent to maximizing margin $\frac{2}{\|\vec{w}\|}$ subject to (4.29).

4.5.2 Constructing the Optimal Hyperplane

The problem posed at the end of last section, is equal to minimizing

$\Phi(\vec{w}) = \frac{1}{2} \vec{w}^T \vec{w}$ subject to (4.29). To solve this, we construct a Lagrangian:

$$L_p(\vec{w}, b, \vec{\alpha}) = \frac{1}{2} \vec{w}^T \vec{w} - \sum_{i=1}^l \alpha_i \left[y_i \left(\vec{w}^T x_i + b \right) - 1 \right] \quad (4.30)$$

Where $\vec{\alpha} = (\alpha_1, \alpha_2, \dots, \alpha_l)$ is a vector of non-negative Lagrange multipliers corresponding

to (4.29). To optimize L_p , based on the Duality Theorem (Haykin, 1998), if the primal

problem (minimize with respect to \vec{w} and b) has an optimal solution, the dual problem

(maximize with respect to $\vec{\alpha}$) also has an optimal solution, and the corresponding

optimal values are equal.

To solve the primal problem, differentiate L_p with respect to \vec{w} and b , and set

the results to zero:

$$\frac{\partial L}{\partial \vec{w}} = \left(\vec{w} - \sum_{i=1}^l \alpha_i y_i \vec{x}_i \right) = 0 \quad (4.31)$$

$$\frac{\partial L}{\partial b} = \sum_{i=1}^l \alpha_i y_i = 0 \quad (4.32)$$

Substitute (4.31) and (4.32) into (4.30), we obtain the dual problem:

$$L_D(\vec{\alpha}) = \sum_{i=1}^l \alpha_i - \frac{1}{2} \sum_{i=1}^l \sum_{j=1}^l \alpha_i \alpha_j y_i y_j \vec{x}_i \vec{x}_j \quad (4.33)$$

L_D has to be maximized subject to:

$$\begin{aligned} \sum_{i=1}^l \alpha_i y_i &= 0 \\ \alpha_i &\geq 0, \text{ for } i = 1, \dots, l \end{aligned} \quad (4.34)$$

Finding α_i that maximize L_D can be solved by numerical methods of quadratic optimization. In the solution, training points for which $\alpha_{i,o} > 0$ are called “support vectors” and lie on the hyperplanes. With the optimum Lagrange multiplier $\alpha_{i,o}$, the optimal weight vector \vec{w}_o is:

$$\vec{w}_o = \sum_{i=1}^l \alpha_{i,o} y_i \vec{x}_i \quad (4.35)$$

And the optimal separating hyperplane is:

$$\vec{w}_o^T \vec{x} + b_o = \sum_{i=1}^l \alpha_{i,o} y_i \vec{x}_i^T \vec{x} + b_o = 0 \quad (4.36)$$

The optimal perpendicular distance b_o is:

$$b_o = 1 - \vec{w}_o^T \vec{x}_+ \quad (4.37)$$

Where \vec{x}_+ is a positive support vector.

4.5.3 Kernel Trick

In the previous section, the data set is linear separable, which is very rare in real world situations. To deal with nonlinear problems, the kernel functions were introduced, which map the input space into a linear separable space.

Consider a mapping function Φ from 2-D space to 3-D space:

$$\Phi(\vec{x}) = \left(x_1^2, \sqrt{2}x_1x_2, x_2^2 \right)^T \quad (4.38)$$

Substitute (4.38) into (4.25):

$$\vec{w}^T(\vec{x}) = w_1x_1^2 + w_2\sqrt{2}x_1x_2 + w_3x_2^2 = 0 \quad (4.39)$$

This means that, with an appropriate mapping function, a linear separable classifier can be easily transformed into a nonlinear classifier.

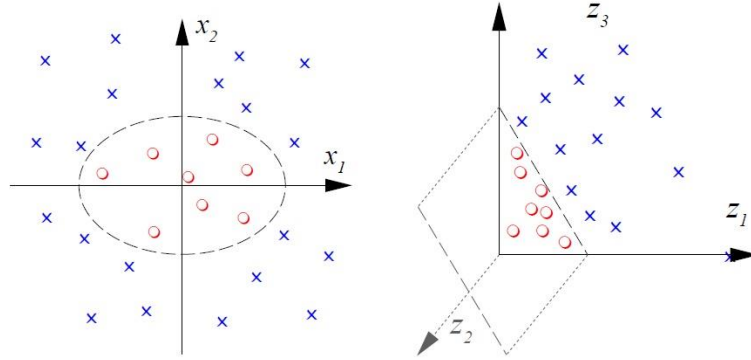


Figure 57. Mapping from 2-D space to 3-D space (Weston, 2006)

By applying the linear classifier to a mapped data set, the dual problem in the Lagrangian can be written as:

$$L_D(\vec{\alpha}) = \sum_{i=1}^l \alpha_i - \frac{1}{2} \sum_{i=1}^l \sum_{j=1}^l \alpha_i \alpha_j y_i y_j \Phi(\vec{x}_i)^T \Phi(\vec{x}_j) \quad (4.40)$$

The optimal weight vector and optimal separating hyperplane becomes:

$$\vec{w}_O = \sum_{i=1}^l \alpha_{i,O} y_i \Phi(\vec{x}_i) \quad (4.41)$$

$$\vec{w}_O^T \vec{x} + b_O = \sum_{i=1}^l \alpha_{i,O} y_i \Phi(\vec{x}_i)^T \Phi(\vec{x}) + b_O = 0 \quad (4.42)$$

It is obvious that, if we define a kernel function $K(\vec{x}_i, \vec{x}) = \Phi(\vec{x}_i)^T \Phi(\vec{x})$, the classifier will only depend on the mapped data. Nonlinear 2-D space data and the mapping function become unnecessary.

Some kernel functions are suitable for most situations, such as:

- Polynomial kernel: $K(x, x') = (x^T x' + \theta)^d$ (Weston, 2006)

- Radial basis function (RBF, or Gaussian) kernel:

$$K(x, x') = \exp\left(-\frac{\|x - x'\|^2}{2\sigma^2}\right) \quad (\text{Vert, Tsuda, \& Schölkopf, 2004})$$

- Sigmoid kernel: $K(x, x') = \tanh(\eta x x' + \theta)$

θ, d, σ, η are specified by user. There is no general best choice of kernel function. But usually, a low polynomial kernel or an RBF kernel is good for the initial try (Joachims, 1998).

4.5.4 Least Squares Support Vector Machine

J.A.K. Suykens and J. Vandewalle proposed a least squares version for SVM (Suykens & Vandewalle, 1999). Instead of a convex quadratic programming problem in classical SVM, least squares SVM (LS-SVM) solves a set of linear equations.

In LS-SVM, a classification problem is written as:

$$\min_{w,b,e} l(w,b,e) = \frac{1}{2} w^T w + \gamma \frac{1}{2} \sum_{k=1}^N e_k^2 \quad (4.43)$$

Which is subject to:

$$y_k [w^T \varphi(x_k) + b] = 1 - e_k, k = 1, \dots, N \quad (4.44)$$

Then construct the Lagrangian,

$$L(w,b,e;\alpha) = l(w,b,e) - \sum_{k=1}^N \alpha_k \{ y_k [w^T \varphi(x_k) + b] - 1 + e_k \} \quad (4.45)$$

Differentiate the Lagrange function with respect to w, b, e, α_k , the result is:

$$\begin{aligned} w &= \sum_{k=1}^N \alpha_k y_k \varphi(x_k) \\ \sum_{k=1}^n \alpha_k y_k &= 0 \\ \alpha_k &= \gamma e_k \\ y_k [w^T \varphi(x_k) + b] - 1 + e_k &= 0 \end{aligned} \quad (4.46)$$

(4.46) can be written as:

$$\begin{bmatrix} I & 0 & 0 & -Z^T \\ 0 & 0 & 0 & -Y^T \\ 0 & 0 & \gamma I & -I \\ Z & Y & I & 0 \end{bmatrix} \begin{bmatrix} w \\ b \\ e \\ \alpha \end{bmatrix} = \begin{bmatrix} 0 \\ 0 \\ 0 \\ \bar{1} \end{bmatrix} \quad (4.47)$$

Where

$$\begin{aligned}
Z &= [\varphi(x_1)^T y_1, \dots, \varphi(x_N)^T y_N]^T \\
Y &= [y_1, \dots, y_N]^T \\
\vec{1} &= [1, \dots, 1]^T \\
e &= [e_1, \dots, e_N]^T \\
\alpha &= [\alpha_1, \dots, \alpha_N]^T
\end{aligned} \tag{4.48}$$

The solution of (4.47) is also given by

$$\begin{bmatrix} 0 & -Y^T \\ Y & ZZ^T + Y^{-1}I \end{bmatrix} \begin{bmatrix} b \\ \alpha \end{bmatrix} = \begin{bmatrix} 0 \\ \vec{1} \end{bmatrix} \tag{4.49}$$

As a result, fitting a LS-SVM can be done by solving (4.49).

4.5.5 Applications of SVM in Wear Prediction

D. Shi and N. Gindy combined LS-SVM and principal component analysis technique to predict tool wear during machining process (Shi & Gindy, 2007).

All experiments were done on a Cincinnati vertical broaching machine with high-speed steel broaching tool comprised of 15 teeth. Cutting force signals in Y and Z direction are inputs of LS-SVM model, length of flank wear (VB) is the output. Force signals were collected via strain sensors, VB was measured by optical scan microscope.

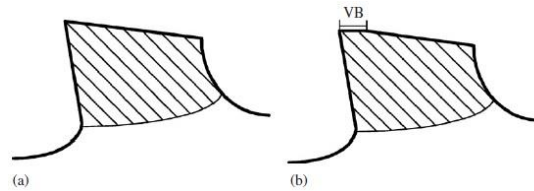


Figure 58. Definition of flank wear of broaching tool: (a) fresh tool, (b) worn tool (Shi & Gindy, 2007)

The data sets were divided into training sets and validation sets. The SVM tool wear model was trained by training sets, and then validated using validation sets. A good agreement can be found at each level of tool wear, which proves that SVM-based wear model is effective to predict tool wear.

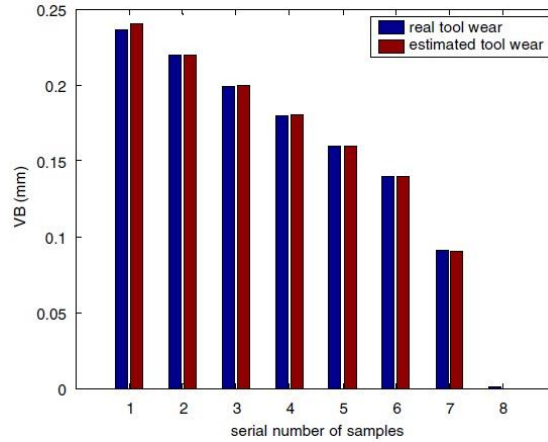


Figure 59. Comparison between predicted wear and wear measured by microscope (*Shi & Gindy, 2007*)

R. Slavkovic, et. al used SVM and improved SVM to predict casted floating ball wear rate (Slavkovic, Jugovic, Dragicevic, Jovicic, & Slavkovic, 2013). The experiments were carried out in a mill of optimum volumetric filling of 15.2 dm³ with 60 mm diameter balls. During the experiments, the mass of new balls was 8.5 kg, the initial mass of copper ore was 2.5 kg. For every 12 minutes, additional copper ore with the same mass was added. In the end, 60 experimental results were collected.

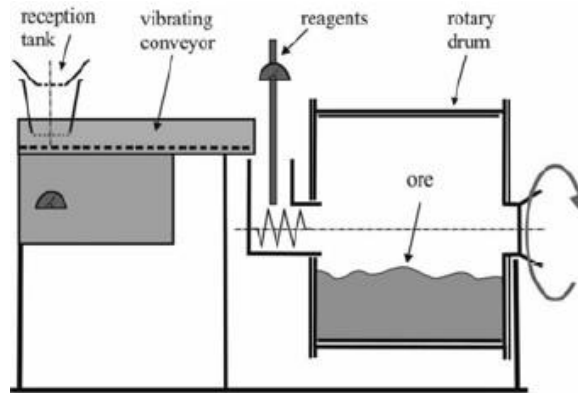


Figure 60. Experimental milling process (*Slavkovic, Jugovic, Dragicevic, Jovicic, & Slavkovic, 2013*)

The input vector consists of hardness (HRC) and the percentage of Cr, Mn, C, and Si, the output is abrasive wear rate.

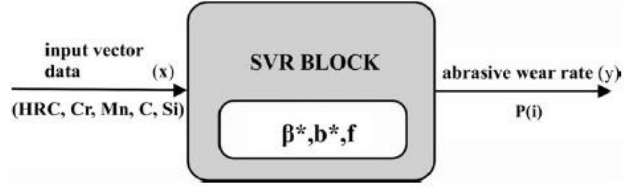


Figure 61. SVR implementation (Slavkovic, Jugovic, Dragicevic, Jovicic, & Slavkovic, 2013)

In the SVM model, three different kernel functions: radial basis kernel function (RBF), exponential radial basis kernel function (ERBF) and polynomial kernel function (POLY), were used. They also used their version of kernel functions:

$$k_{mix} = \rho k_{poly} + (1-\rho)k_{rbf}, k_{mix} = \rho k_{poly} + (1-\rho)k_{erbf} \quad (4.50)$$

Where ρ is a 0 to 1 scalar value.

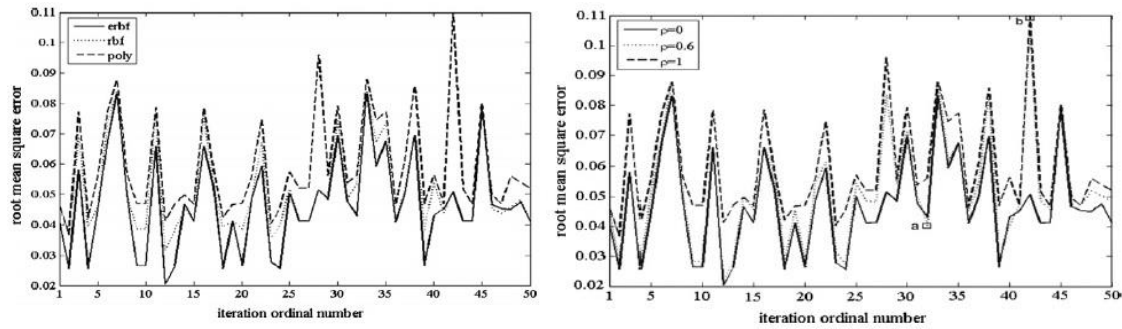


Figure 62. RMS values of different kernel functions (Slavkovic, Jugovic, Dragicevic, Jovicic, & Slavkovic, 2013)

Based on the performance of SVM models with different kernel function, they concluded that the combination of ERBF and POLY with $\rho = 0.6$ show better results for the practical purpose.

4.6 Comparison of Machine Learning Methods

After understanding the theory and developing several supervised learning models, the next step is to choose the best one for tire wear modeling. Therefore, to compare different models, it is necessary to put together a comparison metrics.

4.6.1 Coefficient of Determination

The coefficient of determination R^2 , is the proportion of the variance in the dependent variable that is predictable from the independent variables (Statistics and Probability Dictionary, 2017).

Assume a dataset has response (y_1, \dots, y_n) and predicted response (f_1, \dots, f_n) .

Define residuals as $e_i = y_i - f_i$, and the mean of response as $\bar{y} = \frac{1}{n} \sum_{i=1}^n y_i$. Then we have:

- Total sum of squares

$$SS_{tot} = \sum_i (y_i - \bar{y})^2 \quad (4.51)$$

- Regression sum of squares

$$SS_{reg} = \sum_i (f_i - \bar{y})^2 \quad (4.52)$$

- Sum of squares of residuals

$$SS_{res} = \sum_i e_i^2 = \sum_i (y_i - f_i)^2 \quad (4.53)$$

And the coefficient of determination is:

$$R^2 = 1 - \frac{SS_{res}}{SS_{tot}} = \frac{SS_{reg}}{SS_{tot}} \quad (4.54)$$

In regression, R^2 is an indication of how well the regression fits data points. The value of R^2 is 0 to 1. A value closer to 1 means better fits, $R^2 = 1$ means perfect fit.

4.6.2 Prediction Error

In a data-rich situation, the dataset is randomly divided into three parts: a training set, a validation set, and a test set (Hastie, Tibshirani, & Friedman, 2001). There is no general rule of the exact percentage of each set. Usually, training set is 50% to 80% of the data, and the rest is evenly divided for validation and test set.



Figure 63. Dataset division

- Training set: used to fit the model;
- Validation set: used to estimate prediction error;

- Test set: used to assess test error.

Assume that in the dataset, inputs is X , response is Y , prediction model $f(X)$ is fitted to the training set T . Then the lost function from measuring squared error is:

$$L(Y, f(X)) = (Y - f(X))^2 \quad (4.55)$$

Test error is the perdition error over an independent sample:

$$Err_T = E[L(Y, f(X)) | T] \quad (4.56)$$

X and Y are drawn randomly, and the training set T is fixed. Prediction error is defined as:

$$Err = E[L(Y, f(X))] = E[Err_T] \quad (4.57)$$

In reality, due to the size of dataset, various methods were proposed for estimating prediction error. The square root of the prediction error is called Root-mean-square error (RMSE), which is widely used as a criterion for model performance.

4.6.3 Cross-validation

Cross-validation is one of the most widely used method for estimating prediction error. One of the main reasons of using cross-validation is that there is not enough data to partition into training and test sets. In a K -fold cross-validation, the dataset is roughly divided into K equal-sized parts. One part is used for testing, the other part are used to fit the model.

Define $\kappa: \{1, \dots, N\} \mapsto \{1, \dots, K\}$ as an indexing function. $f^{-k}(x)$ is a prediction model that fitted to dataset with the k th part removed. Then the prediction error is:

$$CV(f) = \frac{1}{N} \sum_{i=1}^N L(y_i, f^{-\kappa(i)}(x_i)) \quad (4.58)$$

If a tuning parameter α is introduced into $f^{-k}(x, \alpha)$, which means that the α th model is fitted to dataset with the k th part removed. Then the prediction error becomes:

$$CV(f, \alpha) = \frac{1}{N} \sum_{i=1}^N L(y_i, f^{-\kappa(i)}(x_i, \alpha)) \quad (4.59)$$

$CV(f, \alpha)$ is a function that estimates test error, and there exist an optimal α that minimize it. As a result, the final model is $f(x, \alpha)$.

The most common choice of K is 5 or 10.

4.6.4 General Comparison of Supervised Machine Learning Models

There is no general answer to the question: which model is the best supervised learning model? The performance of different models are highly depend on data: e.g. number of inputs and response, data distribution, and size of dataset. But from literature reviews, we can still summarize a general comparison of supervised machine learning models in an application of regression.

Table 4. Comparison of supervised machine learning models

| Model | Pros | Cons |
|-----------------------|--|--|
| Boosting trees | 1. Usually has the best performance. | 1. Very easy to overfit. 2. Hard to tune parameters. 3. Training generally takes longer time. 4. Hard to interpret. |
| Bagged trees | 1. Can easily handle categorical features. | 1. Hard to interpret. |
| Random forest | 1. Less overfit. 2. Training takes less time than boosting trees. | 1. Hard to interpret. 2. Less accurate than boosting trees. |
| Neural network | 1. Robust. 2. Non-parametric, and easy to use. 3. Can handle highly nonlinear systems. | 1. Require a large diversity of training sets. 2. Large consumption of computational space and time. 3. Hard to interpret. |
| SVM | 1. Performs well with nonlinear systems. | 1. Hard to choose the best kernel function. |

| | | |
|--|--|---|
| | 2. Can handle high dimensional dataset well. 3. Easy to access. | 2. High algorithmic complexity and memory requirements. |
|--|--|---|

With a good understanding of pros and cons of different supervised learning models, and a clear view of training data characteristics, we can predict the performance of different models. However, actual model training using collected data is still necessary before making a conclusion of the best performing model.

4.7 Dimension Reduction

In machine learning, dimension reduction is the process of obtaining a group of principal variables from a larger group of variables. Dimension reduction are conducted for three major reasons:

- Simplification of models for easier interpretation (James, Witten, Hastie, & Tibshirani, 2013).
- Reduce training costs.
- Reduce overfitting.

There are two major types of dimension reduction: feature selection and feature extraction.

4.7.1 Feature Selection

Feature selection is the process of selecting a subset of features. A feature selection algorithm requires two parts: a search strategy, and an objective function.

The simplest search strategy, is to test all possible subset of features. Objective function evaluates the subsets and figure out the optimal subset. There are three main types of objective functions: wrapper, filter and embedded methods (Guyon & Elisseeff, 2003).

1. Wrapper methods train a new model for each subset, the model with best accuracy indicates the best subset.
2. Filter methods evaluate subsets by their features, such as inter/intra class distance and statistical dependence.

3. Embedded methods conduct feature selection as a part of model construction.

Among the above types of methods, wrapper is more popular, mainly because each subset is used for model training, which generally results in more accurate choice of optimal subset.

4.7.2 Feature Extraction

Feature extraction derives a new set of features from the original set, and the new set is capable of accurately and completely describe the original set. Different feature extraction algorithms have been proposed, such as:

- Principal component analysis (PCA) (Jolliffe, 2011)
- Multifactor dimensionality reduction (MDR) (Ritchie, et al., 2001).
- Independent component analysis (ICA) (Comon, 1994).

As a popular feature extraction algorithm, PCA is used as an example of how feature extraction works. Assume that $x \in \mathbb{R}^N$ can be represented as a linear summation of orthonormal vectors:

$$x = \sum_{i=1}^N y_i \varphi_i \text{ where } \varphi_i^T \varphi_j = \begin{cases} 0; i \neq j \\ 1; i = j \end{cases} \quad (4.60)$$

To represent x with M ($M < N$) independent vectors, coefficients y_{M+1}, \dots, y_N are replaced by constants b_i . The new expression of x is:

$$\hat{x}(M) = \sum_{i=1}^M y_i \varphi_i + \sum_{i=M+1}^N b_i \varphi_i \quad (4.61)$$

Now the problem becomes finding φ_i and b_i that minimize the mean-square error of x and $\hat{x}(M)$: $MSE = \sum_{i=M+1}^N E[(y_i - b_i)^2]$.

Calculating the partial derivative of the equation above, gives us the value of b_i :

$$b_i = E[y_i] \quad (4.62)$$

To find φ_i , Substitute (4.62) into the MSE equation and introduce a set of Lagrange multipliers λ_i , the optimization problem becomes:

$$MSE = \sum_{i=M+1}^N \varphi_i^T \Sigma_x \varphi_i + \sum_{i=M+1}^N \lambda_i (1 - \varphi_i^T \varphi_i) \quad (4.63)$$

Calculate the partial derivative of equation above, we get: $\Sigma_x \varphi_i = \lambda_i \varphi_i$. Therefore, φ_i and λ_i are the eigenvectors and eigenvalues of Σ_x . Substitute this back into (4.63), λ_i have to the smallest eigenvalues to minimize error.

In short, PCA calculates the optimal approximation of a random vector $x \in \mathbb{R}^N$ by a linear combination of M ($M < N$) independent vectors, by projecting x onto the eigenvectors φ_i corresponding to the largest eigenvalues λ_i of the covariance matrix Σ_x (Gutierrez-Osuna, 2011).

Obviously, feature extraction is a more generalized method than feature selection: the latter involves algorithms for search strategy and objective function. In some situations, feature selection is necessary. For example:

- Features are difficult to acquire. In this case, we can conduct feature selection of a large number of features, and select part of them for final application.
- Features have certain meanings. Feature extraction project original features onto a low-dimensional space, which result in loss of feature meanings, such as force, velocity, etc.

Feature selection is applied in section 5.3.2.

4.8 Choices of Inputs and Response for Rubber Sample Wear Model

In the case of rubber sample wear tests on the DFT. Data collected during a set of wear tests, can be split into three categories as Table 5.

Table 5. Data categorization of wear tests on DFT

| Category | Data description | Symbol |
|----------|---|------------------|
| Constant | Room temperature | T_r |
| | Distance from disk center to contact patch center | L_{DC} |
| | Gear ratio of servomotors | n_{dm}, n_{sm} |

| | | |
|------------------------------|--|------------------|
| Independent variables | Rubber property: visco-elastic modulus | E |
| | Rubber property: tensile strength | T_S |
| | Fracture dimension of road surface | D_f |
| | RPM of servomotors | N_{dm}, N_{sm} |
| Dependent variables | Normal load on rubber sample | F_N |
| | Longitudinal friction | F_f |
| | Temperature at contact patch | T_f |
| | Effective radius of rubber sample | R_C |
| | Sliding velocity | v_s |
| | Weight of rubber sample | m_S |
| | Diameter of rubber sample | D_S |

Based on literature reviews on factors influencing rubber abrasion and tire wear, initial choices of wear model inputs are listed in Table 6.

Table 6. Inputs of rubber sample wear model (early stage)

| Description | Symbol |
|--|---------------|
| Rubber property: visco-elastic modulus | E |
| Rubber property: tensile strength | T_S |
| Normal load on rubber sample | F_N |
| Longitudinal friction | F_f |
| Temperature at contact patch | T_f |
| Wavelength of road surface roughness | D_f |

The response could be:

- Weight loss per minute dm_t
- Weight loss per travelling distance dm_{tr}
- Weight loss per sliding distance or dm_{sl}

Finally, training process of rubber sample wear model can be illustrated as follows:

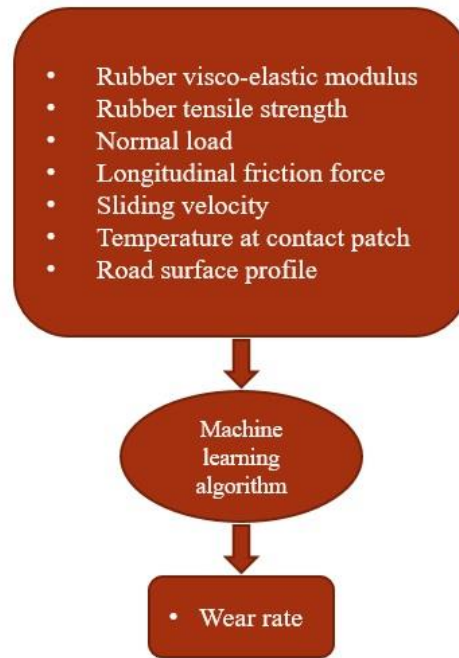


Figure 64. Training process of rubber sample wear model

4.9 Validation of the Wear Modeling Method

After validations of the performance of DFT, early trustable rubber sample wear data set was collected. The data set has its limitations: its size was not large enough, and not all inputs were included. But with some alteration, the data set can be used to train a friction model, which serves as a prior step before wear modeling.

To train a friction model with the wear data, longitudinal friction was removed from model inputs, and model response was changed to friction coefficient. Adding this prior step of friction modeling has several advantages:

- Friction is one of the dominating factors of wear. Success in friction modeling is a necessity of wear modeling.
- Inputs of friction modeling is relatively simple, and are mostly included in wear test dataset.
- Although some models are powerful, like neural networks, they perform badly when dataset is not large enough. Training a neural network model

using a small dataset can result in a bad performing model. For friction modeling, data of one test run can be divided into multiple segments, thus significantly increasing the size of training set.

Test configuration of the initial wear test data is listed in Table 7.

Table 7. Conditions of early wear test data

| Test configuration | Number of variations | Details |
|--------------------------------|----------------------|----------------------------------|
| Rubber compound | 1 | Compound A |
| Disk surface | 1 | Sandpaper P120 |
| Nominal contact patch pressure | 5 | 0.2, 0.33, 0.4, 0.5, 0.6 MPa |
| Sliding velocities | 5 | 0.01, 0.03, 0.05, 0.075, 0.1 m/s |
| Variations in total | 25 | |

Data of each test run was divided into eight segments. As a result, size of dataset (i.e. number of training samples) increased from 25 to 200, which is enough for models that required large dataset. Figure 65 illustrated the training process of friction model.

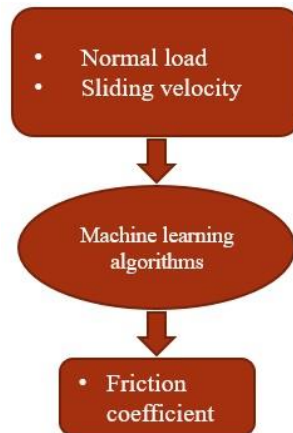


Figure 65. Process of training friction model trained by early wear data

When using machine learning methods, it is better to start from basic and simple algorithms. This manner can reduce the abuse of complicated methods. To start with, a basic algorithm -- linear regression was used, and the result is as follows:

- RMSE: 0.12
- R^2 : 0.05

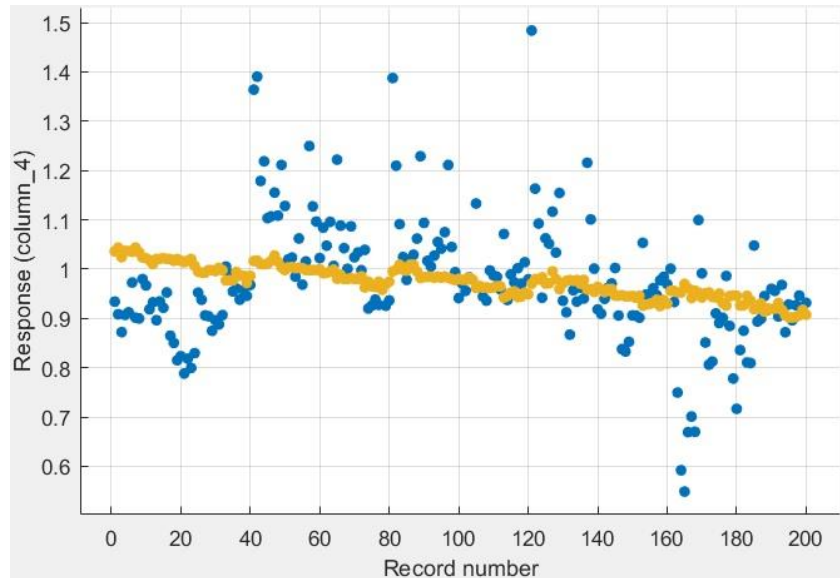


Figure 66. Response plot of linear regression based friction modeling. Blue dots: true response, orange dots: predicted response

Based on the performance of linear regression model, it is clear that although the RMSE value is not large, the R^2 is so close to zero, which means that the data fit is not acceptable.

The next step is to use more complex machine learning algorithms to train the friction model. Since this is a prior step of wear modeling, a relatively simple 2-layer feedforward neural network was chosen. This neural network model has one hidden layer of N (N is a tuning parameter) sigmoid neurons and the output layer has one linear neuron. The network was trained with Levenberg-Marquardt backpropagation algorithm (Kelley, 1999), which is popular in solving nonlinear problems.

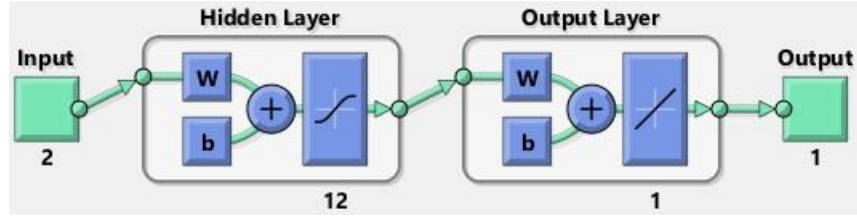


Figure 67. Structure of the 2-layer feedforward neural network

Training with the early wear data, a good-performing neural network model has 12 hidden neurons, and its performance is as follows:

- RMSE: 0.07
- R^2 : 0.78

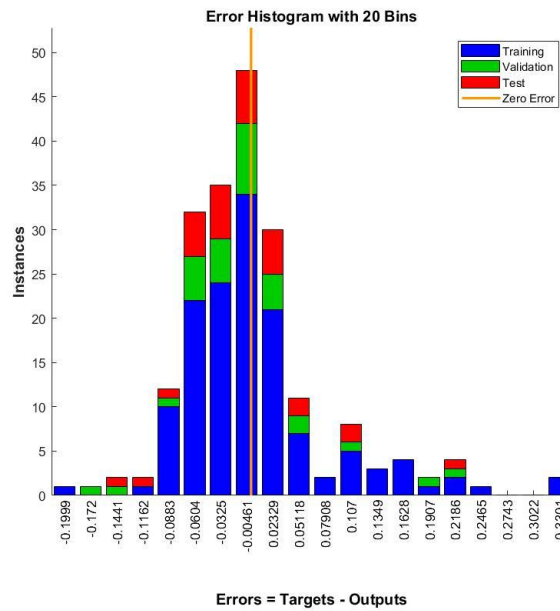


Figure 68. Error histogram of ANN based friction model trained by early data

It is clear that neural network based friction model is far better than linear model in terms of RMSE and R^2 . It should be noticed that the value of R^2 is only acceptable, not great. The reason could be the limited dimension of inputs: only normal load and sliding velocity were included. If flash temperature can be included, the resulting model could perform better. In conclusion, even under the situation of insufficient inputs, machine learning based friction modeling still proved its capability, and gave us confidence in using machine learning methods to predict rubber sample wear rate.

4.10 Choosing Machine Learning Algorithms for Wear Modeling

From the previous sections, we can learn that, a good machine learning based wear model, will need moderate dimension of inputs and a large enough dataset. Also, the model will be highly nonlinear. Based on this, candidate machine learning models were chosen, including:

- Boosted trees
- Bagged trees
- Linear SVM
- Quadratic SVM
- Cubic SVM
- Gaussian SVM
- 2-layer feedforward neural network

Boosted trees and bagged trees are fast and good-performing models. The biggest concern on these two methods is the dimension of inputs might be too high for them. Although we already know that linear SVM won't perform well, it stayed in the list as a "bottom line" of performance of support vector machine methods. As mentioned in section 2.3.5.2, the difference of quadratic SVM, cubic SVM, and Gaussian SVM is the kernel function: quadratic SVM use a quadratic kernel function:

$$K(x, x') = (x^T x' + \theta)^2 \quad (4.64)$$

Cubic SVM use a cubic kernel function

$$K(x, x') = (x^T x' + \theta)^3 \quad (4.65)$$

And Gaussian SVM use a Gaussian kernel function:

$$K(x, x') = \exp\left(-\frac{\|x - x'\|^2}{2\sigma^2}\right) \quad (4.66)$$

The choice of kernel function and tuning parameters θ, σ will decide how well the dataset is mapped to a linear separable space, thus influence the performance of SVM. 2-layer feedforward neural network is also selected because of its good performance when dealing with high dimensional and large dataset.

As mentioned in section 4.6.4, there is no answer to “which machine learning model is the best” before using them under specific situations. When the wear test data set is big enough and majority of inputs included, these chosen algorithms will be used to train wear models. After that, their performance will be compared to reveal the best machine learning models. The results are in section 5.2.4.

5. Results

In this chapter, results of this research are presented. At first, performance of the DFT is evaluated to prove that wear data collected from the DFT is trustable. After that, rubber sample wear test data are collected from the DFT. The wear data are used to train the initial rubber sample wear models using the selected machine learning methods from section 4.9. Performance of these wear models are compared and the machine learning methods that generates better wear models are selected. To further improve the accuracy and reduce over-fitting of the rubber sample wear model, rubber oxidation is introduced as an input, and dimension reduction was conducted. With wear data under 600 different test conditions, the complete rubber sample wear model is trained using neural network and SVM methods. Finally, tire wear tests are conducted on tires with known tread compound properties, test conditions are converted into the format of rubber sample wear model inputs, the result wear prediction is compared with actual tire wear.

5.1 DFT Performance Evaluation

Unlike the test machines available in the market, the DFT is designed and built in house, thus its performance has to be carefully evaluated before collecting wear test data for model training. Based on the design requirements, the following aspects need evaluation:

- Sensor data. After the load cells and temperature sensor were installed, it is necessary to evaluate their performance under known conditions.
- Sliding velocity control. Sliding velocity is a crucial input in the wear model. Therefore, the capability of controlling sliding velocity must be evaluated.
- Fluctuation of normal load. During wear tests, stability of normal load is important because it will influence other test parameters. For example, fluctuating normal load will results in fluctuating contact patch area, which causes unstable contact patch pressure and unrealistic wear results.

- Repeatability. As one of the most emphasized aspects in the design, wear tests conducted under the same test configurations must result in the same output, e.g. sample weight loss.

Evaluation of these aspects are presented in the following sections.

5.1.1 Evaluation of Sensor Data

For evaluating load cells, they were installed between the die spring and rubber sample. The die spring was compressed with 0.5 mm increments. Since the spring rate is known, load can be calculated and compared with load cell measurements. The results are shown in Table 8 and Figure 69.

Table 8. Calculated load and sensor measurements

| dx/mm | F/lb | Fn/lb | Error of Fn | Ff/lb | Error of Ff |
|--------------|-------------|--------------|--------------------|--------------|--------------------|
| 0 | 0 | 0 | - | 0 | - |
| 3 | 8.07 | 8.83 | 9.41% | 8.73 | 8.18% |
| 8 | 21.52 | 22.82 | 5.70% | 22.85 | 6.18% |
| 13 | 34.97 | 36.56 | 4.55% | 36.92 | 5.58% |

dx is spring compression, F is calculated load, Fn is measurement of normal load using the load cell, Ff is measurement of friction force using the load cell.

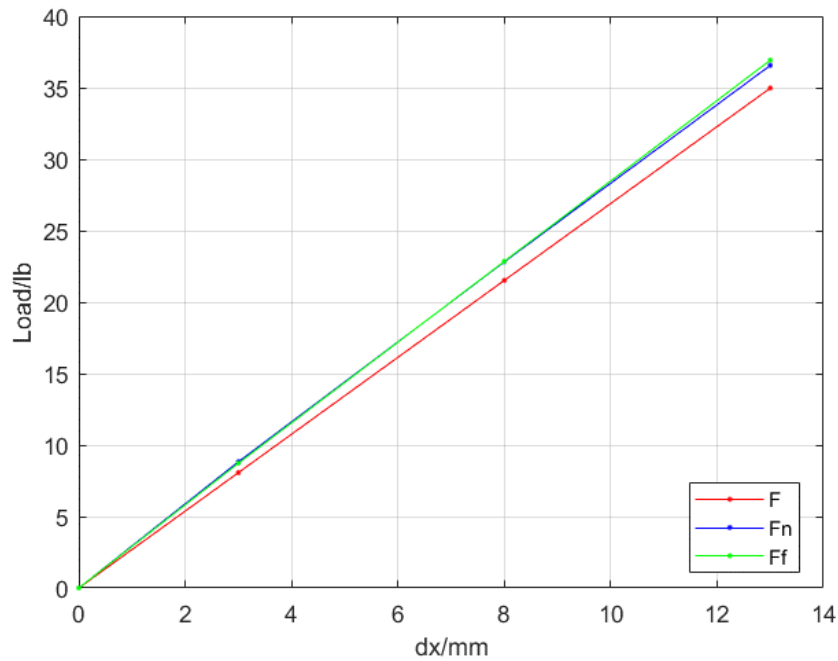


Figure 69. Plot of calculated loads and measurements

According to Table 8, all errors are less than 10%, which is acceptable. The main reason of the error could be measurement error of spring compression length.

For evaluating the temperature sensor, we used two objects that have steady temperature: rubber sample that had been left in room temperature for 20 hours, and center of my hand. The OS136-1-MVC temperature was kept 1 cm away from the object to be measured, which is the same distance as temperature sensor to sample during actual wear tests. Readings from a traditional digital thermometer act as the reference. The result is shown in Table 9.

Table 9. Temperature measurements

| | Reference/ $^{\circ}$ C | OS136-1-MVC/ $^{\circ}$ C | Error |
|--------|-------------------------|---------------------------|-------|
| Sample | 22.4 | 21.9 | -2.2% |
| Hand | 32.9 | 31.6 | -4.1% |

According to Table 9, errors all less than 5%, which is acceptable. Therefore, the load cells and temperature sensor are all working properly.

5.1.2 Evaluation of Sliding Velocity Control

For wear tests using DFT, sliding velocity of rubber sample is a crucial parameter. To validate how well the sliding velocity is controlled, tests were conducted under specified sliding velocities. Motor shaft position data was recorded to calculate actual sliding velocity. Here are two examples.

- Case 1: for a $v_s = 0.01m/s$ test, motors' RPM were set as:

$$n_{dm} = 100, n_{sm} = 117$$

$$(w_{dm} = 10.472rad/s, w_{sm} = 12.252rad/s)$$

- Case 2: for a $v_s = 0.1m/s$ test, motors' RPM were set as:

$$n_{dm} = 100, n_{sm} = 292$$

$$(w_{dm} = 10.472rad/s, w_{sm} = 30.578rad/s)$$

The actual motor shaft positions were drawn:

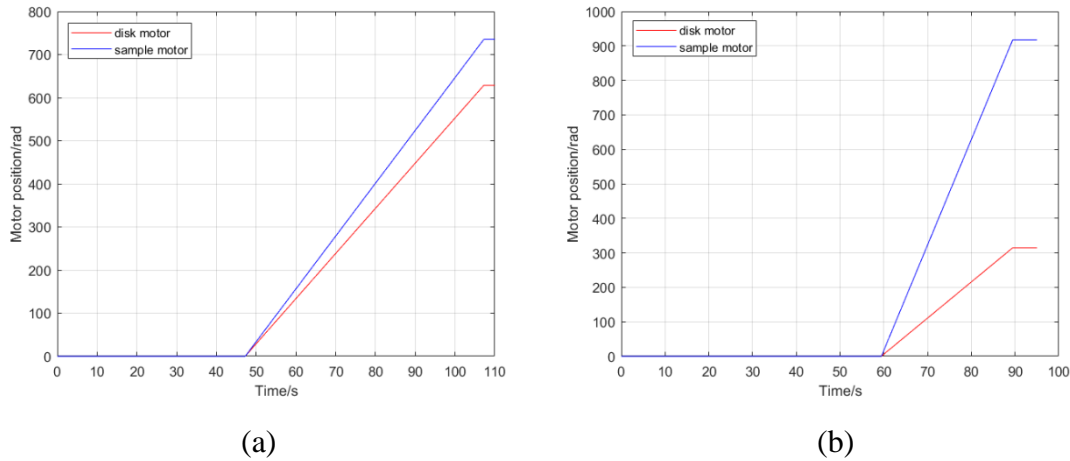


Figure 70. Motor shaft position curve. (a): case 1; (b): case 2

In Figure 70 (a), slope of the curves are: $k_{dm} = 10.460rad/s, k_{sm} = 12.252rad/s$.

In Figure 70 (b), slope of the curves are: $k_{dm} = 10.471rad/s, k_{sm} = 30.567rad/s$.

In both cases, the actual motor shaft speeds are close enough to desired values. Thus the slip velocity control is successful.

5.1.3 Fluctuation of Normal Load

For these tests, the normal load fluctuation must be kept as small as possible. To validate this, normal load data from various test configurations were extracted for analysis. Here are two examples.

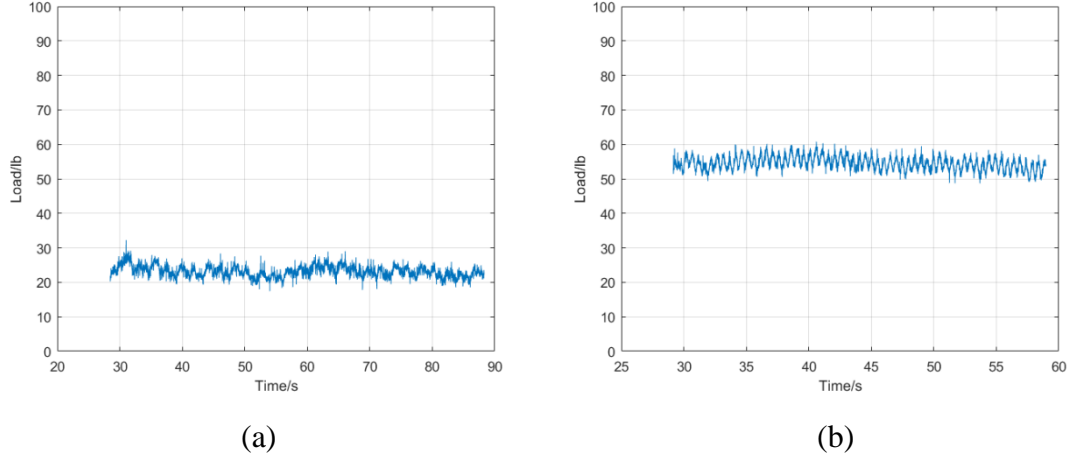


Figure 71. Normal load data during wear tests

In Figure 71(a), the mean normal load $\overline{F_n} = 23.11$ lb, standard deviation $\sigma = 1.46$.

In Figure 71(b), the mean normal load $\overline{F_n} = 54.48$ lb, standard deviation $\sigma = 1.84$.

From contact patch test in section 5.2.1, we can easily calculate that, in the range of 20 to 100 lb normal load, 5 lb load fluctuation will cause less than 5% contact patch pressure fluctuation, which is acceptable. Thus, we construct a criterion of a normal load distribution whose $\mu = \overline{F_n}$, and 95% of load data have less than 5 lb difference from $\overline{F_n}$. Therefore, a load data set should have a standard deviation $\sigma \leq 2.55$. Under this criterion, load fluctuation in both cases are acceptable.

5.1.4 Repeatability of Wear Test

To validate the repeatability of rubber sample wear tests on the DFT, wear tests under five different sliding velocities were each repeated 15 times. Standard deviations of rubber sample weight loss under these five conditions are listed in Table 10.

Table 10. Standard deviation of repeated wear tests

| $v_s(m/s)$ | σ |
|------------|----------|
| 0.010 | 0.0046 |

| | |
|-------|--------|
| 0.015 | 0.004 |
| 0.018 | 0.0046 |
| 0.020 | 0.0045 |
| 0.022 | 0.005 |

Sample weights were measured by the old weight scale, which has a precision of 0.01 g. To evaluate the repeatability of wear tests, we use a normal distribution that 95% instances has less than 0.01 g difference from μ . Therefore, the standard deviation of repeated wear tests should be no bigger than 0.0051. Compare the standard deviations in Table 10 with the criteria, we can conclude that the repeatability of rubber sample wear test on the DFT is acceptable.

After these evaluations, we can conclude that the DFT has met the design requirements, and wear data collected from it is trustable.

5.2 Initial Machine Learning Based Rubber Wear Modeling

Since the DFT has met the design requirements, the next step is conducting rubber sample wear tests under different configurations. Collected data needs conversion before being used to train wear models, thus two kinds of additional tests are necessary, they are:

- Contact patch area tests. We already know that contact patch pressure is an influential factor for rubber wear. However, we cannot directly measure contact patch pressure during tests. Since normal load is measured during tests, if we have a curve of contact patch area vs. load, contact patch pressure can be calculated. Having contact patch pressure also makes it easier to correlate rubber sample wear with tire wear.
- Effective radius tests. Sliding velocity is another influential factor of wear. To calculate it, rubber samples effective radius is needed. Therefore, we need a curve of effective radius vs. load for every rubber compound.

With these two curves, collected wear data can be converted and used to train wear models. At this stage, all machine learning algorithms listed in section 4.9 will be evaluated.

5.2.1 Contact Patch Area of Rubber Samples

There are two main purposes of acquiring rubber samples' contact patch area under different loads:

1. With contact patch area and normal load, average contact patch pressure can be easily calculated.
2. With contact patch area, weight loss per minute can be converted into weight loss per sliding distance.

To acquire a curve of contact patch area vs. normal load, rubber sample was mounted on the DFT, with a piece of Fujifilm prescale film between sample and road surface. Normal loads from 10 lb to 100 lb with 10 lb increments were applied on the rubber sample, and resulted in red patches on the film. Area of these red patches is a decent approximation of contact patch area.

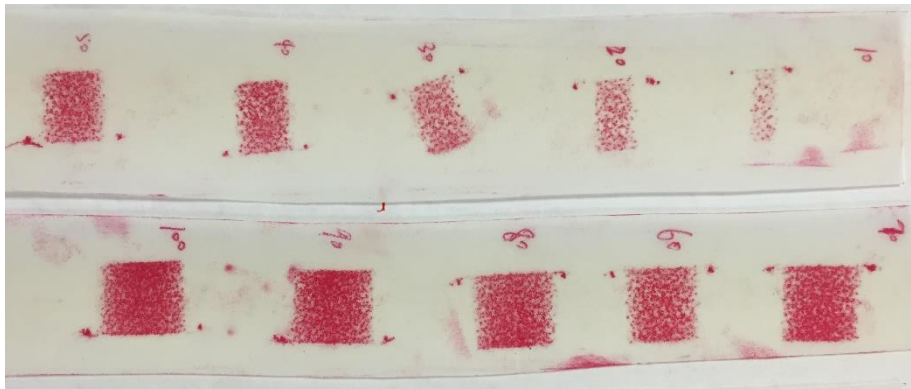


Figure 72. Red patches on prescale film representing the sample contact patch

Table 11. Contact patch test results (compound A)

| Load/lb | Area/mm ² |
|---------|----------------------|
| 0 | 0 |
| 10 | 97.35 |
| 20 | 190 |
| 30 | 260 |

| | |
|-----|-------|
| 40 | 280 |
| 50 | 320 |
| 60 | 369 |
| 70 | 389.5 |
| 80 | 430.5 |
| 90 | 436.8 |
| 100 | 478.4 |

The model of rubber compression is nonlinear and complicated, and researchers have developed different rubber spring models. For example, Berg proposed a rubber spring model, which is a sum of elastic force, friction force and viscous force (Berg, 1998). Since the load increment in our test data is as small as 10 lb, to simplify the problem, the data was fitted to a quadratic polynomial curve, which has a degree of 2 and 3 coefficients. The fitted curve is shown in Figure 73. Every rubber compound has to be tested to acquire its contact patch area vs. load curve.

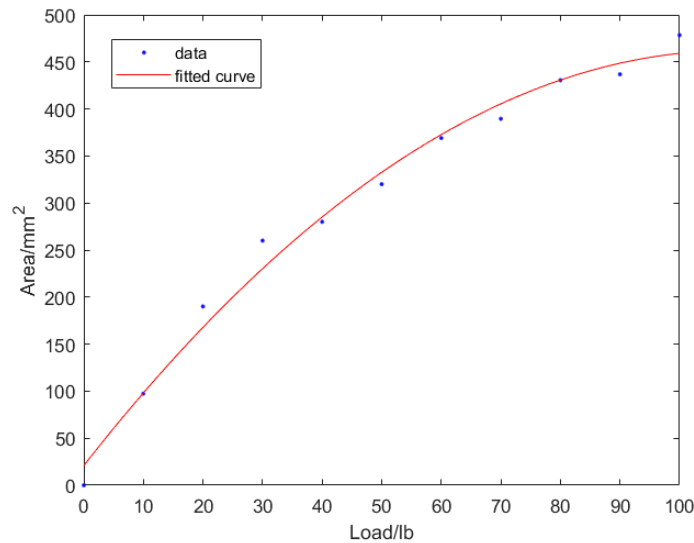


Figure 73. Contact patch area vs. load (rubber compound A)

With the fitted curve, we can further calculate and plot the relationship between load and contact patch pressure, as shown in Figure 74.

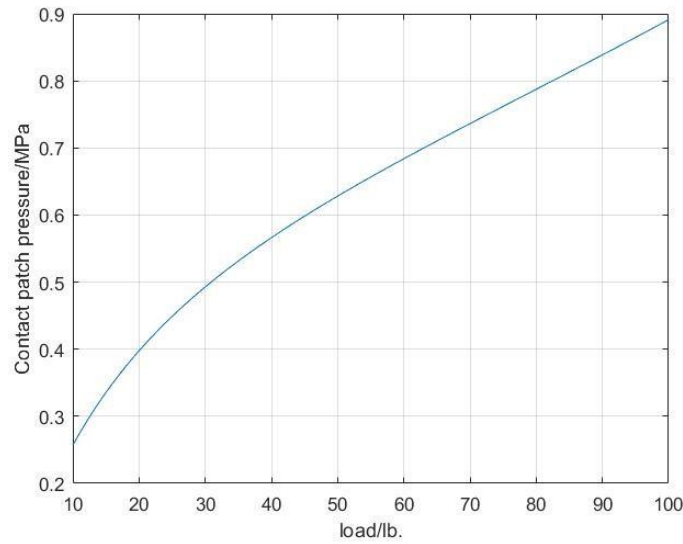


Figure 74. Contact patch pressure vs. load (compound A)

5.2.2 Effective Radius of Rubber Sample

Sliding velocity of rubber sample is:

$$v_s = v_f - wR_c \quad (5.1)$$

Where v_f is forward velocity, w is angular velocity of rubber sample, R_c is effective radius of rubber sample, and will change according to normal load on it. To calculate accurate sliding velocity under different test conditions, a curve of R_c vs. F_N must be acquired.

To acquire the curve, rubber sample was mounted on the DFT, and normal loads from 10 lb to 100 lb with 10 lb increments were applied on rubber sample. Distance from contact patch center to sample center was measured.

Table 12. Rubber sample deformation test results (compound A)

| Normal load/lb | compression/mm |
|----------------|----------------|
| 0 | 0 |
| 10 | 0.52 |
| 20 | 0.88 |
| 30 | 1.31 |
| 40 | 1.75 |
| 50 | 2.28 |
| 60 | 2.89 |
| 70 | 3.26 |

| | |
|-----|------|
| 80 | 3.92 |
| 90 | 4.45 |
| 100 | 4.46 |

For the same reason of the previous section, the data was fitted to a quadratic polynomial curve as shown in Figure 75. Every rubber compound has to be tested to acquire its curve of R_c vs. F_N .

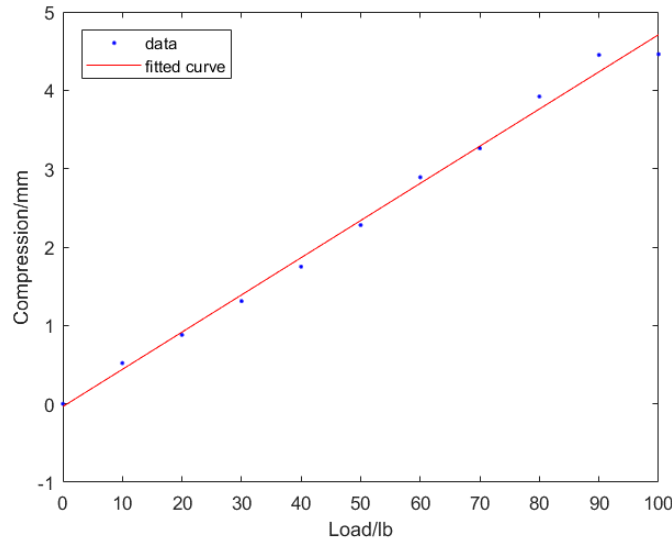


Figure 75. R_c vs. F_N (compound A)

5.2.3 Performance of Different Machine Learning Based Wear Models

To compare the performance of different machine learning algorithms and choose the better ones for the final rubber sample wear modeling, more diverse wear test data is necessary. Table 13 represents the expanded test configurations of rubber sample wear tests on the DFT. Compared with early wear test data configurations in Table 7, these changes were made:

- P240 sandpaper was introduced as alternative road surface. Sandpaper P120 is a commonly used sandpaper in industrial sample/tire friction tests, which is believed to have similar friction coefficient as asphalt. P240 sandpaper is less sharp than P120 sandpaper, thus rubber wear will be influenced less by shearing.

- Nominal contact patch pressure has been replaced by normal load. Since different compounds have different contact patch area under the same normal load, it is more straightforward and feasible to configure normal loads rather than contact patch pressures. Considering the differences of all eight compounds that we have, minimum and maximum normal loads were chosen to cover the usual range of contact patch pressures (0.2 - 0.4 MPa) in literatures.
- Range of sliding velocities was changed. Minimum sliding velocity was changed to zero, which is one of most common test conditions in literatures. The maximum sliding velocity is 0.1 m/s because higher sliding velocity will significantly increase sample temperature, and the current cooling system is not capable of keeping the temperature constant in those situations.

Table 13. Test configurations for model comparison

| Test configuration | Number of variations | Details |
|----------------------------|-----------------------------|--------------------------------|
| Rubber compound | 2 | A, B |
| Disk surface | 2 | Sandpaper P120, P240 |
| Normal load | 5 | 10, 20, 30, 40, 50 lb. |
| Sliding velocities | 5 | 0, 0.025, 0.05, 0.075, 0.1 m/s |
| Variations in total | 100 | |

With sliding velocity configurations, measured rubber sample diameter and Figure 75, RPM of servo motors can be calculated. Wear tests were carried out following the procedures in section 3.1.6.

After collecting rubber sample wear data of the listed 100 conditions, all seven machine learning algorithms in section 4.9 were used to train the wear model. Comparison of these models are shown in Table 14, performance of these machine learning algorithms are judged by their RMSE, R^2 , and time of computation.

Table 14. Performance comparison of machine learning algorithms

| Models | RMSE | R^2 | Time/s |
|---------------|------|-------|--------|
| Boosted trees | 0.08 | 0.83 | 1.1 |
| Bagged trees | 0.11 | 0.68 | 1.7 |
| Linear SVM | 0.08 | 0.84 | 1.7 |
| Quadratic SVM | 0.03 | 0.98 | 0.8 |
| Cubic SVM | 0.03 | 0.99 | 0.8 |
| Gaussian SVM | 0.06 | 0.90 | 0.7 |
| 2-layer ANN | 0.02 | 0.99 | 1 |

According to the values of R^2 , it is clear that boosted trees, bagged trees and linear SVM were out-performed. Focusing on the rest models, Gaussian SVM has worse RMSE and worse R^2 . The performance of quadratic SVM, cubic SVM and 2-layer ANN are very close in all three aspects: RMSE, R^2 , and time consumption.

Based on their better performance compared with other algorithms, quadratic SVM, cubic SVM and 2-layer ANN will be priorities in future wear modeling when more wear test data is available. Gaussian SVM will still be used as reference.

5.3 Improvement of Rubber Wear Model

Inputs of the initial rubber wear model, was decided by combing major influential factors of rubber abrasion, and the capability of DFT. While more test conditions are being tried, it becomes obvious that rubber oxidation is a wear-influential factor that cannot be neglected. After that, dimension reduction is conducted to further improve the performance of rubber sample wear model.

5.3.1 Introducing the Influence of Oxidation

The influence of oxidation on wear is a factor that researcher usually neglected. There are two main reasons:

- Rubber oxidation is a chemistry-based problem, and there is no model that can describe the relationship among compound, oxidation and rubber properties.

- Standard rubber oxidation tests are static, and have strict requirement of temperature, humidity, and oxygen concentration (Sun, Luo, Watkins, & Wong, 2004). Designing a repeatable rubber abrasion test with strict environmental requirement is extremely difficult.

While more test conditions are being attempted, it is more and more clear that oxidation is a wear-influential factor that cannot be ignored. For example, Figure 76 shows the wear rates of compound C running on P120 sandpaper. For instances 1 to 5, sliding velocity $V_s = 0$, normal load increase from 10 lb. to 50 lb. with even interval. For instances 6 to 10, $V_s = 0.025$ m/s, normal load increase from 10 lb. to 50 lb. This principle applies to the rest 15 instances: for each small group of 5 instances, normal load increase from 10 lb. to 50 lb., V_s is 0.025 m/s higher than the previous group. According to literature reviews (Gent & Walter, 2006), the trend of these instances should be: among each small group, wear rate increases; the next small group of 5 instances has a similar increasing pattern but starts at a higher initial wear rate. Instances 1 to 15 matches this prediction, but instances 16 to 25 show a quite different pattern:

- For instances 16 to 20: wear rate drops at 40 lb. normal load, initial wear rate is very close to the previous group.
- For instances 21 to 25: wear rate drops at 50 lb. normal load, initial wear rate is much lower than the previous group.

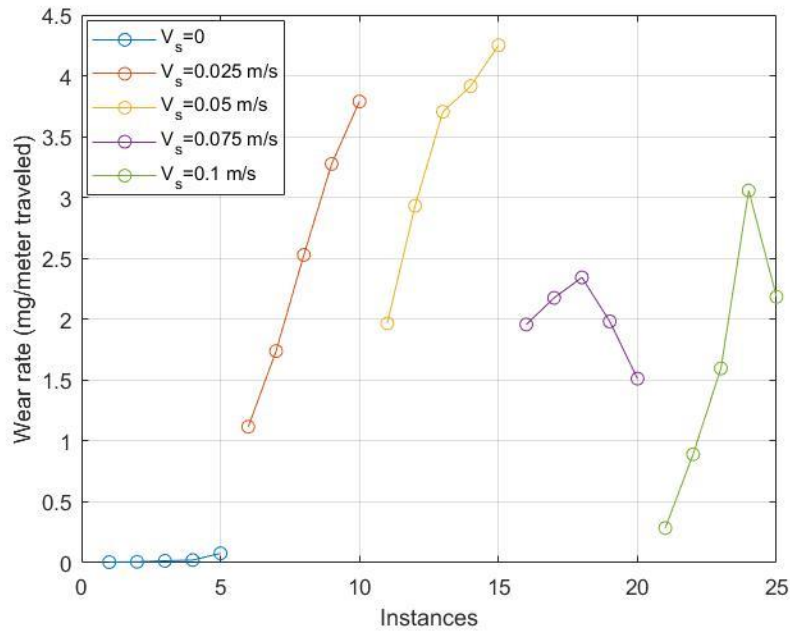


Figure 76. Wear rates of compound C on P120 sandpaper

Obviously, other factors are causing this "abnormal" pattern. After going through all related data, no inputs in the wear model can provide a satisfying explanation. For example, Figure 77 shows the pattern of contact patch temperature, whose pattern generally matches prediction, and cannot explain the wear rate pattern of instances 16 to 20.

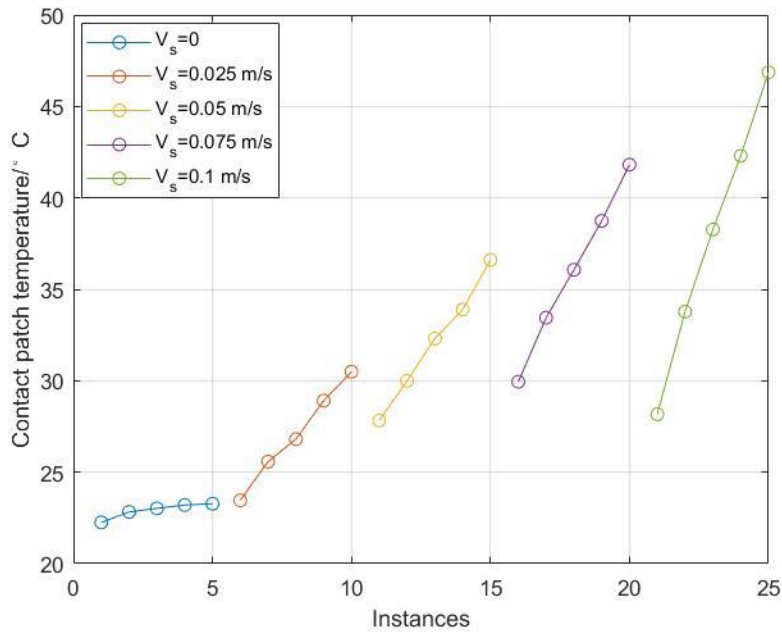


Figure 77. Contact patch temperature of compound C on P120 sandpaper

To understand the influence of oxidation under different wear test conditions, wear tests are conducted using 2 synthetic rubber + 2 natural rubber, under 5 different sliding velocities and 4 different normal loads. After examine the rubber surface and wear particles, a rough correlation of test conditions and oxidation can be concluded, which is shown in Table 15.

Table 15. Correlation of test conditions and oxidation

| | Dynamic | Crack size | Rubber surface | Sticky? | Rubber particles | Obvious oxidation? | Wear rate |
|------------------|----------------|-------------------|-----------------------|----------------|---------------------------|---------------------------|------------------|
| Synthetic rubber | Light | No cracks | Smooth | No | Very fine powder | No | low |
| | Moderate | Small | Rough Dim | No | Short strings | No | Medium |
| | Severe | No cracks | Rough shinny | Yes | Sticky round particles | Yes | low |
| NR | Light | Small | Smooth Dim | No | Fine powder | No | Very low |
| | Moderate | Medium | Rough Dim | No | Short strings | No | medium |
| | Severe | No cracks | Rough shinny | Yes | Sticky round particles | Yes | low |

Features of the correlations are summarized as below:

- Sticky surface is an indication of severe oxidation, oil and carbon black in rubber compounds will come out of the sample. The result is a black track on sandpaper, and oily rubber surface that is shinny.
- With increase severity of dynamic conditions (sliding velocity, normal load), all compounds will eventually have severe oxidation.
- Under light dynamic conditions, some synthetic rubber compounds will become even smoother, similar to polishing metal with sandpaper.

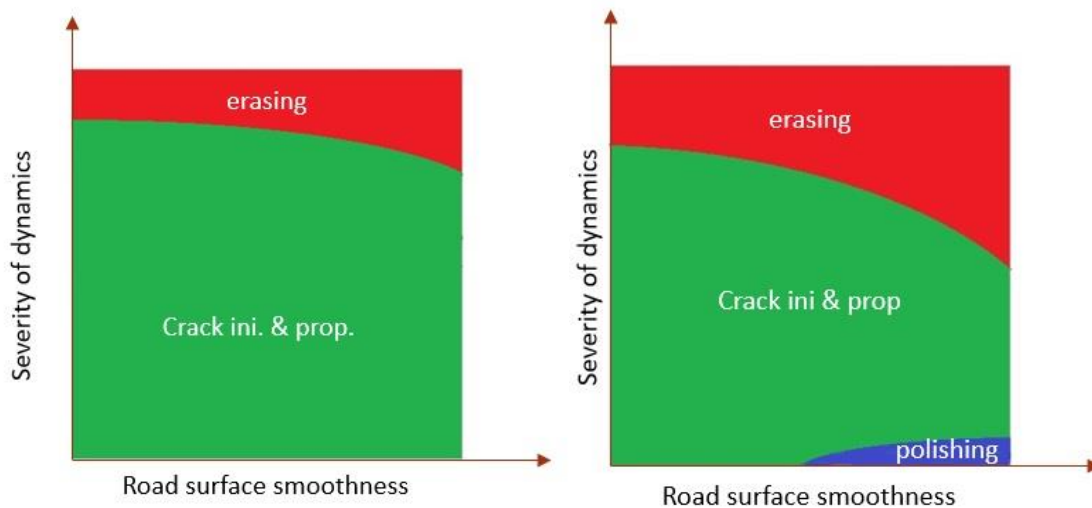
- Different compounds have drastically different resistance against oxidation.
- Finer sandpaper will cause earlier oxidation.

To incorporate these correlations into machine learning based wear model, features have to be extracted to represent the influence of oxidation. Therefore, a new classification of rubber abrasion behaviors is proposed.

Table 16. Classification of rubber abrasion behaviors

| Behavior | Condition | Rubber surface | Wear rate |
|-----------------------------------|---|--------------------------------|---------------|
| Polishing | Smooth road surface, Very light dynamics | Very smooth | Extremely low |
| Crack initiation & propagation | All surface, Moderate dynamics | Cracks dim | Almost linear |
| Erasing | All surface, Severe dynamics | Rough, sticky, oily, shinny | Low |

For easier understanding of the correlations and classification above, and shows the relationship of road surface smoothness, severity of dynamics, and resulting abrasion behavior. Both figures have no actual values on x-y axis or explicit functions of the splitting curves, extensive wear tests are necessary to generate these figures with actual values for different compounds.



(a)

(b)

Figure 78. Relationship of road smoothness, severity of dynamics, and abrasion behavior.
 (a) NR. (b) Synthetic rubber

It is true that using oxidation rate as an input in wear model can better describe this major influential factor. However, oxidation rate testing involves large consumption of toluene, a kind of toxic chemical. Meanwhile, since oxidation rate takes an extra 24 hours to measure, and there is no models that can predict oxidation rate from compounds and test conditions, it is not applicable to directly use oxidation rate as input of rubber abrasion model, not to mention tire wear model. Therefore, a simplified method is proposed: use the labels of these 3 behaviors as input of wear model. To guarantee that this simplified method still can represent the difference of oxidation rate, toluene tests are designed and carried out.

The basis of the validation of the proposed method, is that rubber particles have higher degrees of dissolving in toluene due greater oxidation. Tests were conducted on P240 sandpaper, which can generate diverse wear behaviors on different rubber compounds. Rubber wear particles from 15 different test conditions were collected, laid closely on millimeter paper for total size estimation. Particles were stored in labeled test tubes, and 10 mL toluene was added into each test tube. After 24 hours, toluene was dumped, and the remaining wear particles were air dried and measured again. Test results are listed in Table 17.

Table 17. Toluene test conditions

| Compound | $V_s(m/s)$ | $F_N/lb.$ | Particle shape | Sticky? | Particle numbers BEFORE | Particle numbers AFTER | Remaining size |
|----------|------------|-----------|----------------|---------|-------------------------|------------------------|----------------|
| C | 0.01 | 20 | Round | No | 15 | 15 | 95% |
| C | 0.025 | 20 | thin string | No | 12 | 12 | 95% |
| C | 0.05 | 30 | thin string | partial | 6 | 9 | 90% |
| C | 0.075 | 40 | thicker string | Yes | 6 | 8 | 80% |
| C | 0.1 | 50 | Thicker string | Yes | 8 | 8 | 70% |

| | | | | | | | |
|---|-------|----|-------------|-----|----|----|------|
| F | 0.01 | 20 | Round | Yes | 6 | 7 | 80% |
| F | 0.025 | 20 | Round | Yes | 5 | 6 | 60% |
| F | 0.05 | 30 | Round | Yes | 5 | 6 | 60% |
| F | 0.075 | 40 | Round | Yes | 5 | 5 | 75% |
| F | 0.1 | 50 | Round | Yes | 5 | 5 | 80% |
| H | 0.01 | 20 | Thin string | No | 22 | 22 | 100% |
| H | 0.025 | 20 | Thin string | No | 13 | 13 | 95% |
| H | 0.05 | 30 | Thin string | No | 6 | 15 | 90% |
| H | 0.075 | 40 | Thin string | no | 6 | 20 | 95% |
| H | 0.1 | 50 | round | yes | 7 | 16 | 80% |

Due to dissolving, rubber particles could break into smaller pieces, which resulted in increasing number of particles in some cases. Based on the table, it can be concluded that rubber particles generated from different wear behavior has distinct degree of dissolving in toluene: for particles from crack initiation & propagation behavior (non-sticky), there are 90% to 100% remaining; for particles from erasing behavior (sticky), there are only 60% to 80% remaining. Therefore, using the labels of different wear behaviors can roughly represent the change of oxidation rate, and act as inputs of machine learning based rubber wear model.

5.3.2 Feature Selection

An attempt of feature selection was made mainly for two reasons:

- Better understanding of major wear-influential factors and their correlation.
- Since collecting data from tire wear test is more difficult and usually has less available features, reducing the input dimension of rubber sample wear model can reduce the difficulty of correlating rubber sample wear and tire wear.

At this stage, among the inputs of rubber sample wear model, most of them are either major test parameters (load, rubber compound properties), independent parameters (road surface roughness) or inputs that have unpredictable correlation with other inputs (oxidation). After reviewing all current inputs, there are two inputs can possibly be removed: longitudinal friction force and contact patch temperature.

Since high accuracy is priority and there are only two removable features, wrapper method is used in this feature selection. Cubic SVM model is used to train wear model of each subset: remove longitudinal friction force, remove contact patch temperature, and remove both. Performance of these models are compared with reference model that is trained by original data set. The results are in Table 18.

Table 18. Comparison of reference and select-feature wear models

| | RMSE | R^2 |
|--------------------------------|-------------|-------------------------|
| reference | 15.95 | 0.99 |
| Remove F_f | 16.01 | 0.99 |
| Remove T_c | 15.42 | 0.99 |
| Remove both | 20.59 | 0.98 |

Since these R^2 values are very close, the focus is on RMSE values. Obviously, when contact patch temperature is removed, the corresponding wear model has the smallest RMSE value. This makes sense because contact patch temperature is a highly predictable feature depends on the remaining features.

Therefore, contact patch temperature will be removed from the final rubber wear model. This also makes tire wear correlation easier since it is difficult to collect accurate contact patch temperature from a fast-rotating tire.

5.4 Complete Rubber Wear Model

After introducing oxidation into rubber wear model, and performed feature selection, the last step before training the final model, is further increasing the diversity of wear data. Comparing with the other configurations, there were only 2 road surface: P120 and P240 sandpaper. The main difficulties in finding suitable road surface material are repeatability and durability:

- Repeatability. Road surfaces on the DFT are changed frequently. Material like concrete, it's hard to keep repeatability even for professionals in a time span of years.

- Durability. Some wear tests on the DFT are not only severe to rubber samples, but also road surfaces. Material like tar papers, although their hardness and profile are so close to actual asphalt road, they "wear" even faster than rubber sample. This is huge extra cost of time and money, and also have repeatability issues.

P60 sandpaper was chosen as the third road surface. It is even rougher than P120 sandpaper, thus capable of providing wear data with less potential of oxidation. Wear test configurations for final rubber sample wear models are listed in Table 19.

Table 19. Final wear test configurations

| Test configuration | Number of variations | Details |
|----------------------------|-----------------------------|--------------------------------|
| Rubber compound | 8 | A, B, C, D, E, F, G, H |
| Disk surface | 3 | Sandpaper P60, P120, P240 |
| Normal load | 5 | 10, 20, 30, 40, 50 lb. |
| Sliding velocities | 5 | 0, 0.025, 0.05, 0.075, 0.1 m/s |
| Variations in total | 600 | |

Structure of the final rubber wear model is shown in Figure 79. Machine learning algorithms are: 2-layer feedforward neural network, quadratic SVM, cubic SVM, and Gaussian SVM.

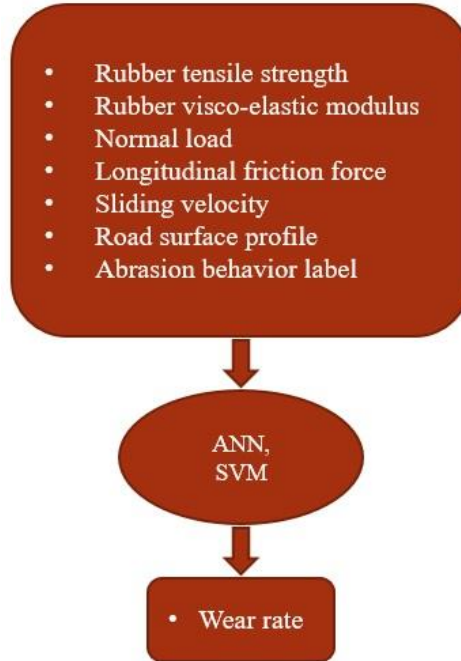


Figure 79. Structure of final rubber wear model

Based on performance of these four models in *Table 20*, 2-layer feedforward neural network based model is the best-performing rubber wear model, and becomes the final rubber wear model.

Table 20. Comparison of last-four wear models

| | RMSE | R^2 | Time cost/s |
|----------------------|-------------|-------------------------|--------------------|
| ANN | 15.87 | 0.97 | 1.0 |
| Quadratic SVM | 27.73 | 0.84 | 0.73 |
| Cubic SVM | 19.33 | 0.92 | 1.6 |
| Gaussian SVM | 29.14 | 0.83 | 0.80 |

Since the wear model is a high-dimensional model, it is impossible to completely represent the relationship of each input and output in a few figures. Figure 80 to Figure 83 represent the relationship of some inputs and output, with comparison of test results and prediction results of ANN and cubic SVM models. Figure 80 represents the relationship of normal load, sliding velocity, and wear rate of rubber compound E tested on P120 sandpaper. Based on the shape and color of these 3 figures, it is obvious that

ANN model has better fitting of test data. Figure 81 to Figure 83 illustrate the relationship of individual inputs and wear rate, and the comparison between prediction and test results. It has to be mentioned that, in the 5th subplot of Figure 81, rubber sample was under the influence of severe oxidation. The wear model successfully predicts the pattern of wear rate, but the wear rate values are not accurate. This indicates that adding wear behavior labels make it possible to predict rubber wear under severe oxidation, but values of oxidation rate are still necessary to accurately predict wear rates under these situations.

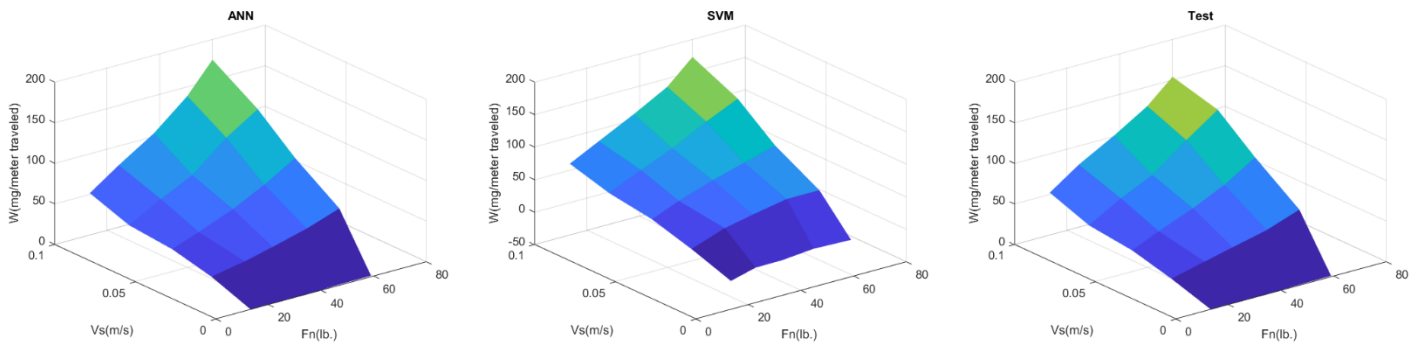


Figure 80. wear rate vs. normal load – sliding velocity. Compound E on P120 sandpaper

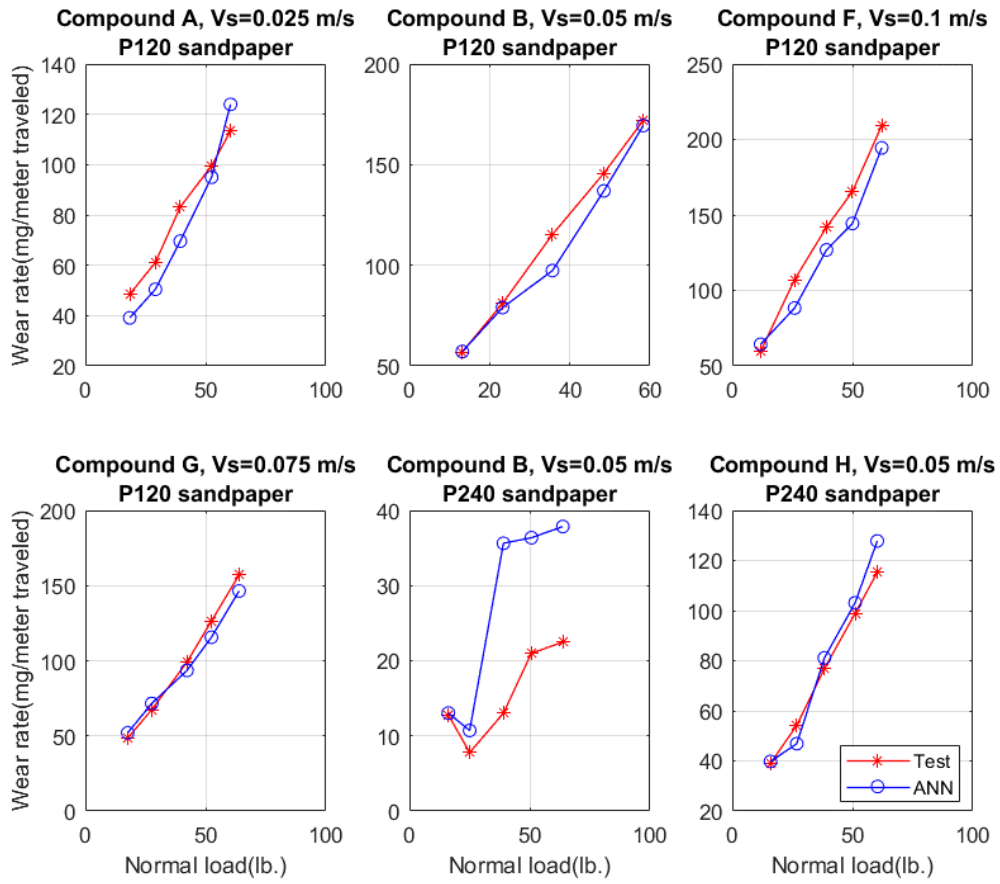


Figure 81. Test and predictions of wear rate vs. normal load

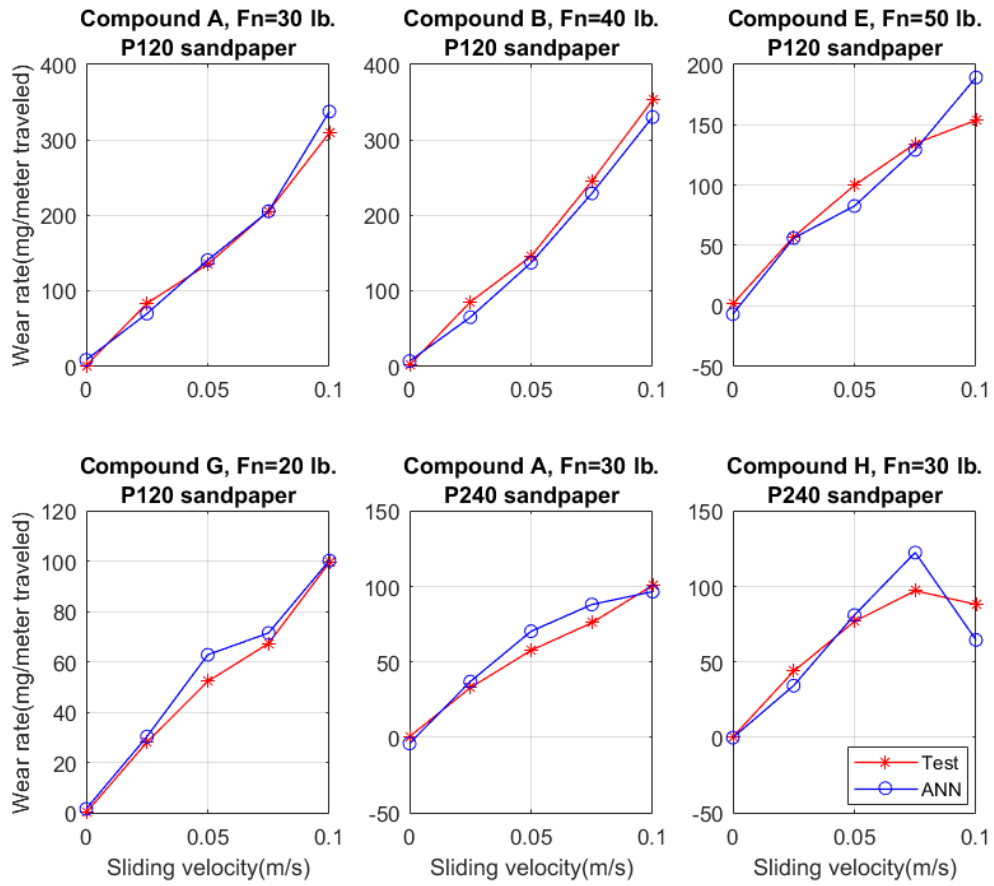


Figure 82. Test and predictions of wear rate vs. sliding velocity

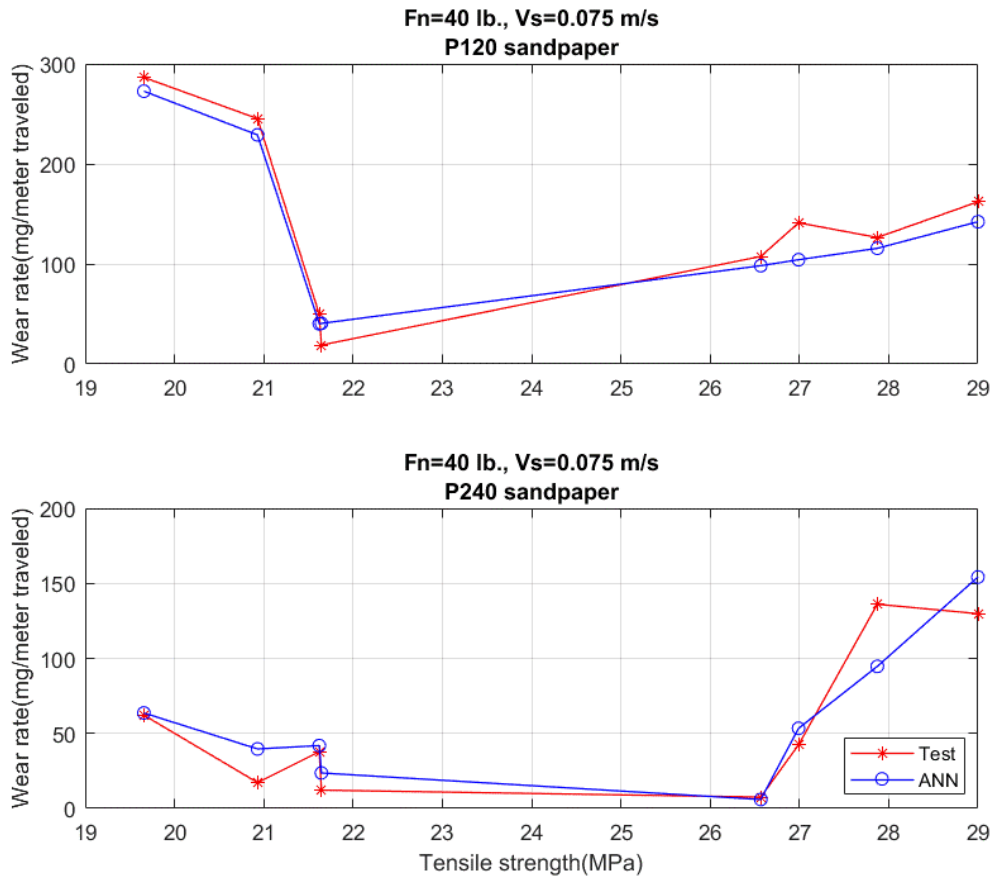


Figure 83. Test and predictions of wear rate vs. tensile strength

In the next section, the final ANN-based rubber wear model was used for correlating rubber wear and tire wear.

5.5 Correlation of Rubber Wear and Tire Wear

After developing machine learning based rubber wear model, the final step is developing a set of conversion functions, so that tire wear test conditions can be transformed and used as the inputs of rubber wear model. The predicted tire wear rate is compared with actual wear rate from test data.

5.5.1 Converting Parameters of Tire Wear into Rubber Wear

Based on literature reviews and results in previous sections, inputs of rubber wear model and major measurable tire wear influential factors are summarized in Table 21.

Tire wear test on the modified rolling resistance machine and standard road test are separated.

Table 21. Rubber wear model and tire wear influential factors

| Inputs | Rubber wear model | RR machine | Road |
|-----------------------|--------------------------|-------------------|-------------|
| Rubber properties | ✓ | ✓ | ✓ |
| Normal load | ✓ | ✓ | ✓ |
| Longitudinal friction | ✓ | ✓ | |
| Sliding velocity | ✓ | | |
| Road profile | ✓ | ✓ | ✓ |
| Abrasion behavior | ✓ | ✓ | ✓ |
| Slip angle | | ✓ | ✓ |
| Route map | | | ✓ |

- Rubber properties. Properties (hardness, visco-elastic modulus, tensile strength) of tire tread compound are measurable.
- Normal load. On the RR machine, normal load is measured by a load cell. For road tests, normal load is estimated by measuring the static load on each tire.
- Longitudinal friction. Estimated on the RR machine, not measurable during a standard road test.
- Sliding velocity. On the RR machine, calculated from slip angle and forward velocity. For road tests, can be estimated from forward velocity and route map.
- Road profile. On the RR machine, the road surface material is P120 sandpaper. For road tests, road surface profile can be measured by a profilometer.
- Abrasion behavior. For both RR machine and road tests, wear particles can be collected and categorized into the 3 abrasion behaviors.

- Slip angle. On the RR machine, slip angle is a controlled test parameter. For road tests, slip angle exists when a vehicle is make a turn.
- Route map. Route map is only for road tests, and it provides the information of road type, travel distance, vehicle velocity, traffic lights, turnings, etc.

Based on these comparisons, it is clear that tire wear test data collected from RR machine and road tests requires different conversion functions.

5.5.1.1 Conversion functions for RR machine

To correlate rubber wear model and tire wear from RR machine tests, correlation functions are needed for normal load, sliding velocity, and slip angle.

To convert the large normal load \bar{F}_{Nt} on tire into the normal load input \bar{F}_{Nr} of rubber wear model, tire contact patch test is necessary to acquire the contact patch area A_t under the same normal load and pneumatic pressure of tire wear testing. Average tire contact patch pressure can be calculated by:

$$\bar{P} = \frac{\bar{F}_{Nt}}{A_t} \quad (5.2)$$

Using contact patch area tests described in section 5.2.1, we can calculate the corresponding normal load on rubber sample when its contact patch pressure is \bar{P} .

Sliding velocity and slip angle have to be considered together. To accelerate tire wear tests, a slip angle is applied to test tire on the RR machine. This slip angle has two main influence on tire: sliding velocity and lateral force. Lateral force is not considered in this wear model. Sliding velocity can be calculated by:

$$v_s = v_f \tan \alpha \quad (5.3)$$

Where v_f is the forward velocity of tire, which is the same as the drum speed of the RR machine. α is the slip angle.

5.5.1.2 Conversion functions for road testing

To correlate rubber wear model and tire wear from road tests, correlation functions are needed for normal load, sliding velocity, slip angle, and route map. The

method of normal load conversion is the same as that of tire wear tests on the RR machine.

During the majority of the travel distance in a standard road test, the tire can be considered as free rolling and has no slip angle. Therefore, wear rate of tire tread can be directly calculated by rubber wear model.

Test vehicles have to stop at red traffic lights. Based on UTQG standard, vehicles have to brake and stop smoothly, which indicates that tires will not reach their peak friction coefficient (threshold of activating ABS). On dry asphalt, depends on rubber compound, friction coefficient reaches maximum value when slip ratio is 15 to 20%. Therefore, a safe approximation of average slip ratio during braking is 10%.

When traffic lights turn green, test vehicles have to accelerate smoothly until reach the speed limit of the road. Following the similar idea of braking, a safe approximation of average slip ratio during acceleration is 10%.

When a test vehicle is turning, it generally takes about 1 second to enter steady state handling. Therefore, tire wear during transient handling is negligible, and tire wear during cornering is considered as steady state. Under this assumption, when a test vehicle is turning, its forward velocity is considered constant. Based on UTQG standard, ballasts are left in vehicles so that weight distribution on front and rear axles are the same. Meanwhile, all four tires on a test vehicle are the same, and they have the same cornering stiffness. Therefore, understeering coefficient

$$K_{us} = \frac{W_f}{C_{\alpha f}} - \frac{W_r}{C_{\alpha r}} = 0 \quad (5.4)$$

It has to be mentioned that actual K_{us} is also influenced by suspension compliance, steering compliance, camber thrust, etc. Considering all the factors and determining the precise values of K_{us} requires repeated constant radius, constant speed, or constant steer tests on the route map. To reduce the complexity of calculating K_{us} , these factors were not considered in this research. Substitute (5.4) into high speed steady state turning equation for two DOF bicycle model:

$$\delta = \frac{L}{R} + K_{us} a_y = \frac{L}{R} \quad (5.5)$$

Where δ is steering angle, L is the length of wheelbase, R is turning radius. Meanwhile, since $K_{us} = 0$, front and rear slip angle are equal:

$$\alpha_f = \alpha_r \quad (5.6)$$

Therefore, slip angle α measured by a two-antenna GPS and optical sensor can be considered as the slip angle for both front tires and rear tires. However, these equipment are too expensive for ordinary tire wear test. Multiple slip angle estimation methods were proposed by researchers (Fukada, 1999) (Piyabongkarn, Rajamani, Grogg, & Lew, 2009), but they also need additional sensors such as accelerometers. For standard UTQG results, where information of vehicle dynamics is highly limited, slip angle can be roughly estimated by:

$$\alpha = \frac{Mv_f^2}{4RC_\alpha} \quad (5.7)$$

Where M is mass of vehicle, C_α is cornering stiffness of test tire.

Sliding velocity of test tire is:

$$v_s = v_f(1 - \cos \alpha) \quad (5.8)$$

5.5.1.3 Conversion function for wear rate

The unit of rubber wear rate, is weight loss per travelled distance, while the unit of tire wear rate, is tread depth deduction per travelled distance. Therefore, a conversion function is necessary to correlate these two wear rates.

Define rubber sample wear rate as:

$$w_r = \frac{\Delta m_r}{L_r} \quad (5.9)$$

Where Δm_r is weight loss after travel a distance of L_r .

Firstly, tread depth deduction has to be converted into weight loss:

$$\Delta m_t = \rho \eta_p C_i b_p \Delta h \quad (5.10)$$

Where ρ is density of tread compound, η_p is contact patch ratio when average contact patch pressure is P , b_p is the width of contact patch when average contact patch

pressure is P , C_t is the outer circumference of tire, Δh is tread depth deduction. It has to be mentioned that pneumatic pressure influences the values of η_p, b_p, C_t .

Assume that wear on rubber sample and tire are uniform. Therefore, weight loss of rubber sample and tire can be correlated by:

$$\Delta m_r = \frac{C_r b_r}{C_t b_p} \Delta m_t \quad (5.11)$$

Where C_r is the circumference of rubber sample, b_r is the thickness of rubber sample.

For a specific surface area on rubber sample and tire tread, it is not always in contact with the ground. For RR machine test, the sliding velocity is lateral, while in road tests, the major sliding velocity is longitudinal. The correlation of travel distances is:

For RR machine test,

$$\begin{aligned} \frac{l_{rP}}{C_r} L_r &= \frac{b_p}{C_t} L_t \\ L_r &= \frac{b_p C_r}{l_{rP} C_t} L_t \end{aligned} \quad (5.12)$$

For road test,

$$\begin{aligned} \frac{l_{rP}}{C_r} L_r &= \frac{l_{tP}}{C_t} L_t, \\ L_r &= \frac{l_{tP} C_r}{l_{rP} C_t} L_t \end{aligned}$$

Where l_{rP}, l_{tP} are the length of rubber sample/tire contact patch when average contact patch pressure is P . Substitute these correlations into (5.9), we get the conversion function for wear rate:

$$\begin{aligned} w_r &= \frac{b_r l_{rP} \rho \eta_p C_t}{b_p} \frac{\Delta h}{L_t} \\ &= \frac{b_r l_{rP} \rho \eta_p C_t}{b_p} w_t \text{ (RR machine test)} \\ w_r &= \frac{b_r l_{rP} \rho \eta_p C_t}{l_{tP}} \frac{\Delta h}{L_t} \\ &= \frac{b_r l_{rP} \rho \eta_p C_t}{l_{tP}} w_t \text{ (road test)} \end{aligned} \quad (5.13)$$

5.5.2 Tire Wear Tests

Tire wear tests were conducted using the modified RR machine. Tire wear data of road testing was also acquired.

5.5.2.1 Wear tests on the RR machine

A passenger car tire was used for wear tests on the RR machine, and test parameters are listed in Table 22.

Table 22. Parameters of wear tests on RR machine

| | |
|----------------------------|----------------|
| Tire size | 205/55ZR16.94 |
| Tread compound | A |
| Pneumatic pressure | 0.24 MPa |
| Normal load | 4500 N |
| Drum surface | P120 sandpaper |
| Slip angle | 11 degrees |
| travelling velocity | 20 km/h |
| Test duration | 10 mins |

Tread depths were measured after 10 minutes of test, and the test was conducted for once due to safety reasons. During tread depth measurement, UTQG standard was strictly followed as in Figure 84. Measurements of test tire tread depth reduction is shown in Table 23.



Figure 84. Standard tread measurement

Table 23. Tread depth measurements of RR machine tests (in mm)

| | | Out | #1 | #2 | In |
|-----------|---------|------------|-----------|-----------|-----------|
| T=0 | T1 | 7.65 | 8 | 8.06 | 7.63 |
| | T2 | 7.65 | 8.13 | 8.05 | 7.56 |
| | T3 | 7.71 | 8.18 | 7.98 | 7.57 |
| | T4 | 7.53 | 8 | 8.01 | 7.57 |
| | T5 | 7.64 | 8 | 8.01 | 7.63 |
| | T6 | 7.53 | 8.07 | 8.01 | 7.61 |
| | Average | 7.62 | 8.06 | 8.02 | 7.59 |
| T=10 mins | T1 | 7.6 | 8.03 | 8.01 | 7.56 |
| | T2 | 7.58 | 8.03 | 8.03 | 7.54 |
| | T3 | 7.55 | 8.03 | 7.98 | 7.55 |
| | T4 | 7.52 | 7.99 | 7.96 | 7.54 |
| | T5 | 7.62 | 7.98 | 7.97 | 7.6 |
| | T6 | 7.46 | 8.02 | 7.98 | 7.59 |

| | | | | | |
|--|---------|------|------|------|------|
| | Average | 7.55 | 8.01 | 7.98 | 7.56 |
|--|---------|------|------|------|------|

The average tread depth reduction is 0.05 mm.

5.5.2.2 Wear test on roads

Tire wear data from road tests was provided by a tire company. Test tires are mounted on all-wheel drive Volkswagen Touareg. Test parameters are listed in Table 24, and route map information are listed in Table 25.

Table 24. Parameters of tire wear tests on road

| | |
|--|------------|
| Tire size | 255/50ZR19 |
| Tread compound max tensile strength | 22.3 MPa |
| Pneumatic pressure | 0.22 MPa |
| Normal load | 6566 N |
| Road surface | Asphalt |
| Weather | Sunny |
| Average road temperature | 15°C |

Table 25. Route map information

| Section | Length (km) | Velocity (km/h) | Traffic lights | Left turn | Right turn |
|----------------|------------------------|----------------------------|---------------------------|------------------|-------------------|
| 1 | 16.2 | 65 | 1 | 3 | 5 |
| 2 | 25.2 | 95 | 0 | 3 | 3 |
| 3 | 74.4 | 52 | 34 | 14 | 16 |
| 4 | 99.1 | 93 | 0 | 7 | 11 |
| 5 | 118.6 | 55 | 16 | 27 | 34 |
| 6 | 156.4 | 103 | 0 | 3 | 2 |
| 7 | 15.9 | 40 | 5 | 2 | 3 |
| Total | 505.8 | | 56 | 59 | 74 |

Tread depths were measured after travelling 2532 km, and the test was repeated for 16 times. UTQG standard was strictly followed, such as tire rotation, tread depth measurement, etc. Tread depth reductions of test tire A1 is shown in Table 26.

Table 26. Tread depth of tire A2

| Loop | Average tread depth/mm | Deduction/mm |
|-------------|-------------------------------|---------------------|
| 1 | 7.36 | |
| 2 | 7.32 | 0.04 |
| 3 | 7.21 | 0.11 |
| 4 | 7.14 | 0.07 |
| 5 | 7.09 | 0.05 |
| 6 | 7.05 | 0.04 |
| 7 | 6.95 | 0.10 |
| 8 | 6.91 | 0.04 |
| 9 | 6.73 | 0.18 |
| 10 | 6.61 | 0.02 |
| 11 | 6.41 | 0.20 |
| 12 | 6.17 | 0.24 |
| 13 | 5.89 | 0.28 |
| 14 | 5.77 | 0.12 |
| 15 | 5.45 | 0.32 |
| 16 | 4.88 | 0.57 |

Due to the influence of random incidents during tests, such as encountering less red traffic lights, sudden breaks, etc., tire wear data of road tests has a relatively high variance. The least tread depth reduction (0.02 mm) and the most reduction (0.57 mm) is excluded from the calculation of average tread depth reduction. The trimmed mean tread depth reduction for every 505.8 km is 0.0275 mm.

5.5.3 Validation of the Conversion Functions

Validation of the conversion functions consists of three major steps: predict rubber wear rate, convert rubber wear rate into tire wear rate, and compare the predicted tire wear rate with test data. For wear data collected from the RR machine and road tests, the validating procedures are slightly different, which will be explained in detail.

5.5.3.1 Validating by RR machine wear test data

To validate the conversion functions for wear data collected from the RR machine, the steps are:

- Convert tire test parameters into valid inputs of machine learning based rubber wear model.
- Predict rubber wear rate by: $w_r = W(X_r)$. $W(x)$ is machine learning based rubber wear model, X_r is a matrix of inputs.
- Compare the predicted rubber wear rate with test data.
- Convert rubber wear rate into tire wear rate.
- Compare the predicted tire wear rate with test data.

Table 27. Constants and coefficients of tire wear test on RR machine

| | |
|---|----------------------|
| P/MPa | 0.39 |
| ρ/(kg/m³) | 1.52*10 ³ |
| $\eta_{0.39}$ | 0.71 |
| C_t/m | 1.96 |
| $b_{0.39}$/m | 0.1612 |
| C_r/m | 0.251 |
| b_r/m | 0.018 |
| $l_{r0.39}$/m | 0.0176 |
| $l_{t0.39}$/m | 0.0996 |

In the calculation of weight loss, the sliding velocity is 1.08 m/s, which is out of the range of rubber wear model. Based on additional wear tests with constant contact patch pressure of 0.39 MPa, compound A enters erasing behavior when sliding velocity is

higher than 0.15 m/s on P120 sandpaper. In erasing behavior, wear rate is relatively constant against increasing sliding velocity. Therefore, rubber sample wear rate when $V_s = 1.08$ m/s was calculated by using 0.2 m/s sliding velocity.

The predicted rubber sample weight loss is:

$$\begin{aligned}\Delta m_r &= W(X_r)V_s t = 0.0642 * 5.56 * 600g \\ &= 214.17g\end{aligned}$$

Substitute this weight deduction into (5.13), the predicted tread depth reduction $\Delta h = 0.0515$ mm, compared with measured average tread depth reduction 0.05mm, the predicted value is 3.0% larger. The major reason for this are:

- Rubber wear model. The actual sliding velocity is 1.08 m/s, which is out of the prediction range of rubber wear model. Therefore, the wear rate is approximated, not calculated.
- Uneven wear. In the actual tire wear tests, pressure, oxidation rate and wear rate on different part of the tread is different.

5.5.3.2 Validating by road wear test data

Using road wear test data for validation, is more complicated because of test parameter variation. Validation steps are as follows:

- Divide route map into three categories: free rolling, braking/accelerating (traffic light), and turning. Convert test parameters into valid inputs of machine learning based rubber wear model.
- Assume that stopping in front of traffic lights and make turning are separate incidents. Predict rubber weight loss after one loop by:

$$\Delta m_r = \sum_{i=1}^7 W_1(X_{fr_i})L_i + \sum_{j=1}^{112} \Delta m_{tl_j} + \sum_{k=1}^{133} W_1(X_{m_k})L_k \quad (5.14)$$

Where $W_1(x)$ is machine learning based rubber wear model without the input of longitudinal friction. X_{fr} is input matrix of free rolling conditions, Δm_{tl} is weight loss from accelerating and braking in front of traffic lights, and X_m is input matrix of turning conditions. Δm_{tl} is calculated by:

$$\Delta m_{it} = \sum_{t=0}^{T_{ba}} W_1 (X_t) v_t dt \quad (5.15)$$

Where T_{ba} is the time cost of ordinary complete stop or accelerate till require velocity. Average acceleration during braking and accelerating is considered as $\mp 0.5m / s^2$.

- Convert rubber weight loss into tire tread depth deduction.
- Compare the predicted tire wear and test data.

After converting load on tire into contact patch pressure, known constants and coefficients are listed in Table 28.

Table 28. Constants and coefficients of tire wear test on road

| | |
|---|----------------------|
| P/MPa | 0.23 |
| ρ/(kg/m³) | 1.52*10 ³ |
| $\eta_{0.23}$ | 0.76 |
| C_t/m | 2.322 |
| $b_{0.23}$/m | 0.207 |
| C_r/m | 0.251 |
| b_r/m | 0.018 |
| $l_{r0.23}$/m | 0.015 |
| $l_{t0.23}$/m | 0.144 |

Since not every road, traffic light and corners of the route map can be found on Google map, and important information such as road turning radius and angles of the corners and ramps are not available. Therefore, the route map has to be simplified for rubber weight loss calculation:

- Section 1, 3, 5, and 7 are roads inside cities, most of which are four lane roads, and most corners in section 1, 3, 5, and 7 are 90 degrees. To simplify wear calculation, every corner in these 4 sections are considered as 90 degrees. Based on GB standard of road turning radius, single lane width is 3.5 to 4 m, and the central turning radius of a four lane road (14 to

16 m wide) is 15 m. Therefore, right turn radius is considered as 11 m, and left turn radius is considered as 19 m.

- Section 2, 4 and 6 are highways. Corners on these three sections, are large curves that gradually change directions, and gentle interchanges. To simplify wear calculation, every corner in these 4 sections are considered as 60 degrees, turning radius are considered as 500 m.

Therefore, Table 25 can be divided into smaller segments to calculate rubber weight loss in each segment. In the calculation of weight loss, there are sliding velocities that are larger than 0.1 m/s, which are out of the range of rubber wear model. Since maximum tensile strength and viscoelastic modulus of the tread compound is very close to compound C, it will enter erasing behavior when sliding velocity is higher than 0.075 m/s on P120 sandpaper. In erasing behavior, wear rate is relatively constant against increasing sliding velocity. Therefore, when sliding velocities are larger than 0.1 m/s, wear rates were calculated by using 0.1 m/s sliding velocity.

Table 29. Predicted weight loss in each road segment

| Section | movement | Velocity(m/s) | Distance (m) | Sliding velocity (m/s) | Weight loss (g) | number |
|---------|--------------|---------------|--------------|------------------------|-----------------|--------|
| 1 | Free rolling | 18.05 | 15787 | 0 | 1.989 | 1 |
| 1 | Brk/acc | 18.05 | 326 | | 2.328 | 1 |
| 1 | Left turn | 18.05 | 29.8 | 0.36 | 0.213 | 3 |
| 1 | Right turn | 18.05 | 17.3 | 1.07 | 0.123 | 5 |
| 2 | Free rolling | 26.39 | 22058.4 | 0 | 2.779 | 1 |
| 2 | turn | 26.39 | 523.6 | 0.0035 | 0.066 | 6 |
| 3 | Free rolling | 14.44 | 66617 | 0 | 8.394 | 1 |
| 3 | Brk/acc | 14.44 | 208.5 | | 1.488 | 34 |
| 3 | Left turn | 14.44 | 29.8 | 0.12 | 0.213 | 14 |
| 3 | Right turn | 14.44 | 17.3 | 0.35 | 0.123 | 16 |
| 4 | Free rolling | 25.83 | 89675.2 | 0 | 11.299 | 1 |
| 4 | turn | 25.83 | 523.6 | 0.0031 | 0.066 | 18 |
| 5 | Free rolling | 15.28 | 113471.2 | 0 | 14.297 | 1 |
| 5 | Brk/acc | 15.28 | 233.5 | | 1.667 | 16 |

| | | | | | | |
|---|--------------|-------|---------|--------|--------|----|
| 5 | Left turn | 15.28 | 29.8 | 0.16 | 0.213 | 27 |
| 5 | Right turn | 15.28 | 17.3 | 0.47 | 0.123 | 34 |
| 6 | Free rolling | 28.61 | 153782 | 0 | 19.116 | 1 |
| 6 | turn | 28.61 | 523.6 | 0.0052 | 0.1110 | 5 |
| 7 | Free rolling | 11.11 | 15171.5 | 0 | 1.912 | 1 |
| 7 | Brk/acc | 11.11 | 123.4 | | 0.881 | 5 |
| 7 | Left turn | 11.11 | 29.8 | 0.03 | 0.958 | 2 |
| 7 | Right turn | 11.11 | 17.3 | 0.09 | 0.242 | 3 |

The total rubber weight deduction $\Delta m_r = 164.701\text{g}$. Substitute this weight deduction into (5.13), the predicted tread depth reduction $\Delta h = 0.0327\text{mm}$, compared with measured average tread depth reduction 0.0275mm , the predicted value is 18.9% larger than measurement. The major reasons for this are:

- Road surface. Although P120 sandpaper is widely used in tire related tests as a substitute of asphalt, it is sharper than asphalt, and cause higher wear rate.
- Estimated slip angle. Due to the lack of slip angle and related vehicle dynamics measurement in standard UTQG tests, it is not possible to acquire or calculate accurate slip angles for corners on the route map.
- Rubber wear model. Besides normal wear prediction errors, when sliding velocity is larger than 0.1 m/s, since it is out of the range of rubber wear model, the wear rate is approximated, not calculated.
- Uneven wear. In actual tire wear tests, pressure, oxidation rate and wear rate on different part of the tread is different.
- Simplified rout map. Instead of calculating the total wear caused by the 196 different scenarios on the route map, they are simplified into 22 scenarios.

6. Conclusions

This research was initiated with the goal of developing new wear test machines and methods, and machine learning based rubber/tire wear models. Literature on crack initiation, crack propagation, empirical wear models, major contributing factors on rubber and tire wear, rubber materials, and rubber oxidation were studied. In combination of studying most of the existing sample/tire friction/wear test machines and methods, it was found that it is necessary to design new test machines that can control or measure the majority of exterior factor that influence wear rate of rubber samples or tires. For rubber samples, the factors are: normal load, friction, speed, sliding velocity, temperature at contact patch and road surface roughness. For tires, the factors are: load, friction, speed, sliding velocity, slip angle, temperature, tire construction and road surface. Meanwhile, literature reviews on machine learning methods and their applications revealed the possibility of applying machine learning methods on rubber sample/tire wear modeling. Therefore, supervised machine learning models were studied and practiced.

With the knowledge of factors of abrasion/wear and existing testing machines, the Dynamic Friction Tester (DFT) was designed and built. Countless validations and modifications have been performed on the DFT until it met all requirements for rubber wear testing. Early trustable wear test data was used to validate the idea of applying machine learning methods on rubber/tire wear modeling. The results of this initiative, strengthened the confidence of using machine learning methods to develop practical wear models.

After wear data of two rubber compounds on two kinds of sandpapers were collected, the data was used to train rubber sample wear models via seven different machine learning algorithms. Performance of the trained models proved that the approach of using machine learning methods in rubber wear modeling is correct. Also, comparisons of the trained models showed that quadratic SVM, cubic SVM and 2-layer feedforward neural network have better performance than other algorithms, and should be tried first in final wear modeling.

As rubber wear data was collected from more and more test conditions, it became clear that our initial wear model inputs, which were decided by literature reviews and test capabilities, cannot explain wear rate changes in severe test conditions. After examination of rubber surface and wear particles, it turned out that rubber oxidation is the critical factor that was neglected. However, there is no easy method to measure rubber oxidation rate after each test, and there is no model that can predict oxidation rate from compounds and test conditions. Therefore, a simplified method was proposed: use the label of three distinct wear behaviors as the oxidation input of rubber wear model. To reduce the dimension of wear model inputs, feature selection was conducted, and contact patch temperature was removed from model inputs. The final rubber wear model was trained by wear data collected from 600 different test conditions. The model has eight inputs, including rubber properties, oxidation, dynamics, and road surface profile, with wear rate as the output. 2-layer feedforward neural network proved to be the best-performing algorithm in rubber wear modeling.

To correlate rubber wear and tire wear, conversion functions were proposed to correlate the inputs and the output of rubber wear model and tire wear model. These conversion functions were validated by tire wear data collected from the RR machine and road tests.

To summarize the contributions of the research, the following can be stated:

- Comprehensive understanding of crack initiation, crack propagation, empirical wear models, major contributing factors on rubber & tire wear, rubber materials, and rubber oxidation.
- Designed, built, and validated the DFT as a reliable platform for rubber sample wear testing.
- With other lab members, modified a rolling resistance machine that can be used in tire wear testing.
- Rubber sample wear tests were performed under combination of different test configurations: 8 different rubber compounds, sandpapers of 3 different grit sizes, 5 nominal normal loads, and 5 sliding velocities. In total 600 test conditions.

- Introduced rubber oxidation, a crucial but less studied wear influential factor, into rubber wear model.
- Four different machine learning methods were developed to train the final rubber wear model. After comparing the performance of trained models, it was concluded that 2-layer feedforward neural network has the best performance in rubber wear modeling.
- Conversion functions that can correlate rubber sample wear and tire wear were proposed, and validated by indoor and on-road tire wear test data.

Finally, a tire wear model was developed by incorporating machine design, machine learning based rubber wear model, and rubber-tire wear conversion functions. Instead of spending enormous time and resources in tire wear tests, tire industries now have a significantly faster and economical approach to predict tire wear.

7. Future Work

The work presented here can be further developed as follows:

- In rubber wear tests, sandpapers are used as road surfaces partially because of their high repeatability and durability. However, sandpaper is still different from asphalt roads, which influences the tire wear model. Finding repeatable and durable asphalt-like materials that can be used on the DFT road disk, will improve the performance of tire wear model.
- Oxidation rate is a crucial wear influential factor that cannot be fully utilized now. The two potential solutions are: developing a fast and accurate method to measure oxidation rate without damaging rubber surface, or developing a model that is able to predict rubber oxidation rate from compound and test conditions. The latter solution requires extensive polymer background knowledge.
- To improve the performance of rubber wear model, the range of current test parameters can be expanded, and new test parameters can be introduced. For example, number of compounds can be increased, the upper limit of sliding velocity can be increased, oxygen density can be introduced, and environmental humidity can be introduced (an environmental chamber has been ordered for DFT for this purpose).
- To accurately predict UTQG standard tire wear, detail information (surface roughness, speed limit, turning radius, etc.) of every road and corner is necessary. This requires extensive collaboration with a tire company.

References

- Abu-Abdeen, M. (2001). Degradation of the mechanical properties of composite vulcanizates loaded with paraffin wax. *Journal of applied polymer science*, 81(9), 2265-2270.
- Anderson, T. L. (2017). *Fracture mechanics: fundamentals and applications*. CRC press.
- Artificial neural network*. (2017). Retrieved from Wikipedia:
https://en.wikipedia.org/wiki/Artificial_neural_network#cite_note-Zell1994ch5.2-49
- Baldwin, J., & Bauer, D. (2008). Rubber oxidation and tire aging-a review. *Rubber Chemistry and Technology*, 81(2), 338-358.
- Baldwin, J., Bauer, D., & Ellwood, K. (2004). Effects of Nitrogen Inflation on Tire Aging and Performance. *Rubber & Plastics News*, (pp. 34(4), 14-19).
- Baldwin, J., Bauer, D., & Ellwood, K. (2005). Accelerated aging of tires, Part III. *Rubber chemistry and technology*, 78(5), 767-776.
- Baldwin, J., Bauer, D., & Hurley, P. (2005). *Field Aging of Tires, Part III*. San Antonio, TX: Rubber Division, ACS.
- Barber, M., Donley, J., & Langer, J. (1989). Steady-state propagation of a crack in a viscoelastic strip. *Physical Review A*, 40(1), 366.
- Barenblatt, G. I. (1962). The mathematical theory of equilibrium cracks in brittle fracture. *Advances in applied mechanics*, 7, 55-129.
- Bauer, D., Baldwin, J., & Ellwood, K. (2007). Rubber aging in tires. Part 2: Accelerated oven aging tests. *Polymer Degradation and Stability*, 92(1), 110-117.
- Bayer, R. G. (1991). Comments on engineering needs and wear models. *Tribological Modeling for Mechanical Designers*.
- Bayer, R. G. (1994). *Mechanical wear prediction and prevention*. Marcel Dekker.
- Beebe, D. (2004, 8). Procedures for Tire Treadwear Testing.
- Berg, M. (1998). A non-linear rubber spring model for rail vehicle dynamics analysis. *Vehicle system dynamics*, 30(3-4), 197-212.
- Berres, R., & Barz, D. (2017). *High Speed Linear Friction Tester (HSLFT)*. Retrieved from Altracon:
http://www.altracon.com/Downloads/HSLFT/HSLFT%2003_17.pdf

- Berritta, R., Cossalter, V., Doria, A., & Ruffo, N. (2002). Identification of Motorcycle Tire Properties by Means of A Testing Machine. *Proc. 2002 SEM Annual Conference and Exposition on Experimental and Applied Mechanics*.
- Bootstrap aggregating*. (2017). Retrieved from Wikipedia: https://en.wikipedia.org/wiki/Bootstrap_aggregating
- Breiman, L. (1996). Bagging predictors. *Machine Learning* 24(2), 123-140.
- Breiman, L. (2001). Random forests. *Machine learning* 45(1), 5-32.
- Breiman, L., Friedman, J., Stone, C., & Olshen, R. (1984). *Classification and regression trees*. CRC press.
- Busfield, J., Liang, H., Fukahori, Y., & Thomas, A. (2005). Modelling the abrasion process in elastomer materials. *CONSTITUTIVE MODELS FOR RUBBER-PROCEEDINGS-*, (pp. Vol. 4, p. 139).
- Busfield, J., Tsunoda, K., Davies, C., & Thomas, A. (2002). Contributions of time dependent and cyclic crack growth to the crack growth behavior of non strain-crystallizing elastomers. *Rubber chemistry and technology*, 643-656.
- Champ, D., Southern, E., & Thomas, A. (1974). Fracture mechanics applied to rubber abrasion. *Advances in Polymer Friction and Wear*, 133-144.
- Cho, J., & Jung, B. (2007). Cho, J. C., and B. C. Jung. "Prediction of Tread Pattern Wear by an Explicit Finite Element Model 3. *Tire science and Technology*, 35(4), 276-299.
- Choi, S. (1997). Migration of antidegradants to the surface in NR and SBR vulcanizates. *Journal of applied polymer science*, 65(1), 117-125.
- Comon, P. (1994). Independent component analysis, a new concept? *Signal processing*, 36(3), 287-314.
- Cortes, C., & Vapnik, V. (1995). Support-vector networks. *Machine learning* 20.3, 273-297.
- Coveney, V., & Menger, C. (1999). Initiation and development of wear of an elastomeric surface by a blade abrader. *Wear*, 702-711.
- Cunneen, J. (1968). Oxidative aging of natural rubber. *Rubber chemistry and technology*, 41(1), 182-208.
- Davidshofer, K., & Murphy, C. (2005). *Psychological testing: principles and applications*. Pearson/Prentice.
- De, S., & White, J. (2001). *Rubber technologist's handbook. Vol. 1*. iSmithers Rapra Publishing.

- Description – Laboratory Abrasion & Skid Tester. (2014).
- Donnet, J. (1993). *Carbon black: science and technology*. CRC Press.
- Ellwood, K., Baldwin, J., & Bauer, D. (2006). Numerical simulation of thermal oxidation in automotive tires. *Rubber chemistry and technology*, 79(2), 249-266.
- Feedforward neural network*. (2017). Retrieved from Wikipedia:
https://en.wikipedia.org/wiki/Feedforward_neural_network
- Fernando. (2009). ASFT Surface Friction Tester, and Weather Systems Presentation.
- Ferreira, T., & Rasband, W. (2012). *ImageJ User Guide*. Retrieved from ImageJ:
<https://imagej.nih.gov/ij/docs/guide/user-guide.pdf>
- Fisher, R. A. (1937). *The design of experiments*. London: Oliver And Boyd.
- Flat-Trac Tire Test Systems*. (2014). Retrieved from MTS:
https://www.mts.com/cs/groups/public/documents/library/dev_002227.pdf
- Freund, Y., & Schapire, R. (1995). A decision-theoretic generalization of on-line learning and an application to boosting. *European conference on computational learning theory* (pp. 23-37). Springer.
- Frictional property tester of JLU. (2012).
- Fukada, Y. (1999). Slip-angle estimation for vehicle stability control. *Vehicle System Dynamics*, 32(4-5), 375-388.
- Fukahori, Y., & Yamazaki, H. (1994). Mechanism of rubber abrasion. Part I: Abrasion pattern formation in natural rubber vulcanizate. *Wear*, 195-202.
- Fukahori, Y., & Yamazaki, H. (1994). Mechanism of rubber abrasion: Part 2. General rule in abrasion pattern formation in rubber-like materials. *Wear*, 109-116.
- Fukahori, Y., & Yamazaki, H. (1995). Mechanism of rubber abrasion part 3: how is friction linked to fracture in rubber abrasion? *Wear*, 188(1-2), 19-26.
- Fukahori, Y., Liang, H., & Busfield, J. (2008). Criteria for crack initiation during rubber abrasion. *Wear*, 387-395.
- Gent, A. N. (1996). Adhesion and strength of viscoelastic solids. Is there a relationship between adhesion and bulk properties? *Langmuir*, 12(19), 4492-4496.
- Gent, A., & Pulford, C. (1983). Mechanisms of rubber abrasion. *Journal of Applied Polymer Science*, 943-960.
- Gent, A., & Walter, J. (2006). *Pneumatic Tire*. Retrieved from
http://ideaexchange.uakron.edu/mechanical_ideas/854

- Gent, A., Lindley, P., & Thomas, A. (1964). Cut growth and fatigue of rubbers. I. The relationship between cut growth and fatigue. *Journal of Applied Polymer Science*, 8(1), 455-466.
- George. (2017). *TE 75 Rubber Friction Test Machine*. Retrieved from PLINT Tribology Products: <http://www.phoenix-tribology.com/at2/leaflet/te75>
- Greenland, S., Robins, J., & Pearl, J. (1999). Confounding and collapsibility in causal inference. *Statistical science*, 29-46.
- Grosch, K., & Schallamach, A. (1961). Tyre wear at controlled slip. *Wear*, 4(5), 356-371.
- Grosch, K., & Schallamach, A. (1970). The Load Dependence of Laboratory Abrasion and Tire Wear. *Rubber Chemistry and Technology*, 43(4), 701-713.
- Gutierrez-Osuna, R. (2011). Principal components analysis. TX.
- Guyon, I., & Elisseeff, A. (2003). An introduction to variable and feature selection. *Journal of machine learning research*, 3(Mar), 1157-1182.
- Hastie, T., Tibshirani, R., & Friedman, J. (2001). *The Elements of Statistical Learning*. New York: Springer.
- Haykin, S. (1998). *Neural Networks: A Comprehensive Foundation (2nd Edition)*. Prentice Hall.
- Hofmann, M. (2006). Support vector machines-kernels and the kernel trick.
- Jaksch, T., Ortner, R., & Auer, P. (2010). Near-optimal regret bounds for reinforcement learning. *Journal of Machine Learning Research* 11, 1563-1600.
- James, G., Witten, D., Hastie, T., & Tibshirani, R. (2013). *An Introduction to Statistical Learning*. New York: springer.
- Joachims, T. (1998). Text categorization with support vector machines: Learning with many relevant features. *Machine learning: ECML-98*, 137-142.
- Jolliffe, I. (2011). Principal component analysis. *International encyclopedia of statistical science*, 1094-1096.
- Jü. (2011). *Sulfur vulcanization*. Retrieved from Wikipedia: https://en.wikipedia.org/wiki/Sulfur_vulcanization
- Kelley, C. T. (1999). *Iterative methods for optimization*. Society for Industrial and Applied Mathematics.
- Kistler. (2010). *RoadDyn S630 sp System 2000*. Retrieved from Kistler: <https://www.kistler.com/?type=669&fid=67304>
- Kohavi, R., & Provost, F. (1998). Glossary of terms. *Machine Learning*.

- Kriesel, D. (2012). *A Brief Introduction to Neural Networks*. Retrieved from dkriesel.com: http://www.dkriesel.com/en/science/neural_networks
- Lake, G., & Lindley, P. (1965). Role of ozone in dynamic cut growth of rubber. *Journal of Applied Polymer Science*, 9(6), 2031-2045.
- Langer, W., & Potts, G. (1980). *Development of a flat surface tire testing machine*. SAE Technical Paper.
- lcf300. (2016). Retrieved from FUTEK: <http://www.futek.com/files/pdf/Product%20Drawings/lcf300.pdf>
- Lewis, P. (1972). Protecting natural rubber against ozone cracking. *Natural Rubber Technology*, 3, 1-35.
- Liang, H., Fukahori, Y., Thomas, A., & Busfield, J. (2010). The steady state abrasion of rubber: Why are the weakest rubber compounds so good in abrasion? *Wear*, 268(5), 756-762.
- Lim, B. (2016). *HRB-103_203_303_602_1002*. Retrieved from LW Measurements, LLC: http://lwmeasurements.com/wp-content/uploads/2015/09/HRB-103_203_303_602_1002.pdf
- Lowne, R. W. (1970). The effect of road surface texture on tyre wear. *Wear*, 15(1), 57-70.
- Luchini, J. R. (1982). *Test surface curvature reduction factor for truck tire rolling resistance*. SAE Technical Paper.
- Lupker, H., Cheli, F., Braghin, F., Gelosa, E., & Kechman, A. (2004). Numerical prediction of car tire wear. *Tire Science and Technology*, 32(3), 164-186.
- LW12.8. (2017). Retrieved from Michigan Scientific Corporation: <http://www.michsci.com/download/lw12-8-datasheet/?wpdmdl=5389&ind=TFcxMi44LnBkZg>
- Mark, J., Erman, B., & Roland, M. (2013). *The science and technology of rubber*. Academic press.
- Michelin. (n.d.). *An unknown object: the tire - materials*. Retrieved from Michelin The tire digest: <https://thetiredigest.michelin.com/an-unknown-object-the-tire-materials#nav>
- Mohri, M., Rostamizadeh, A., & Talwalkar, A. (2012). *Foundations of Machine Learning*. The MIT Press.
- Nasir, M., & Teh, G. (1988). The effects of various types of crosslinks on the physical properties of natural rubber. *European polymer journal*, 24(8), 733-736.

- Persson , B., & Brener, E. (2005). Crack propagation in viscoelastic solids. *Physical Review*, 71(3), 036123.
- Piyabongkarn, D., Rajamani, R., Grogg, J., & Lew, J. (2009). Development and experimental evaluation of a slip angle estimator for vehicle stability control. *IEEE Transactions on control systems technology*, 17(1), 78-88.
- Ramdasi, S. S. (2016). *Enhancement of a Rolling Resistance Rig for Force and Moment Testing of Tires*.
- Replication (statistics)*. (2017, 6 27). Retrieved from Wikipedia:
[https://en.wikipedia.org/wiki/Replication_\(statistics\)](https://en.wikipedia.org/wiki/Replication_(statistics))
- Rhee, S. K. (1970). Wear equation for polymers sliding against metal surfaces. *Wear*, 16(6), 431-445.
- Ritchie, M., Hahn, L., Roodi, N., Bailey, L., Dupont, W., Parl, F., & Moore, J. (2001). Multifactor-dimensionality reduction reveals high-order interactions among estrogen-metabolism genes in sporadic breast cancer. *The American Journal of Human Genetics*, 69(1), 138-147.
- Rivlin, R., & Thomas, A. (1953). Rupture of rubber. I. Characteristic energy for tearing. *Journal of Polymer Science Part A: Polymer Chemistry*, 10(3), 291-318.
- Schallamach, A. (1952). Abrasion of rubber by a needle. *Journal of Polymer Science Part A: Polymer Chemistry* 9.5, 385-404.
- Shelton, J. (1972). Review of basic oxidation processes in elastomers. *Rubber Chemistry and Technology*, 45(2), 359-380.
- Shi, D., & Gindy, N. (2007). Tool wear predictive model based on least squares support vector machines. *Mechanical Systems and Signal Processing* 21, no. 4, 1799-1814.
- Slavkovic, R., Jugovic, Z., Dragicevic, S., Jovicic, A., & Slavkovic, V. (2013). An application of learning machine methods in prediction of wear rate of wear resistant casting parts. *Computers & Industrial Engineering* 64, no. 3, 850-857.
- Smith, K., Kennedy, R., & Knisley, S. (2008). Prediction of Tire Profile Wear by Steady-State FEM 5. *Tire Science and Technology*, 36(4), 290-303.
- Southern, E., & Thomas, A. (1979). Studies of rubber abrasion. *Rubber chemistry and technology*, 1008-1018.
- Statistics and Probability Dictionary*. (2017). Retrieved from Stat Trek:
http://stattrek.com/statistics/dictionary.aspx?definition=coefficient_of_determination

- Sun, Y., Luo, S., Watkins, K., & Wong, C. (2004). Electrical approach to monitor the thermal oxidation aging of carbon black filled ethylene propylene rubber. *Polymer Degradation and Stability*, 86(2), 209-215.
- Suykens, J., & Vandewalle, J. (1999). Least squares support vector machine classifiers. *Neural processing letters* 9.3, 293-300.
- Thomas, A. G. (1974). Factors influencing the strength of rubbers. *Journal of Polymer Science: Polymer Symposia*, Vol. 48, No. 1, pp. 145-157.
- Tire Rolling Resistance Measurement System*. (2014). Retrieved from MTS:
https://www.mts.com/cs/groups/public/documents/library/dev_002230.pdf
- Tire Tread Wear Simulation System*. (2014). Retrieved from MTS:
https://www.mts.com/cs/groups/public/documents/library/dev_002232.pdf
- Vert, J.-P., Tsuda, K., & Schölkopf, B. (2004). A primer on kernel methods. *Kernel Methods in Computational Biology*, 35-70.
- Weertman, J. (1973). Theory of fatigue crack growth based on a BCS crack theory with work hardening. *International Journal of Fracture*, 9(2), 125-131.
- Weston, J. (2006). Support Vector Machine Tutorial.